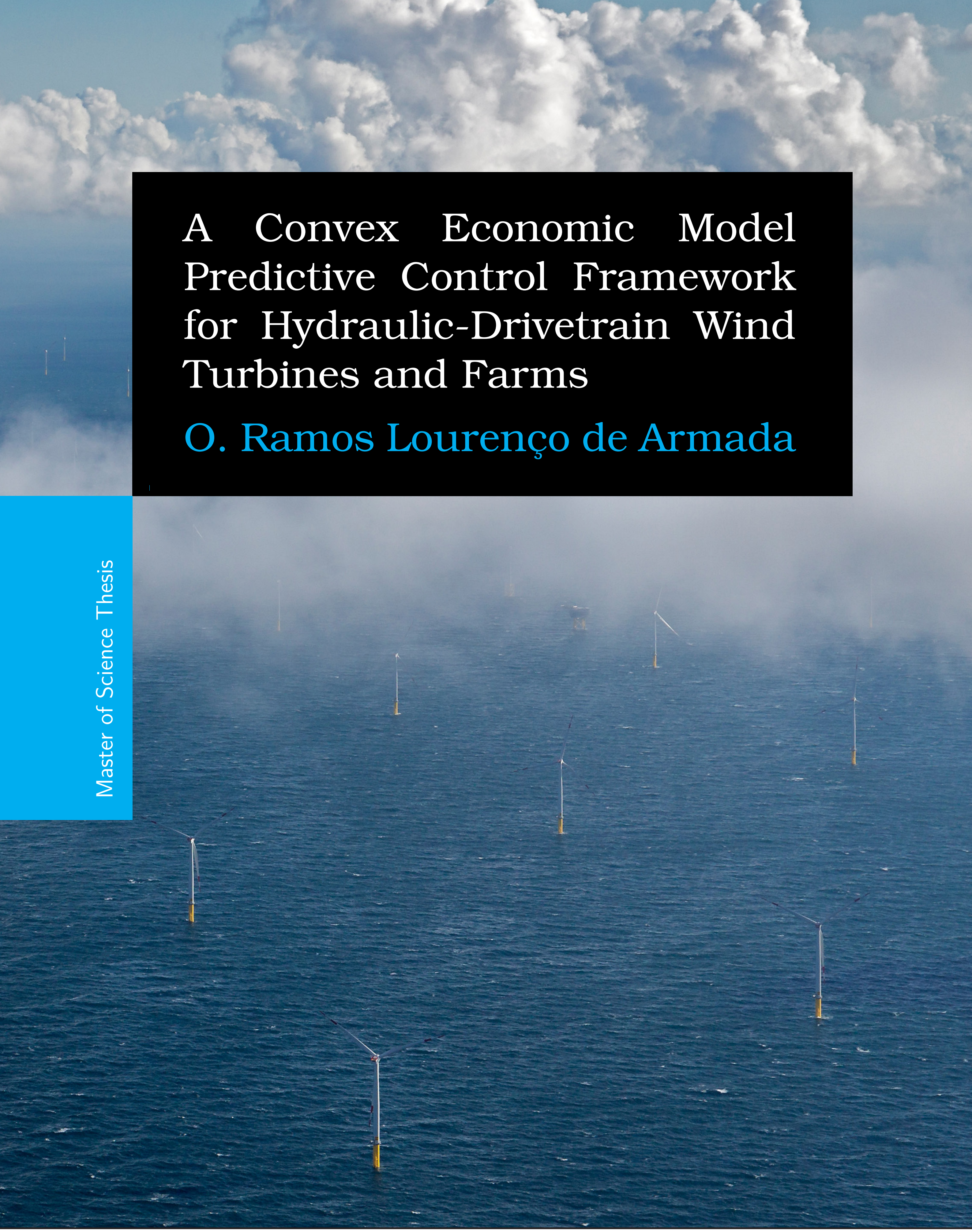

A Convex Economic Model Predictive Control Framework for Hydraulic-Drivetrain Wind Turbines and Farms

O. Ramos Lourenço de Armada

Master of Science Thesis

Delft Center for Systems and Control

A Convex Economic Model Predictive Control Framework for Hydraulic-Drivetrain Wind Turbines and Farms

Master of Science Thesis

For the degree of Master of Science in Systems and Control at Delft University of Technology

O. Ramos Lourenço de Armada

April 2, 2022

Faculty of Mechanical, Maritime and Materials Engineering (3mE) · Delft University of Technology

The work in this thesis was supported by Delft Offshore Turbine and DOB-Academy. Their cooperation is hereby gratefully acknowledged.

Abstract

In the mission to slow down global warming, the replacement of fossil fuels by renewable energy resources is key. A tipping point in the adoption of renewable energy resources is notable, as they are becoming economically more viable. Offshore wind energy is considered essential in realizing the greenhouse gas emission reduction targets. However, high construction, installation, and maintenance costs cause offshore wind to remain in competition with fossil fuel-based energy. Therefore, further reduction of offshore wind energy costs is crucial.

The most common method of wind energy cost reduction is the upscaling of nominal power ratings by increasing the size of the rotor. However, an alternative way for attaining cost reductions might be the employment of a radically different hydraulic drivetrain concept. Hydraulic-drivetrain wind turbines have the potential of lowering the construction and maintenance cost of wind farms by using a shared hydraulic network. Hydrostatic power, generated by individual wind turbines, is transmitted to a central location where electrical power is collectively generated. However, challenges arise in the control of hydraulic-drivetrain wind farms, e.g., limited pump torque controllability and increasingly complex coupled dynamics for a rising amount of employed wind turbines.

Current control strategies for hydraulic-drivetrain wind farms are developed based on classical control methods. These methods become less suitable for maximizing the collective power of larger wind farms. Therefore, this thesis presents a modification of the existing convex economic model predictive control (CEMPC) framework for conventional wind turbines, such that it becomes compliant to the domain of single-turbine and multi-turbine hydraulic-drivetrain wind farms. The CEMPC method provides computational tractability by circumventing the nonlinear nature of the dynamics. A novelty in this work is that the CEMPC framework is scalable for the control of multiple wind turbines. Moreover, an additional algorithm is proposed to extend the applicability of this framework to control wind turbines containing digital displacement pumps.

In a simulation study, the performances of the developed CEMPC framework applied to a single-turbine and two-turbine hydraulic-drivetrain wind farm are compared for different wind speed scenarios. The proposed CEMPC framework shows its ability to adequately control the employed wind farms. When comparing the obtained power production efficiencies with a conventional wind farm employing NREL 5-MW reference turbines, the efficiency of the hydraulic-drivetrain wind farm is 10%-17% lower compared to the reference wind farm. To reduce the levelized costs of offshore wind energy, the hydraulic-drivetrain wind farm concept has to provide at least an equivalent cost reduction over the wind farm's lifetime. The scalability in the number of controlled turbines makes the proposed CEMPC framework for hydraulic-drivetrain wind farms a promising candidate for realizing the necessary cost reduction.

Table of Contents

Acknowledgments

Studying at home, or in an empty office, has been a part of my time graduating during the COVID-pandemic. Nevertheless, I have been surrounded by many, many supportive and vibrant people that made my graduation period surprisingly fun. Although it is impossible to mention every single person, this section aims at expressing my gratitude and love for these people.

Foremost, I want to thank my daily supervisor Sebatiaan Mulders, but for the sake of a chronological story, I will start with my leading supervisor Jan-Willem van Wingerden. Thank you for your continuous support throughout my Thesis. I admire your love for wind turbines, which got me excited about wind energy myself as well. I am grateful for the new insights and interesting papers you gave me during my literature survey. I am happy that you showed appreciation for the hard work that I have been delivering during this thesis project. Moreover, I am thankful that you matched me with my daily supervisor, Sebastiaan.

I would like to share my gratitude to the company Valcon to be boring enough for Sebastiaan to resign and become my supervisor (and continue his academic career at the TU Delft). Sebas, if there was a competition in being the best supervisor, you would have definitely gotten my vote. Your experience with the DOT system and knowledge of control made our brainstorming sessions at the DE Café very efficient and useful. Moreover, your involvement and enthusiasm in supervising me in my project encouraged me to invest time and hard work in this project. More importantly, you did not only show interest in my project, but also in me as a person. Chit-chatting about the weekend, interest, and future plans made our supervisor-student relationship amicable, which I doubt a lot of students experience. Therefore, as a thank-you and to investigate a future friendship, I want to treat you to a big pitcher of beer at the bar after I graduate!

I want to thank Rogier Dinkla, Chris Keidemeijer, and Niels Diepeveen for being my supervisors from the side of DOT. Although things didn't go as smoothly as planned, I am happy that all of you found the time to follow each other up as my supervisors. A special thanks to Rogier, who invested time to explain the features of his thesis, which were an inspiration for my work. Furthermore, I would like to show my gratitude to

Krithika from DOB-Academy, who created custom-made images especially for in this thesis, fancy figures! On that note, I would like to thank Barbara for helping me design this thesis cover. I would like to thank Desiree van Es for the random chats and for keeping me in the loop for DOT and DOB events as a graduate intern. Finally, I want to thank 'de Keuken' for making the delicious (and healthy!) meals, shakes, and cakes.

My love goes to all the master students I studied with at 'Study Landscape' at the TU Delft. We worked our asses off, blood, sweat, and tears were (literally) shed in that room. Thank you for pulling me out of my intense periods of focus, reminding me to also take breaks with you and drink the delicious coffee and choco provided by 'de zwevende pas'. The structure and conviviality provided by you got me through the days!

Without my housemates, the turbulent period of the COVID-pandemic would've been genuinely boring. I am happy that we found ways to circumvent this boringness that has struck so many other students. We have had a wonderful time playing board games, walking around the city during our 'corona wandelingetjes', going to parks in summer, and frequently throwing parties. I hope that we finally get a longer period of 'non-lockdown' to start discovering the hidden gems of Rotterdam! Dirk, Laurens, Tijmen, and Mark, with all my heart, thank you!

I would like to thank my mother, Linda, for randomly ringing the bell in Rotterdam to come and drink coffee or have lunch with me. Mom, thanks for all the love and support that you've given from birth up until now. In my opinion, this graduation is a great accomplishment for both of us! Also, I would like to show my gratitude to my brother, Ngui. I am really happy that we see each other more often than a few years ago when we were discovering our student lives. I enjoy chilling and having interesting discussions together. I am proud to see that you are sailing your own course in your study and progressing every time we see each other. I am impressed at your calm and caring interviewing skills, asking the right questions. I know you will become a great psychologist!

Carmen, I adore the endless love and support that you have given me the past years, starting from the moment that we joined the same project group, WB43, building an unnecessary large hydraulic water pump. After all these years, we, fortunately, have not gotten tired of each other yet, on the contrary, our bond and joy together have only grown. I am proud of how you dashed through your graduation project, and I will respectfully accept that you've won the race by graduating two weeks before me. I get super excited at the prospect of us using the power of the wind and sea, not for generating electricity with offshore wind turbines, but for (kite)surfing during the future trips with our campervan!

Oyono Ramos Lourenço de Armada
Rotterdam, March 2022

Chapter 1

Introduction

In the past decades, it has been generally accepted that the extensive usage of fossil fuels causes severe damage to the environment. In 2019, fossil fuels accounted as the energy source for 86% of the world's direct primary energy consumption [7]. With a rising world population and developing economies in, e.g., Asia and Africa, it is highly presumable that the overall energy demand will continue to increase [49]. Therefore, it is imperative to shift from fossil towards more renewable sources of energy.

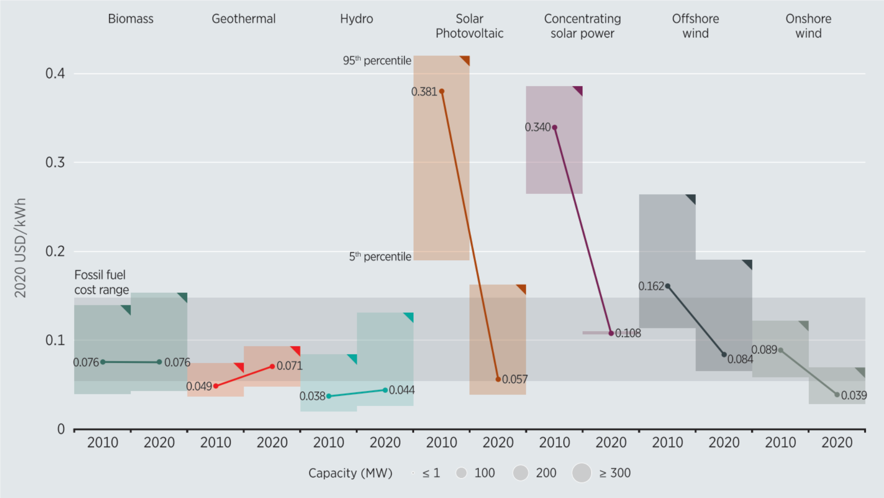

Figure 1-1: Global LCOEs from newly commissioned, utility-scale renewable power generation technologies, 2010-2020. The global weighted-average LCOE values are shown, the bands of the colored boxes represent the 5th and 95th percentile bands for renewable projects. The gray horizontal box denotes the cost range of fossil fuels [33].

Up until recently, fossil fuels have been financially most price competitive, and therefore, the most extensively used energy resource in society and industry [33]. Investment and development in renewable energy technologies, encouraged by authority incentives such as the Paris Climate Agreement [67] and the European Green Deal [25], have significantly reduced the levelized cost of energy (LCOE) of green energy resources [33], as visible in Figure 1-1. In Europe, a large portion of future renewable energy capacity is envisioned at offshore sites. The deployment of turbines in wind farms at offshore locations eliminates design and operation limits due to issues like spatial occupancy, cast shadow, and noise constraints [25]. Moreover, wind speeds are generally higher offshore [22, 77]. Compared to onshore wind energy, offshore construction costs are typically 1.5 to 2 times higher due to the need for supports, foundations, and marine wiring [30]. Moreover, maintenance is technically and operationally more challenging on sea, and therefore more expensive than onshore maintenance operations [14]. Figure 1-1 shows that the LCOE of offshore wind energy is significantly higher than onshore energy, and is not ready to compete with the cheapest form of fossil fuel energy. To speed up the expansion of offshore wind power capacity, it is required to further reduce the LCOE of offshore wind.

1-1 Reducing the levelized costs of offshore wind energy

A commonly used method of reducing the costs of wind energy has been to upscale the nominal power rating of offshore wind turbines by increasing the size of the rotor [10, 26]. This significantly decreased the LCOE, resulting in the first tenders for subsidy-free offshore wind farms to be built in the Netherlands by 2022 [78]. However, further cost reductions are necessary to facilitate wind power capacity growth, such that climate goals can be achieved [78].

Another method of reducing the LCOE is clustering wind turbines in a wind farm. This enables the use of shared electrical infrastructure, leading to a reduction of construction and maintenance costs [71]. However, a more dense layout increases the chance of wake interaction among wind turbines. This negatively affects the wind quality of downstream turbines, inducing increased turbine loads and reduced power outputs, resulting in a suboptimal farm operation. To address the negative effects of wakes, wake control (WC) is starting to play a significant role [2, 21, 27, 73].

Maintenance still accounts for 20-25% of the total LCOE of current wind power systems [14]. Lowering the frequency and cost of maintenance will therefore have a significant impact on the profitability of wind farms. Early-fatigue damage can often be attributed to the direct coupling of the drivetrain to the rotor, which is subjected to dynamical loads induced by turbulent wind fluctuations. Especially, the gearbox in conventional wind turbines is sensitive to wear and is the main contributor to maintenance costs [51]. Hydraulic systems could be an alternative to conventional maintenance-critical wind turbine drivetrains. In many industries, hydraulics have proven to be efficient under harsh conditions and undergoing heavy loads [17, 43].

Conventional high-maintenance and heavy mechanical and electrical components, which are located in the nacelle, can be replaced by a hydraulic pump. This is graphically shown in Figure 1-2. The pump uses the mechanical power harvested from the wind to create a high-pressure fluid flow, which is transmitted through a hydraulic network towards a centralized mechanical hydro-turbine. The energy contained in the flow is used to drive the rotation of a generator shaft. The robustness of the hydraulic components and improved torsional dynamics, due to added damping of the fluid medium, can substantially stretch the expected lifetime of wind turbines. Moreover, it enables operation at lower wind speeds, lower tip-speed ratio (TSR), and higher torques [43]. Furthermore, hydraulic components have a high power density and, hence, could facilitate a weight reduction of the head mass. As the head mass of the nacelle appears in several design criteria for the turbine tower design [30], this might enable a reduction of structural material and costs of the wind turbine tower. Finally, a hydraulic drivetrain enables centralized power production of multiple hydraulic-drivetrain wind turbines (HWTs) using a single hydro-turbine. This should minimize the number and total volume of maintenance-sensitive electronic equipment [17]. Finally, the hydro-generator can be placed in an accessible location close to sea level [12, 50].

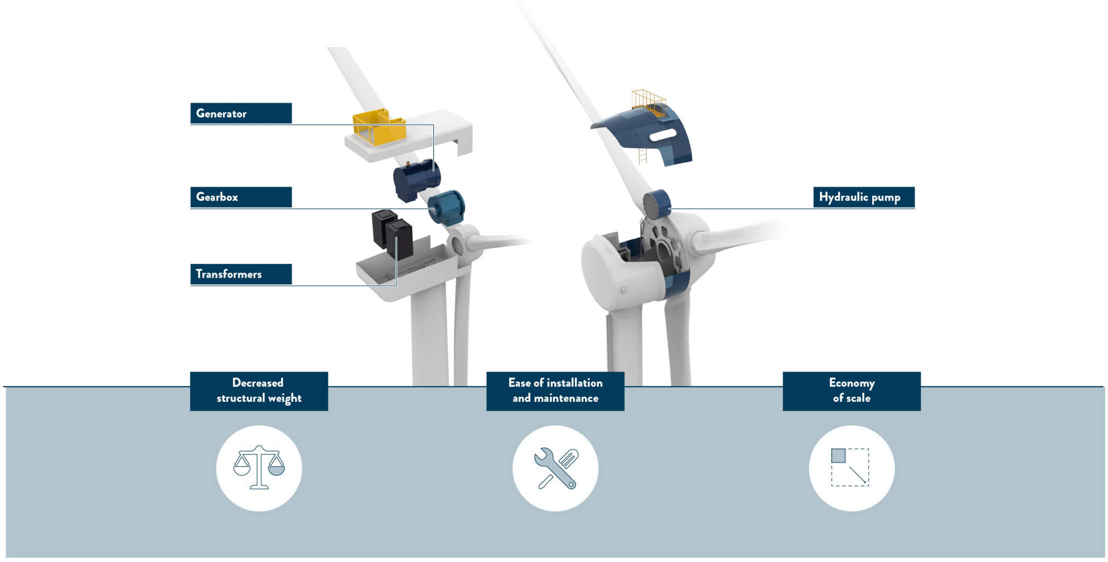

Figure 1-2: Component reduction in Delft Offshore Turbine hydraulic-drivetrain wind turbine nacelles. High-critical mechanical and electrical components of a conventional wind turbine are replaced by a single hydraulic pump, which is directly coupled to the rotor shaft. This results in a decrease in nacelle weight, and maintenance needed.

1-2 Hydraulic-drivetrain wind power plants

The introduction of hydraulic transmission systems in the wind industry provides new possibilities by allowing the combination of fluid power from multiple wind turbines for centralized power generation. In literature, two fluid transmission systems are mainly discussed: closed-loop oil-based transmission systems [9, 17, 43] and open-loop seawater-based transmission systems [17, 35, 70, 72]. A disadvantage of oil-based transmission systems is that an extensive amount of mineral oil is utilized, with risks of oil leaks and fire hazards [35]. The adoption of seawater-based hydraulic drivetrains enables the prospect of using ocean thermal energy conversion (OTEC) [70], reversed osmosis (RO) for the desalination of seawater [64, 72], and hydrogen generation [34].

Delft Offshore Turbine (DOT) is a Dutch company developing wind turbines with a seawater-based open-loop hydraulic drivetrain for centralized electricity generation using a Pelton turbine, as illustrated in Figure 1-3. The HWTs utilizes the power harvested from the wind to generate high-pressure water flows using digital displacement pumps (DDPs). The water streams, generated by multiple turbines, are transmitted through a shared hydraulic network, leading to a spear valve. At the nozzle, the pressurized flow is converted into a high-velocity jet driving the rotation of a Pelton turbine, which is mechanically coupled to a generator. Field experiments have been conducted with a HWT prototype, the DOT500, at Maasvlakte II and Princess Amalia Wind Farm [44]. The tests were erected as a proof of concept, where it is shown that the turbine was able to obtain a decent power production by governing the rotor speed.

1-3 State-of-the-Art hydraulic-drivetrain wind turbine control

Single-turbine control

In single wind turbine control, the control strategy is typically based on four wind speed regions, as shown in Figure 1-4. Region 1 represents the region where the power in wind is not deemed sufficient to operate the turbine to produce power and the turbine is maintained out of operation.

When the wind speed surpasses the cut-in wind speed and enters Region 2, the below-region wind speed conditions allow for power generation. The control objective in this region is to maximize wind power extraction, also referred to as maximum power point tracking (MPPT), to produce as much electrical power as possible. In conventional wind turbines, this is achieved by maintaining fine-pitch and tracking the optimal TSR by controlling the generator torque on the rotor shaft [48]. In HWTs the counter-torque on the rotor shaft is delivered by the pump. The pump torque is regulated by controlling the pressure in the discharge line by combined control actions of varying the pump displacement and manipulating the position of the spear valve [44]. When the wind speed surpasses the rated value in Region 3, the aerodynamic rotor power is

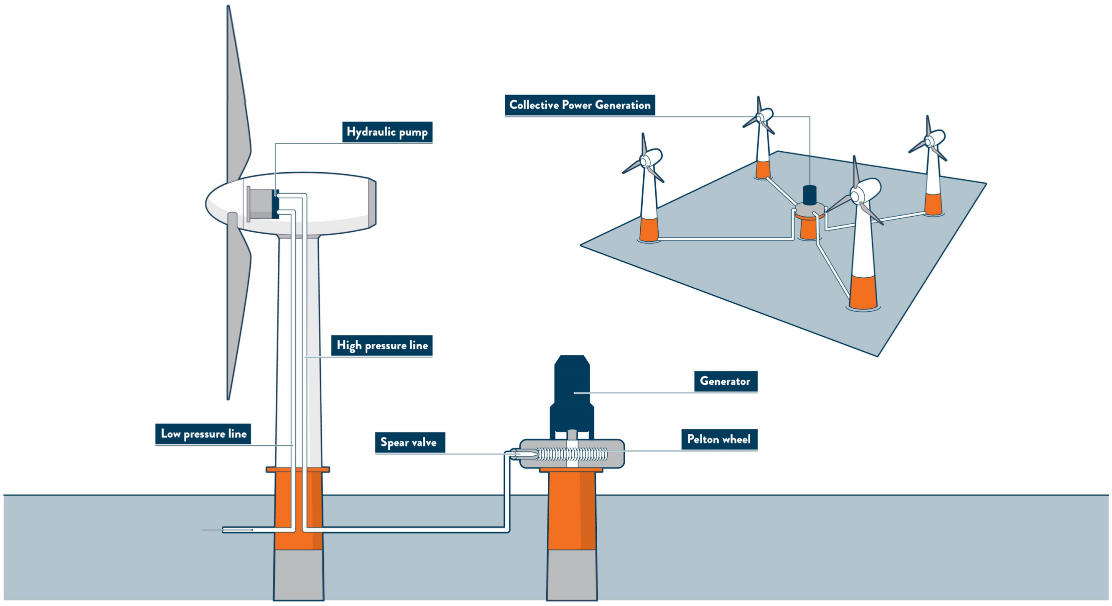

Figure 1-3: A graphical overview of a DOT wind power plant. Wind energy is captured by the wind turbine blades and transformed into a pressurized flow by the pump. This flow is transferred through a hydraulic network towards the spear valve, where the flow is transformed into a high-velocity water jet that drives the rotation of the Pelton runner and mechanically coupled generator. Multiple hydraulic-drivetrain wind turbines can be connected to the Pelton turbine using a shared hydraulic network or parallel hydraulic pipelines.

purposely reduced by regulating the blade pitch angle to guarantee the wind turbine to operate within its design limitations. The control objective hence changes from power maximization to limiting power by intentionally reducing rotor efficiency. When the wind speed exceeds the cut-out limit, the wind turbine operation is shut down and the rotor is fixated to prevent structural damage. The remainder of this work will only regard the control in regions 2 and 3.

In previous work, the control of single-turbine hydraulic-drivetrain wind farms (HWFs) containing a fixed-displacement pump [16, 17, 43, 44, 69] and continuously variable displacement pump (CDP) [17, 68] is investigated. It is found that for single-turbine HWFs a passive spear valve control strategy is sufficient for decent turbine performance in wind region 2 and 3. Nevertheless, an active spear valve control technique to keep the pressure at the nozzle at a nominal value, significantly improves the power generation efficiency of the turbine. A DDP is implemented in [9], however, when inspecting the pump control method and simulation results, the discrete nature of the pump displacements seem not considered. Instead, a continuous range of available pump displacements appear to be realizable, which may be a valid assumption for a pump with an abundance of pump chambers. The systems in the abovementioned works are all controlled using classical control methods using proportional-integral-derivative (PID) type controllers.

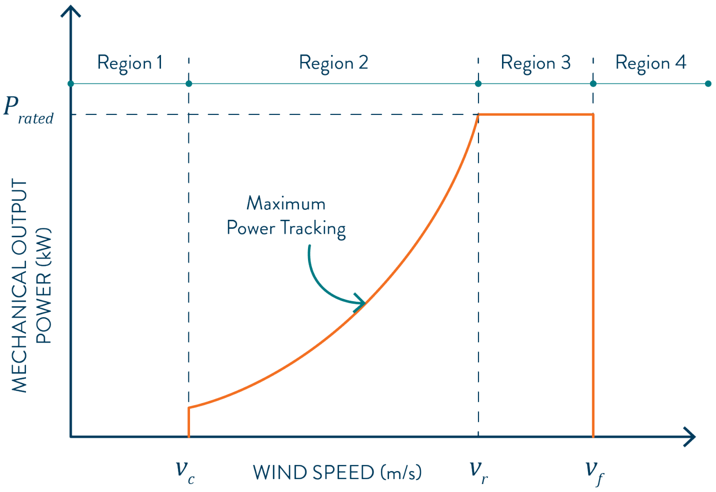

Figure 1-4: A typical wind turbine control strategy. In Region 1 the wind power is not sufficient for the turbine to produce electrical power. As the cut-in wind speed v_c is surpassed in region 2, also known as the below-rated wind speed region, a power maximization objective is enacted. As the turbine design limits are reached at rated wind speed v_r in region 3, the objective changes to maintaining the wind turbine within its design limits by intentionally decreasing its efficiency. When the wind speed exceeds the cut-out wind speed v_f in region 4, the wind turbine rotor is fixated to prevent structural damage.

Multi-turbine control

When expanding to an array of multiple HWFs sharing the same hydraulic drivetrain, several challenges arise. Research on the control of multi-turbine HWFs for the DOT concept has been performed in [35] and [70] for systems with CDP and fixed-displacement pumps, respectively.

The results in [35] show that, due to economic and performance benefits, a shared hydraulic network is preferred over parallel hydraulic pipeline connections to the Pelton turbine. Furthermore, active spear valve and variable displacement pump control strategies are shown to be more efficient than passive spear valve and fixed-pump displacement control strategies, respectively. The author notes that when wind turbines are connected through a shared hydraulic network, the challenge arises that only the nozzle pressure can be controlled to provide torque control of all connected wind turbines. Therefore, the connected turbines experience similar hydraulic torque feedback on their rotors, but dissimilar aerodynamic torques due to the different effective wind speeds that they are subjected to. The author shows that without proper active pitch control to steer the pressure towards the nominal value, turbines experiencing high wind speeds accelerate at the cost of the deceleration of wind turbines experiencing lower wind speeds. For large wind speed differences throughout the farm, this may cause wind turbines experiencing high wind speeds to prematurely reach their rated angular velocity, and hence blade pitch control is necessary for below-rated conditions. The latter results in suboptimal farm operation. Moreover, the turbines experiencing low wind speeds may come to a standstill. Therefore, a proportional-integral (PI) feedback controller and a cascade controller compensation are used to alter the linear position of the spear valve, such that nominal pressure is maintained.

The author in [70] shows that the performance of multi-turbine HWFs containing fixed-displacement pumps and a shared hydraulic network is limited due to loss in controllability of the individual pump torques. As the displacements of the pumps are fixed, the pump torque control of all wind turbines is completely dependent on the pressure feedback regulated by the single spear valve in the hydraulic network. As all wind turbines experience different wind speeds and therefore need different pump torques to obtain optimal wind power capture, suboptimal performance can not be circumvented. A varying control strategy, scheduled on the wind speed regions experienced by the wind turbines in the farm, is developed to control the spear position in an attempt to maximize the obtainable farm power.

1-4 The potential of model predictive control for hydraulic-drivetrain wind turbines

1-4-1 Challenges in the control of hydraulic-drivetrain wind turbines

As DDPs have a finite discrete set of realizable pump displacements and the pump torque is dependent on the pump displacement and employed pressure. The realizable pump torque for any arbitrary pump pressure is hence also a discrete set of values. Therefore, the control of multi-turbine HWFs with DDPs has similar control challenges as described in the previous two paragraphs. It is likely that the pump torque, required to steer the rotor towards optimal TSR, is typically not realizable. Therefore, the attainable aerodynamic efficiency of individual turbines is limited. This results in inevitable suboptimal farm operation when experiencing deviating wind speeds throughout the park. It is important to find a multivariable control strategy maximizing the overall attainable HWF performance by finding a suitable spear valve position, blade pitch angles, and realizable volumetric pump displacements.

The turbine dynamics are coupled through the shared hydraulic network, causing turbine interaction. As the HWF concept is scalable in the number of wind turbines, the employed system model can become large and the coupled dynamics complex. Therefore, the control problem of maximizing the power of the multi-turbine HWF becomes increasingly hard for a rising number of connected wind turbines. Moreover, keeping the system within its design limits becomes less straightforward. Therefore, the system may become difficult to be controlled using classical control methods that do not explicitly consider the coupled system dynamics. The multi-input, multi-output (MIMO) nature of a multi-turbine HWF system model makes it interesting to use multivariable control methodologies for the control of larger HWFs.

1-4-2 Solutions from model predictive control

Model predictive control (MPC) has several positive attributes that render the method useful for the control of HWFs. The method is well suited for the control of, e.g., multivariable control applications [38], complicated dynamic system behavior [13], and non-minimum phase system dynamics [40]. Moreover, it has preview information capabilities [18]. The three most important advantages of MPC, when compared to other multivariable control techniques are arguably: (1) the capability to handle both hard and soft constraints on the system's states, inputs, and outputs; (2) the ability to consider multiple competing control objectives; and (3) the possibility to take the predicted future in consideration. It must be noted, however, that the MPC's performance and usefulness are dependent on the accuracy of the employed internal system model and used measurements and estimates. Solutions for this problem have been found in adaptive MPC structures that minimize model errors using online model correction, and robust methods accounting for disturbance uncertainties [24, 60]. A drawback of using MPC is that the computational complexity of the control problem may increase significantly. This complexity is mainly dependent on the size and nature of the plant model [53, 54].

Conventional MPC applications are commonly used for set-point tracking. Set-points usually represent the relevant optimal steady-state, but are typically picked without considering how this equilibrium should be reached. As a result, specifically in processes where the reference changes faster and more frequently than the relevant states, conventional MPC methods may perform suboptimally [52]. In economic model predictive control (EMPC) there is no set-point [60]. Instead, EMPC merely seeks to optimize a given cost function that reflects real costs and benefits.

To alleviate the computational burden, the use of a state-of-the-art convex economic model predictive control convex economic model predictive control (CEMPC) framework for wind turbine control [18, 31, 57] seems very promising. The method is able to circumvent the nonlinear wind turbine dynamics using an internal control model. A change of variables is used to describe the wind turbine dynamics as a linear function. As a result, the optimization problem that has to be solved becomes convex. This allows the wind turbine controller to use convex optimization algorithms, rendering the optimization problem computationally tractable by providing globally optimal solutions.

Although the characteristics of the state-of-the-art CEMPC framework are very promising, the existing framework is only applicable to conventional wind turbines. To provide the possibility to use the CEMPC method for HWTs, it would be valuable to modify the current CEMPC framework for the control of single-turbine and multi-turbine HWFs.

1-5 Thesis goals and approach

In the pursuit of commercial deployment of HWFs, the expansion to an array of multiple turbines is imperative. The addition of turbines to a HWF introduces multiple control challenges, i.a., complex coupled system dynamics and limited pump torque controllability. This renders the control objective of plant power maximization while considering the system constraints to become increasingly hard for the number of applied wind turbines.

The state-of-the-art CEMPC framework for conventional turbines seems to be a promising candidate for the control of the multivariable plant system, considering an overall plant power maximization objective and constraint handling. Moreover, the method provides computational tractability by circumventing the nonlinear nature of the HWF dynamics. However, the current CEMPC framework is not suitable for the use of controlling HWTs, or HWFs.
Based on the previously stated, the goal of this thesis is formulated as follows:

Thesis goal: Develop a CEMPC framework, maximizing the overall power generation of individual hydraulic wind turbines and multi-turbine hydraulic wind farms.

The presented thesis goal is somewhat broad and general. To provide some context and sketch the approach in fulfilling the main goal, different subgoals are formulated, which align with the previously introduced challenges.

As the CEMPC method relies on numerical methods, a simulation study is performed as a proof of concept. To this end, a HWF simulation model is key for the evaluation of the proposed controller framework. Additionally, it is necessary to develop an internal control model that represents the abovementioned simulation model, but is compliant with the requirements of the CEMPC framework. Towards the development of the aforementioned models, the following research question is formulated:

I: How to develop an adequate, turbine scalable hydraulic-drivetrain wind farm simulation model for evaluation purposes, and how can this model be modified for the use as an internal control model in the CEMPC framework?

Due to differences in working principles, control variables, and system constraints of the conventional and hydraulic-drivetrain wind turbine concepts, the existing CEMPC framework for conventional wind turbines is not applicable for HWTs. Moreover, the current framework is designed to optimize the generated power of a single wind turbine, where for the hydraulic drivetrain concept it is important that the combined generated power of all connected wind turbines is maximized. Therefore, the subgoal is formalized by the following research question:

II: How is the existing CEMPC framework for conventional turbines altered for the control of single-turbine and multi-turbine hydraulic-drivetrain wind farms?

When controlling HWTs containing a DDP, the choice of pump displacements is restrained to a finite set of realizable settings. The limited pump displacement selection range has consequences for wind turbine and wind farm performances. Moreover, the control challenge arises on how to identify and select the desired available pump settings. For this reason, the following research question is formulated:

III: How can the control of digital displacement pumps be incorporated within the in **II** developed CEMPC framework? And how does the performance differ when controlling turbines containing continuously variable displacement pumps and digital displacement pumps?

The developed controller framework for HWTs contains a novel characteristic, namely the ability to control multiple HWTs with the objective of collective power maximization. To evaluate the performance of the developed controller framework, simulation studies are performed, aiming to answer the following subquestion:

IV: Is the established CEMPC framework, capable of adequately controlling both single hydraulic-drivetrain wind turbines and multi-turbine hydraulic-drivetrain wind farms? How does the overall power generation performance change when extending towards a multi-turbine wind farm, and what is the performance compared to conventional wind turbines?

1-6 Thesis outline

This section presents the outline of this thesis. Each of the paragraphs gives a brief summary of the contents in each chapter.

Chapter 2 provides the theoretical background and (dynamic) modeling of single-turbine and multi-turbine hydraulic-drivetrain wind farms. Moreover, the implementation of a simulation model is provided.

Chapter 3 provides the theoretical background of the proposed scalable CEMPC method for single and multi-turbine CDP-HWFs. It describes the development of the predictive convex internal control model and outlines its use in the CEMPC optimization problem.

Chapter 4 presents the implementation of the theoretical CEMPC framework. Moreover, it discusses additional practical considerations to increase the accuracy and performance of the controller framework.

Chapter 5 extends the introduced CEMPC frameworks to the domain of controlling DDP-HWFs by introducing an additional algorithm to control the pump displacements.

Chapter 6 presents the results of the conducted simulation study. Different wind speed profiles are used to reveal the behavior and performance of the scalable CEMPC for CDP and DDP HWFs.

Chapter 2

Hydraulic-Drivetrain Wind Power Plant: Theory and Modelling

The novelty of hydraulic-drivetrain wind farm (HWF) is that it uses seawater-hydraulics as power transmission. This creates an opportunity for collective power generation using a shared hydraulic network, which in turn may allow the reduction of levelized cost of energy (LCOE), described in Section 1-2.

This chapter elaborates on the working principles and mathematical modeling of the components of a HWF containing one, or multiple wind turbines. A graphical overview of the power conversion throughout the HWF is depicted in Figure 2-1. The energy contained in the wind is captured by the wind turbine blades, providing the rotor shafts with mechanical power. This mechanical power is used to drive the hydraulic pumps, resulting in pressurized flows of seawater. The hydrostatic energy carried by the pressurized flows from all the wind turbines is transmitted to the centralized spear valve of the Pelton turbine through a shared hydraulic network. In the nozzle of the spear valve, the hydrostatic energy is converted to hydrodynamic energy by transforming the pressurized flow into a high-velocity jet. The energy of the high-velocity jet is captured by the buckets of the Pelton runner wheel, converting it into rotational mechanical energy. The generator, which is mechanically coupled to the Pelton runner shaft, finally converts the mechanical energy into electricity.

The remainder of this chapter is structured as follows: Section 2-1 discusses wind energy capture by the wind turbine rotor and the corresponding dynamics. Section 2-2 describes the working principles of the hydraulic pump. Section 2-3 describes the hydraulic network. Section 2-4 explains the spear valve. The Pelton turbine is explained in Section 2-5. The implementation of the system model is described in Section 2-6.

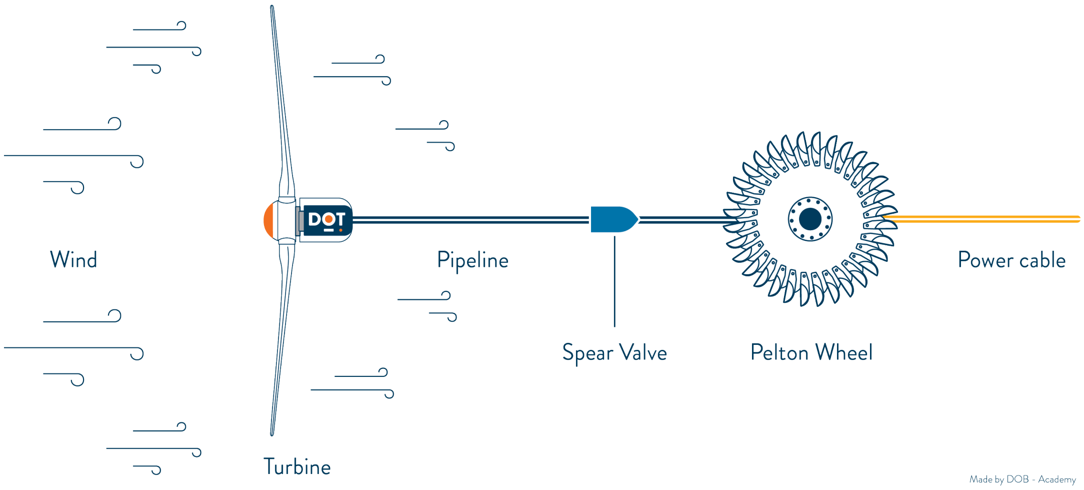

(a) A simplified overview of a single-turbine configuration of the wind farm.

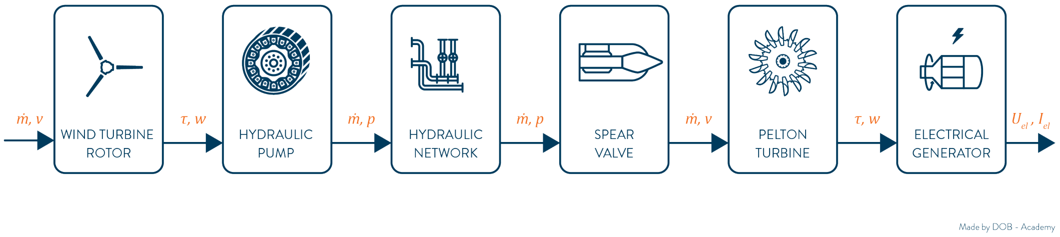

(b) A graphical overview of the power transmission.

Figure 2-1: A graphical overview of a hydraulic-drivetrain wind power plant. (a) An overview of a single-turbine farm configuration. (b) A simplified overview of the power transmission in the system. The kinetic wind energy, which is described by a mass flow of air $\dot{m}$ with a velocity v, is captured by the wind turbine blades and transformed into rotational mechanical rotor power, described by a torque τ and rotational speed ω. This power is used to drive a hydraulic pump, which transforms the power in a pressurized mass flow of water with pressure p. This flow is transferred through a hydraulic network towards the centralized spear valve. Here, the pressurized flow is transformed into a high-velocity water jet, which exerts torque and induces rotational mechanical power of the Pelton turbine, which is connected to a generator shaft. Here, the mechanical power is finally converted into electrical power, defined by the voltage U_{el} and current I_{el}.

2-1 Wind turbine rotor

The process of energy extraction by turbine rotors can be described by using the actuator disk model [3]. In this model, the available wind power is described by the kinetic energy

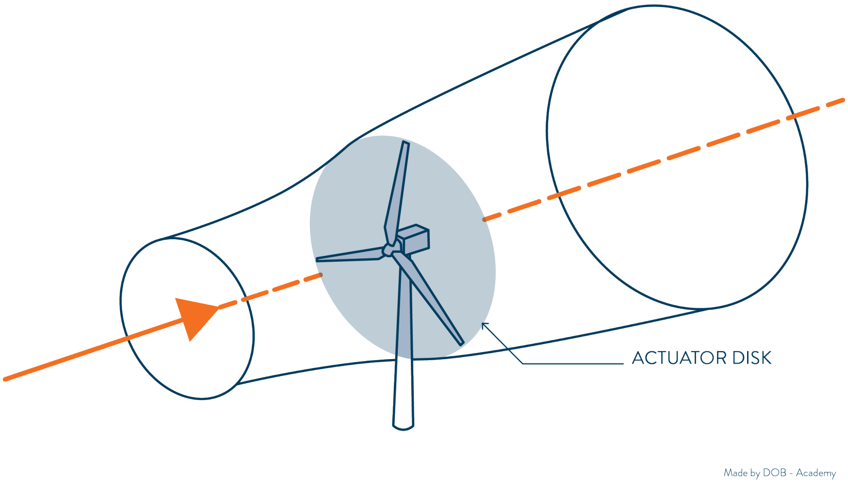

Figure 2-2: Graphical representation of the airflow passing the rotor swept actuator disk area. When using the actuator disk theory, the total available wind power P_w is defined as the kinetic energy of the wind that passes this disk, which is dependent on the mass flow through the disk and the rotor-effective wind speed v.

of the wind that passes a fictive disk, which is defined as the effective rotor swept area, illustrated in Figure 2-2,

$$P_\mathrm{w} = \frac{1}{2}\rho_\mathrm{a} A v^3, \tag{2-1}$$

where ρ_a is the air density, $A = \pi R^2$ is the rotor area with a rotor radius of R, and v is the effective wind speed over the rotor surface, known as the rotor-effective wind speed.

The rotor energy capture efficiency of wind energy by the turbine rotor is reflected by a variable called the power coefficient C_P, and is defined as the ratio between captured aerodynamic rotor power P_r and the available wind power P_w:

$$C_\mathrm{P}\left(\beta, \lambda\right) = \frac{P_\mathrm{r}}{P_\mathrm{w}}, \tag{2-2}$$

in which $\{\beta \subset \mathbb{R} \mid \beta_\mathrm{min} \leq \beta \leq \beta_\mathrm{max}\}$, is the collective blade pitch angle, with constant minimum and maximum value β_min and β_max, and λ is the tip-speed ratio (TSR), defined by

$$\lambda = \frac{\omega R}{v}, \tag{2-3}$$

where ω is the angular velocity of the rotor, also known as the rotor speed. Blade pitch actuator dynamics are defined by a first order actuator model:

$$\dot{\beta} = \frac{1}{t_\beta}\left(\beta_\mathrm{ref} - \beta\right), \tag{2-4}$$

in which t_β is the time constant and β_{ref} the reference angle, which can be derived by a controller.

The actuator disk theory shows that C_{P} is limited by the Lanchester-Betz-Joukowsky limit [46]. This theory states that turbines can not extract more than 59.3% of the kinetic energy from the airflow passing the blades. The power coefficient's dependency on the blade pitch angle and tip speed ratio is often obtained from simulation software or experimental data. In this thesis, the C_{P} curves from the baseline NREL 5-MW turbines [20] are used. As seen in Figure 2-3, this function is clearly nonlinear.

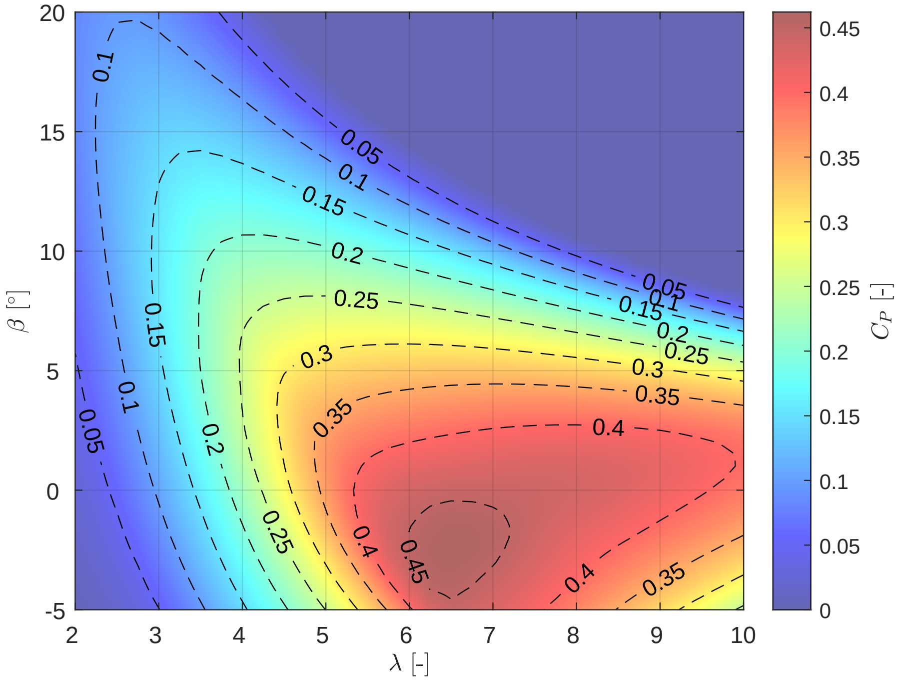

Figure 2-3: The power coefficient as a function of the TSR and blade pitch angle $C_{\text{P}}(\beta, \lambda)$ of the NREL 5-MW reference turbine [20].

The total aerodynamic wind power that is extracted by the rotor blades is given by

$$P_{\text{r}} = \frac{1}{2}\rho_{\text{a}} A C_{\text{P}}(\beta, \lambda) v^3. \tag{2-5}$$

The captured power results in an aerodynamic rotor torque, which induces rotation. The equation can be obtained by dividing (2-5) by the rotor speed:

$$\tau_{\text{r}} = \frac{1}{2}\rho_{\text{a}} A \frac{C_{\text{P}}(\beta, \lambda) v^3}{\omega}. \tag{2-6}$$

The simplified rotor speed dynamics of a hydraulic-drivetrain wind turbine can be described by the Newton law for rotational motion:

$$\dot{\omega} = \frac{1}{J}\left(\tau_{\text{r}} - \tau_{\text{p}}\right), \tag{2-7}$$

where $\dot{\omega}$ is the rotational acceleration of the rotor, J is the total rotational inertia of the drivetrain, and τ_p is the counter-torque on the rotor, delivered by the pump in hydraulic-drivetrain wind turbines (HWTs).

Maximum power is extracted by the rotor when it operates at optimal TSR, which is defined by the available power coefficient table. As the optimal TSR is equal for all wind speeds, the optimal condition can be translated to a certain optimal rotor speed when experiencing a specific rotor-effective wind speed. The variable rotor speed is controlled by regulating the torque imbalance on the rotor shaft, shown in (2-7), which can be influenced in several ways. The power coefficient, and therefore the rotor torque, are affected by altering the collective blade pitch angle. In wind farm control techniques such as wake steering and wake induction control, it is even possible to exert influence on the rotor-effective wind speed, which in turn affects the rotor torque. Note that the value of the optimal rotor speed changes as the rotor-effective wind speed changes. Finally, the pump torque can be controlled. The pump torque is dependent on a controllable pump displacement and the pressure in the hydraulic network, which can be indirectly regulated. This will be further explained in the following sections.

2-2 Hydraulic pump

The rotor shaft is directly coupled to the pump. Its rotational energy is used to pump seawater towards the Pelton turbine. Moreover, regulating the counter-torque of the pump is important in the variable-speed control of the rotor. In conventional-drivetrain wind turbines, the reactive torque on the rotor is directly regulated by controlling the generator torque. In hydraulic drivetrains, the pump torque is dependent on the controllable variable displacement of the pump and the pressure in the hydraulic network, which is regulated by the spear valve.

To reduce kinetic energy losses in pipelines, a low-velocity, high-pressure flow is preferred [70]. The most effective type of pump to achieve this is a positive displacement pump. The positive displacement principle refers to a fixed volume of fluid that is trapped and forced to move into a separate confined space. Where a continuously variable displacement pump (CDP) can realize all the values between the minimum pump displacement V_min and maximum pump displacement V_max, a digital displacement pump (DDP) only has a final set of available displacement settings dependent on the number of active piston chambers. This type of pump uses electronic solenoid valves to activate or deactivate pump chambers, which allows accurate and fast control of the pump displacement [63]. The discrete set of realizable pump displacement settings is described by

$$V_\mathrm{p} = n_{\mathrm{c},i} V_\mathrm{c}, \tag{2-8}$$

where V_p is the total volumetric displacement of the pump, $\{n_{\mathrm{c},i} \subset \mathbb{Z}^+ \mid 1 \leq n_{\mathrm{c},i} \leq n_\mathrm{c}\}$ is the number of active pistons with n_c the maximum number of active pistons, and V_c is the fixed volumetric displacement of a single piston chamber for a pump shaft revolution.

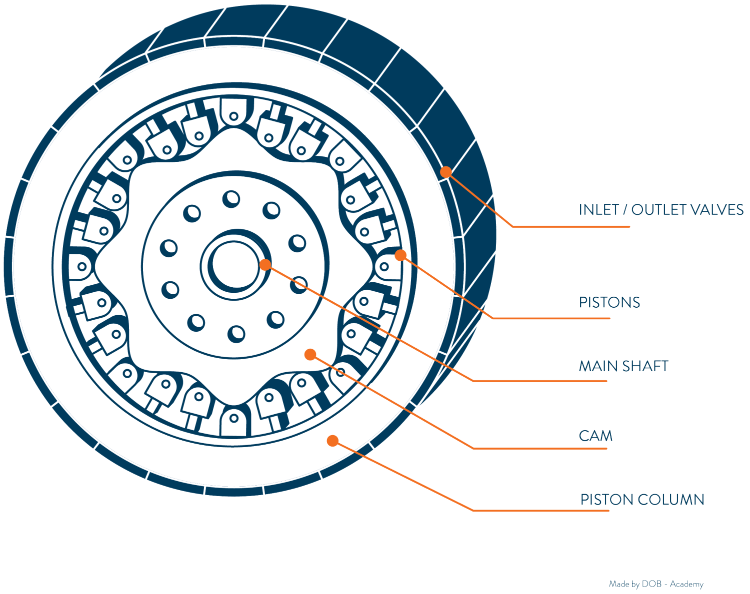

Figure 2-4: A graphical figure of the digital displacement pump. The main shaft is directly coupled to the wind turbine rotor. As it rotates, the cam drives the pistons in the piston column to make strokes and thereby generates a water flow.

When assuming a rigid driving shaft, the generated flow, torque of the pump are given by the following equations [44]:

$$Q_\mathrm{p} = V_\mathrm{p}\omega\eta_\mathrm{v}, \tag{2-9}$$

$$\tau_\mathrm{p} = \frac{V_\mathrm{p}\Delta p_\mathrm{p}}{\eta_\mathrm{m}}, \tag{2-10}$$

where ω is equal to the rotor speed, Q_p is the flow of water displaced by the pump, Δp_p is the pressure difference over the pump, given by $\Delta p_\mathrm{p} = p_\mathrm{p} - p_\mathrm{feed}$, where p_p is the pressure at the pump and p_feed is a known constant feed pressure, η_v and η_m are the pumps volumetric and mechanical efficiency, respectively. Note that the model used is a quasi-static model since inertial and capacitive terms for the pump are not considered. The efficiencies of a pump vary due to flow and pressure losses in the pump [42]. This will be explained in the following subsections.

A distinction is made between two types of powers, delivered by the pump,

$$P_\mathrm{p}^{(v)} = Q_\mathrm{p}\Delta p_\mathrm{p} = V_\mathrm{p}\omega\Delta p_\mathrm{p}\eta_\mathrm{v}, \tag{2-11}$$

$$P_\mathrm{p}^{(m)} = \tau_\mathrm{p}\omega\eta_\mathrm{v} = V_\mathrm{p}\omega\Delta p_\mathrm{p}, \tag{2-12}$$

which denote the volumetric and mechanical power, respectively. The symbol P_p is used to denote the volumetric power $P_\mathrm{p}^{(v)}$ for the remainder of this work, the mechanical pump is always denoted with a superscript.

2-2-1 Varying pump efficiencies

The flow production of a pump decreases for a pressure increase in the system, causing larger amounts of fluid leakage through clearances and gaps [65]. A simple description of the flow leakage is assumed and described by

$$Q_\mathrm{s} = C_\mathrm{s}\frac{\Delta p_\mathrm{p}}{\mu}, \tag{2-13}$$

where C_s is the laminar leakage coefficient, and μ is the dynamic viscosity of the considered fluid. The net flow generated by a pump is then given by

$$Q_\mathrm{p} = V_\mathrm{p}\omega - Q_\mathrm{s}. \tag{2-14}$$

The volumetric efficiency is defined as the ratio between the network flow including leakage losses and the ideal pump flow

$$\eta_\mathrm{v} = \frac{Q_\mathrm{p}}{V_\mathrm{p}\omega} = 1 - C_\mathrm{s}\frac{\Delta p_\mathrm{p}}{V_\mathrm{p}\mu\omega}. \tag{2-15}$$

Due to internal friction and flow resistance, the torque on the driving shaft of the pump must necessarily be larger than the ideal torque [65]. A more realistic description of the effective pump torque is given by [42]

$$\tau_\mathrm{p} = V_\mathrm{p}\Delta p_\mathrm{p} + \tau_\mathrm{f} + \tau_\mathrm{d}, \tag{2-16}$$

where τ_d is the additional torque due to damping properties of the fluid and τ_f is caused by fluid friction. The friction torque simulates the effect of dry friction forces on the pump pistons that oppose their motion [42]. It is proportional to the volumetric displacement and the pressure difference over the pump and given by

$$\tau_\mathrm{f} = C_\mathrm{f}V_\mathrm{p}\Delta p_\mathrm{p}, \tag{2-17}$$

where C_f is the dry friction coefficient of seawater. The damping torque describes the loss of torque due to fluid shear losses in small clearances between moving mechanical components [42]. It is proportional to the angular velocity of the pump shaft and is denoted as

$$\tau_\mathrm{d} = C_\mathrm{damp}V_\mathrm{p}\mu\omega, \tag{2-18}$$

where C_damp is the damping coefficient of water. The resulting torque produced by the pump is thus given by

$$\tau_\mathrm{p} = (1 + C_\mathrm{f})\,V_\mathrm{p}\Delta p_\mathrm{p} + C_\mathrm{damp}V_\mathrm{p}\mu\omega. \tag{2-19}$$

The mechanical efficiency is defined as the ratio between the ideal pump torque and the pump torque, including the added torque by fluid damping and resistance,

$$\eta_\mathrm{m} = \frac{V_\mathrm{p}\Delta p_\mathrm{p}}{\tau_\mathrm{p}} = \frac{1}{1 + C_\mathrm{damp}\frac{\mu\omega}{\Delta p_\mathrm{p}} + C_\mathrm{f}}. \tag{2-20}$$

The total pump efficiency η_{tot} is defined by the product of the volumetric and mechanical efficiencies,

$$\eta_{\text{tot}} = \eta_{\text{v}}\eta_{\text{m}} = \frac{1 - \frac{C_{\text{s}}}{V_{\text{p}}}\frac{\Delta p_{\text{p}}}{\mu\omega}}{1 + C_{\text{damp}}\frac{\mu\omega}{\Delta p_{\text{p}}} + C_{\text{f}}}. \tag{2-21}$$

The performance coefficients, C_{s}, C_{f}, and C_{damp} are assumed to be constant for this quasi-static pump model and chosen such that the rated efficiencies become $\eta_{\text{v}} = 0.98$ and $\eta_{\text{m}} = 0.98$ at nominal pressure and rated rotor speed. The total pump efficiency for values for different pump displacements and the combined parameter ratio $\Delta p/(\mu\omega)$ is shown in Figure 2-5.

It must be noted that Diepeveen found in [17] that accurate modeling of the efficiency of a real hydraulic pump is not possible with the empirically derived equations presented here. But, when operating in the right conditions, it does not deviate more than a few percent from real pump characteristics. In literature such as [55], the issue of modeling efficiency is omitted altogether. In this situation, a common approach is to use lookup tables of measured values, which, however, require accurate data. Since accurate data for digital displacement pumps for seawater is not available, and work is aimed at providing a proof of concept, the method described above suffices.

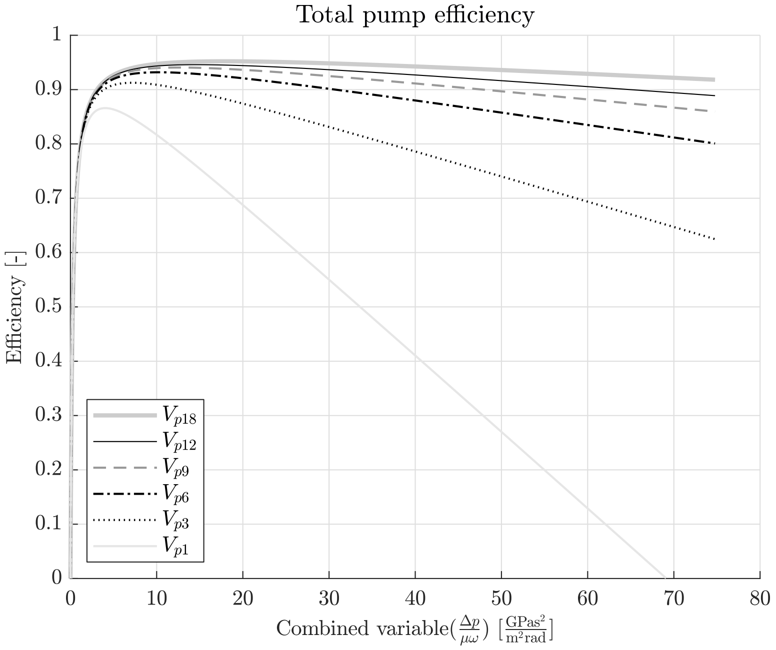

Figure 2-5: Total pump efficiency for different pump displacement settings. $V_{\text{p,i}}$ denote the displacements with i active pump pistons. For the sake of clarity, only the efficiency curves at 1, 3, 6, 9, 12, and 18 active pump chambers are shown.

2-2-2 Pump design

The digital displacement pump is one of the main features that Delft Offshore Turbine (DOT) introduces to the HWF concept, and is currently in development, but not commercially available yet. Therefore, the National Renewable Energy Laboratory (NREL) 5-MW reference wind turbine is taken as the blueprint for the pump design. The pump is assumed to operate at rated conditions at nominal network pressure to minimize kinetic losses. The maximum and minimum volumetric displacements are given by

$$V_{\mathrm{max}} = \frac{P_{\mathrm{p,mech}}}{\omega \Delta p_{\mathrm{p}}}, \tag{2-22}$$

$$V_{\mathrm{min}} = \frac{V_{\mathrm{max}}}{n_{\mathrm{c}}}. \tag{2-23}$$

A first-order actuator model is used to approximate the change in pump displacement due to opening and closing solenoid valves which activate or deactivate the piston chambers, respectively,

$$\dot{V}_{\mathrm{p}} = \frac{1}{t_{\mathrm{p}}} \left(V_{\mathrm{ref}} - V_{\mathrm{p}} \right), \tag{2-24}$$

where t_{p} is the time constant posed by the solenoid opening and closing rate and V_{ref} is the reference displacement, which is given by a controller.

2-3 Hydraulic network

The hydraulic network is used to transport pressurized water flow, generated by the pumps, towards the spear valve attached to the Pelton turbine. The analogies to modeling electrical and mass systems are used for the derivation of the hydraulic dynamics. The inertia, compressibility, and flow losses in the pipeline can be described as hydraulic induction L_{H} (mass), capacitance C_{H} (spring stiffness), and resistance R_{H} (damping), respectively [17]. A schematic representation of this principle is shown in Figure 2-6.

The abovementioned hydraulic characteristics can be used in combination with an analogy of a standard mass-damper-spring system driven by an external force F

$$F = m\ddot{x} + c\dot{x} + kx, \tag{2-25}$$

in which m is the mass, c the damping, and k the spring stiffness. For conversion to a hydraulic equivalent expressionFigure 2-6, the mechanical force is substituted by the pressure force $F = \Delta p A_{\mathrm{L}}$, with A_{L} the cross-sectional diameter of the pipeline. The mass in the pipeline is taken as $m = \rho_{\mathrm{w}} A_{\mathrm{L}} L_{\mathrm{L}}$, with L_{L} denoting the length of a pipeline segment, and ρ_{w} the fluid density. Finally, the fluid flow rate is defined as $\dot{x} = Q/A_{\mathrm{L}}$,

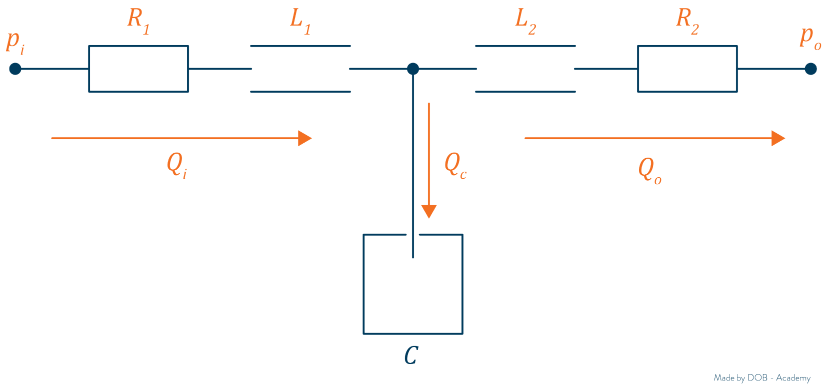

Figure 2-6: Schematic overview of a pipeline segment, described in the electrical analogy. The inlet-, net-, and outlet pressure and flow of the pipeline segment are represented by p_i, Q_i, p_c, Q_c, p_o, and Q_o, respectively. The hydraulic resistance, induction, and capacitance terms are denoted as R_1, R_2, L_1, L_2, and C, respectively

where Q is the flow through the pipeline segment. By rearranging terms, the following equation is obtained:

$$\Delta p = \frac{\rho_\mathrm{w} L_\mathrm{L}}{A_\mathrm{L}} \dot{Q} + \frac{c}{A_\mathrm{L}^2} Q + \frac{k}{A_\mathrm{L}^2} \int Q \ \mathrm{d}t, \tag{2-26}$$

which is further simplified into

$$\Delta p = L_\mathrm{H} \dot{Q} + R_\mathrm{H} Q + \frac{1}{C_\mathrm{H}} \int Q \ \mathrm{d}t. \tag{2-27}$$

This system equation contains an inconvenient circular dependency: the resistance term R_H is dependent on the flow through the pipeline, which is in turn dependent on the resistance term [76]. A linear parameter-varying (LPV) state-space model is used to capture the varying flow dynamics. The resistance term and system matrices are updated at every iteration to account for the nonlinearity in the resistive terms [9]. The following sections focus on obtaining state-space system representations of a single-turbine and two-turbine hydraulic network.

Single-turbine pipeline model

When modeling a single pipeline segment as displayed in Figure 2-6, it follows from the definition of the hydraulic properties in (2-27) that the following holds for each branch of the pipeline segment

$$p_{\mathrm{i}} - p_{\mathrm{c}} = R_1 Q_{\mathrm{i}} + L_1 \dot{Q}_{\mathrm{i}}, \tag{2-28}$$

$$p_{\mathrm{c}} - p_{\mathrm{o}} = R_2 Q_{\mathrm{o}} + L_2 \dot{Q}_{\mathrm{o}}, \tag{2-29}$$

$$p_{\mathrm{c}} = \frac{1}{C_{\mathrm{H}}} \int Q_{\mathrm{c}}, \tag{2-30}$$

where $\{p_{\mathrm{i}}, Q_{\mathrm{i}}\}$,$\{p_{\mathrm{o}}, Q_{\mathrm{o}}\}$, and $\{p_{\mathrm{c}}, Q_{\mathrm{c}}\}$ are the input, output, and net pressure and flow, respectively. The first two sets correspond to the values at the pump, and spear valve side of the pipeline, respectively. The quantities R_1, R_2 and L_1, L_2, denote the resistance and induction terms of the first and second branch of the pipeline segment, respectively.

Using the law of flow continuation, the net flow is

$$Q_{\mathrm{c}} = Q_{\mathrm{i}} - Q_{\mathrm{o}}. \tag{2-31}$$

Taking the derivative of (2-30) yields

$$\dot{p}_{\mathrm{c}} = \frac{1}{C_{\mathrm{H}}} Q_{\mathrm{c}}. \tag{2-32}$$

Substituting (2-31) in (2-29) results in

$$p_{\mathrm{c}} - p_{\mathrm{o}} = R_2 Q_{\mathrm{i}} - R_2 Q_{\mathrm{c}} + L_2 \dot{Q}_{\mathrm{i}} - L_2 \dot{Q}_{\mathrm{c}}, \tag{2-33}$$

which can be rearranged into

$$\dot{Q}_{\mathrm{c}} = \frac{R_2}{L_2} (Q_{\mathrm{i}} - Q_{\mathrm{c}}) + \dot{Q}_{\mathrm{i}} - \frac{1}{L_2} p_{\mathrm{c}} + \frac{1}{L_2} p_{\mathrm{o}}. \tag{2-34}$$

Finally, by substituting (2-32) in (2-34) the following equation is derived

$$\ddot{p}_{\mathrm{c}} = \frac{R_2}{C L_2} Q_{\mathrm{i}} - \frac{R_2}{L_2} \dot{p}_{\mathrm{c}} + \frac{1}{C} \dot{Q}_{\mathrm{i}} - \frac{1}{C L_2} p_{\mathrm{c}} + \frac{1}{C L_2} p_{\mathrm{o}}. \tag{2-35}$$

The dynamics of a single segment pipeline are fully captured by (2-32), (2-34), and (2-35). A state-space model is derived from the equations above. The inputs are chosen to be the input flow and output pressure, which can be controlled by the pump displacement and spear valve position, respectively. The outputs of the system are the input pressure at the pump and output flow at the spear valve. It is assumed that the pipeline branches have a constant and equal length and diameter, enabling the simplification $L_1 = L_2 = L_{\mathrm{H}}$. The resulting state-space equation is given by [70]

$$\underbrace{\begin{bmatrix} \dot{p}_{\mathrm{c}} \\ \ddot{p}_{\mathrm{c}} \\ \dot{Q}_{\mathrm{c}} \end{bmatrix}}_{\dot{x}_{\mathrm{N}}} = \underbrace{\begin{bmatrix} 0 & 0 & \frac{1}{C_{\mathrm{H}}} \\ \frac{-1}{C_{\mathrm{H}}L_{\mathrm{H}}} & \frac{-R_2}{L_{\mathrm{H}}} & 0 \\ \frac{-1}{L_{\mathrm{H}}} & 0 & \frac{-R_2}{L_{\mathrm{H}}} \end{bmatrix}}_{A_{\mathrm{N}}} \underbrace{\begin{bmatrix} p_{\mathrm{c}} \\ \dot{p}_{\mathrm{c}} \\ Q_{\mathrm{c}} \end{bmatrix}}_{x_{\mathrm{N}}} + \underbrace{\begin{bmatrix} 0 & 0 & 0 \\ \frac{1}{C_{\mathrm{H}}L_{\mathrm{H}}} & \frac{R_2}{C_{\mathrm{H}}L_{\mathrm{H}}} & \frac{1}{C_{\mathrm{H}}} \\ \frac{1}{L_{\mathrm{H}}} & \frac{R_2}{L_{\mathrm{H}}} & 1 \end{bmatrix}}_{B_{\mathrm{N}}} \underbrace{\begin{bmatrix} p_{\mathrm{o}} \\ Q_{\mathrm{i}} \\ \dot{Q}_{\mathrm{i}} \end{bmatrix}}_{u_{\mathrm{N}}}, \tag{2-36}$$

$$\underbrace{\begin{bmatrix} p_{\mathrm{i}} \\ Q_{\mathrm{o}} \\ Q_{\mathrm{c}} \end{bmatrix}}_{y_{\mathrm{N}}} = \underbrace{\begin{bmatrix} 1 & 0 & 0 \\ 0 & 0 & -1 \\ 0 & 0 & 1 \end{bmatrix}}_{C_{\mathrm{N}}} \begin{bmatrix} p_{\mathrm{c}} \\ \dot{p}_{\mathrm{c}} \\ Q_{\mathrm{c}} \end{bmatrix} + \underbrace{\begin{bmatrix} 0 & R_1 & L_{\mathrm{H}} \\ 0 & 1 & 0 \\ 0 & 0 & 0 \end{bmatrix}}_{D_{\mathrm{N}}} \begin{bmatrix} p_{\mathrm{o}} \\ Q_{\mathrm{i}} \\ \dot{Q}_{\mathrm{i}} \end{bmatrix}, \tag{2-37}$$

where A_{N}, B_{N}, C_{N}, and D_{N} denote the state-space system matrices and $\dot{x}_{\mathrm{N}}$, x_{N}, u_{N}, and y_{N} the state derivatives, states, inputs, and outputs, respectively.

Two-turbine hydraulic network model

When expanding towards the two-turbine farm, a model is needed to represent the hydraulic network that connects the two turbines to the spear valve. A model can be constructed assuming two parallel pipeline segments coming from the two turbines, which come together in one single segment leading to the spear valve, as shown in Figure 2-7. The assumption is made that the length and radius of all segments are equal, leading to equivalent L_{H} and C_{H} terms. Furthermore, it is assumed that the input flow of the combining pipe segment is the sum of the flows of the two parallel lines and that the pressure at each outlet of the parallel lines is equal to the inlet pressure p_{line} at the junction point. The derivation of the state-space model for the two-turbine hydraulic network is given in Appendix B.

2-3-1 Modeling hydraulic characteristics

Laminar and turbulent flows

Whether a flow of fluid is laminar or turbulent, is assessed by calculating the Reynold's number [75]

$$\mathrm{Re} = \frac{\rho_{\mathrm{w}} Q D_{\mathrm{L}}}{\mu A_{\mathrm{L}}}, \tag{2-38}$$

where D_{L} is the cross-sectional diameter. The flow is deemed laminar for Reynold numbers below 2300. In reality, there is a transition region between laminar and turbulent flows. However, in this work, it is assumed that the flow is turbulent for Reynold numbers above 2300.

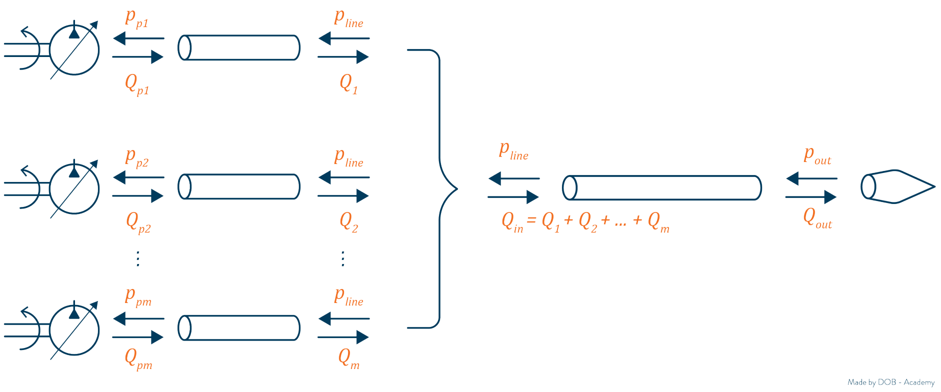

Figure 2-7: A schematic overview of a multi-turbine hydraulic network model. Each cylinder represents a pipe segment, as depicted in Figure 2-6. The m parallel pipelines originating from the wind turbines come together in a single pipe segment which leads to the spear valve. The inlet flow of the collective pipeline is the sum of the flows of its predecessors. It is assumed that the pressure p_{line} is equal for the parallel pipeline outlets.

Hydraulic induction

The hydraulic induction of fluid is analogous to the mass of a mass-spring-damper system and represents the resistance to an acceleration of the fluid. This may thus induce system delays. The hydraulic inductance of a pipeline is modeled as the fluid inertia in the control volume [17],

$$L_{\text{H}} = f_{\text{c}} \frac{\rho_{\text{w}} L_{\text{L}}}{A_{\text{L}}}, \tag{2-39}$$

$$f_{\text{c}} = \begin{cases} \frac{4}{3}, & \text{if } \text{Re} \leq 2300, \\ 1, & \text{otherwise}, \end{cases} \tag{2-40}$$

where f_{c} is the laminar flow correction factor. The fluid inertia describes the mass inertia effect of a fluid mass and is characterized by the fluid density, line length, and cross-sectional area of the pipeline, as can be seen in (2-39).

Hydraulic capacitance

Due to compressibility, a fluid in a pipeline behaves similar to a mechanical spring. The fluid in a pipeline segment is modeled as a constant volume with an effective bulk modulus E_{e}, associated with its compressibility. The spring stiffness C_0 represents the resistance to fluid volume changes and is defined as the ratio between the change in force dF exerted on the fluid in a rigid internal pipeline volume and the compression length of the fluid dL,

$$C_0 = \frac{dF}{dL}. \tag{2-41}$$

The addition or subtraction of a volume dV of water to the pipeline with constant volume $V_{\mathrm{L}} = A_{\mathrm{L}} L_{\mathrm{L}}$ will lead to a change in pressure

$$dp = E_{\mathrm{e}} \frac{dV}{V_{\mathrm{L}}}, \tag{2-42}$$

where E_{e} is the effective bulk modulus, which considers both the fluid stiffness and the material compliance [17]. The change of volume with respect to time is the effective flow Q, in or out of the system. Therefore, (2-42) can be written as

$$\dot{p} = E_{\mathrm{e}} \frac{Q}{V_{\mathrm{L}}}. \tag{2-43}$$

The inverse of the hydraulic spring stiffness C_0 is known as the hydraulic capacitance. This capacitance is the relation between the time rate of change of the pressure and the effective volumetric flow [17],

$$C_{\mathrm{H}} = \frac{1}{C_0} = \frac{Q}{\dot{p}} = \frac{V_{\mathrm{L}}}{E_{\mathrm{e}}}. \tag{2-44}$$

Hydraulic resistance

The hydraulic resistance in a pipeline is analogous to the damping in a mass-spring-damper system and is induced by fluid friction and flow losses. This term represents a resistance to velocity changes in the system. In general, there are two types of hydraulic resistance recognized: (1) resistance due to pressure losses induced by friction and fluid shear and (2) resistance due to flow losses in hydraulic components [17]. It is assumed that there are no leakages in the pipeline. Therefore, there is only a pressure loss resistance term which is induced by fluid and surface friction.

The hydraulic resistance R_{H} is the change in pressure over the flow rate and is defined by the Darcy-Weisbach equation [76].

$$R_{\mathrm{H}} = \frac{8\rho_{\mathrm{w}} L_{\mathrm{L}} Q}{\pi^2 D_{\mathrm{L}}^5} f, \tag{2-45}$$

where f is the friction coefficient. For laminar flows, this friction coefficient and hydraulic resistance are given by

$$f_{\mathrm{lam}} = \frac{64}{\mathrm{Re}}, \tag{2-46}$$

$$R_{\mathrm{H,lam}} = \frac{8\mu L_{\mathrm{L}}}{\pi R_{\mathrm{L}}^4}, \tag{2-47}$$

where R_{L} is the radius of the pipeline. For turbulent flows, the friction coefficient is evaluated using the Haaland equation [29], which approximates the Colebrook-White formula [76] for flows with Reynold numbers between $4000 \leq \text{Re} \leq 10^8$ [29].

$$f_{\text{turb}} = \left(-1.8 \log \left[\frac{6.9}{\text{Re}} + \left(\frac{\epsilon_{\text{L}}}{3.7 D_{\text{L}}}\right)^{1.11}\right]\right)^{-2}, \tag{2-48}$$

in which ϵ_{L} is the internal surface roughness of the pipeline. Substituting (2-48) in the Darcy-Weisbach formula (2-45) results in a formulation of the hydraulic resistance term for turbulent flows [9]

$$R_{\text{H}} = \frac{8\rho_{\text{w}} L_{\text{L}} Q}{\pi^2 D_{\text{p}}^5} \left(-1.8 \log \left[\frac{6.9}{\text{Re}} + \left(\frac{\epsilon_{\text{L}}}{3.7 D_{\text{L}}}\right)^{1.11}\right]\right)^{-2}. \tag{2-49}$$

2-3-2 The necessity of a linear parameter-varying model

To find out if an LPV model is needed to describe the nonlinear model or if a static model suffices, an analysis of a single-turbine and two-turbine case is performed and can be found in Appendix C. This analysis also covers the effects of the pipeline length and -radius design parameters on the hydraulic dynamics. For conciseness, this is not discussed in this section.

As mentioned in the previous section, the hydraulic resistance term is affected by the magnitude of the flows in the system. Accordingly, the dynamics of the LPV model change for a varying flow. Larger flows result in larger resistance, and thus there is more pressure loss in the pipeline. This increases the damping while the induction and capacitive terms remain unchanged. The added damping is seen as the damping of the resonance peaks in the bode response in Figure 2-8. Furthermore, an increased DC gain is visible in Figure 2-8b. This results in an increased pump flow to pump pressure relation, indicating higher friction and therefore larger network losses.

Simulations in Appendix C show that the hydraulic network has a cut-in flow. If the flow declines below this value, the system will exhibit unstable dynamical behavior. Therefore, for efficient control of HWFs it is important that the controller can maintain the pump flows above this cut-in flow value.

The dynamical behavior changes significantly for different flows. Therefore, a LPV hydraulic pipeline model is adopted to capture the nonlinear hydraulic dynamics.

2-4 Spear valve

The spear valve is used to convert the high-pressure pipeline flow at the nozzle side into a high-velocity water jet, which is then used to power the rotation of the Pelton turbine. Moreover, the spear valve controls the pressure traversing through the hydraulic system. By changing the position s of the spear valve, the area of the nozzle opening A_{nz} changes, leading to a pressure discharge, given by [43]

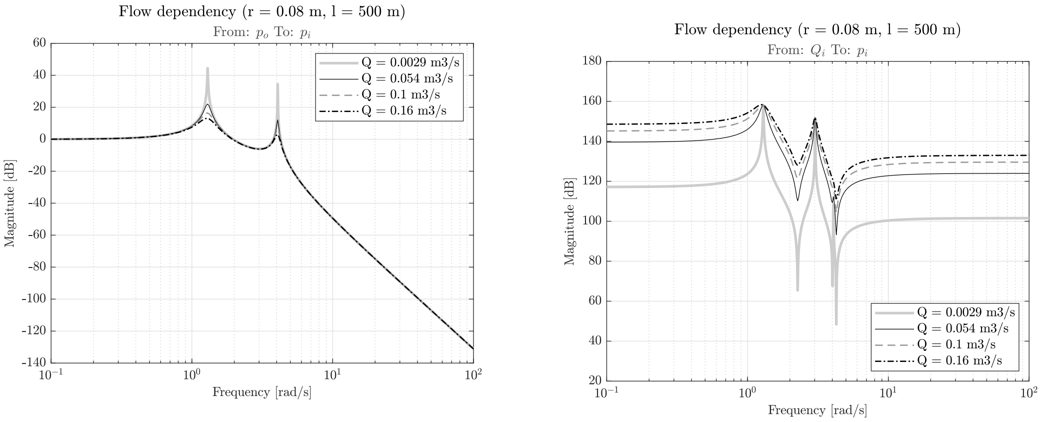

(a) Single-turbine (p_o to p_i)

(b) Single-turbine (Q_i to p_i)

Figure 2-8: Influence of different pipeline flows on the bode response of a two-turbine hydraulic network for the system inputs: outlet pressure p_o (left) and inlet flow Q_i (right), to the system output: inlet pressure p_i. The pipeline flow influences the damping and DC gain of the system. The natural frequencies remain unchanged.

$$\Delta p_\mathrm{nz}(s) = \frac{\rho_\mathrm{w}}{2}\left(\frac{Q_\mathrm{nz}}{C_\mathrm{d} A_\mathrm{nz}(s)}\right)^2, \tag{2-50}$$

where Q_nz the flow of water through the spear valve, which is taken to be the output flow of the hydraulic network Q_o, C_d is the discharge coefficient to account for pressure losses due to the geometry and flow regime at the nozzle exit, and A_nz the effective area of the nozzle orifice, controllable by altering the spear valve position as in [43]

$$A_\mathrm{nz}(s) = N_\mathrm{s}\pi\left(\frac{D_\mathrm{nz}^2}{4} - (s_\mathrm{max} - s)^2 \tan^2\frac{\alpha}{2}\right), \tag{2-51}$$

where D_nz denotes the nozzle diameter, which is derived such that nominal pressure can be realized in rated flow conditions, the spear coning angle is described by α, N_s indicates the amount of spear valves on the same line. Modeling multiple spear valves by N_s assumes equal effective nozzle areas for all valves. Furthermore, $\{s \subset \mathbb{R} \mid 0 \leq s \leq s_\mathrm{max}\}$ represents the position of the spear in the circular nozzle cross-section. The spear valve is closed at $s = 0$ m and fully open as the maximum spear position is reached [43],

$$s_\mathrm{max} = \frac{D_\mathrm{nz}}{2\tan\frac{\alpha}{2}}. \tag{2-52}$$

The dynamics of the spear position actuator are approximated by a first order actuator model,

$$\dot{s} = \frac{1}{t_\mathrm{s}} \left(s_\mathrm{ref} - s\right), \tag{2-53}$$

where t_s is the spear actuator time constant which described how fast the spear valve position responds to a reference value input s_ref, given by a controller.

Using the pressure obtained in (2-50), the spear valve converts a high-pressure water stream into a high-velocity jet. The velocity and power of the jet are described in the following equations [35]:

$$v_\mathrm{jet} = C_\mathrm{v} \frac{Q_\mathrm{nz}}{A_\mathrm{nz}}, \tag{2-54}$$

$$P_\mathrm{jet} = Q_\mathrm{nz} \Delta p_\mathrm{nz}, \tag{2-55}$$

where C_v is a vena-contracta coefficient to account for the change in velocity immediately after the water jet exits the nozzle.

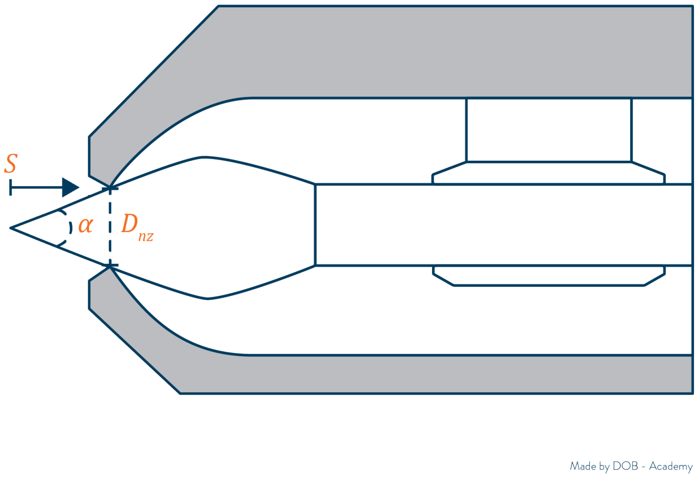

Figure 2-9: Cross-section of a spear valve. The spear coning angle is given by α, the nozzle diameter by D_nz, and the position of the spear tip in the nozzle by s. The spear valve is closed for $s = 0$ and fully opened for $s = s_\mathrm{max}$.

2-5 Pelton turbine

The Pelton turbine is used to convert the energy contained in the high-velocity water jet, that leaves the spear valve, into rotation of the Pelton runner and thereby delivering mechanical energy to a generator shaft. A schematic view of a Pelton turbine is given in Figure 2-10. The Pelton runner consists of a series of double spoon-shaped buckets spaced uniformly along a disk. The water jet is directed to the center of the buckets, tangent to the runner pitch circle diameter (PCD). A splitter inside the buckets redirects the flow such that it leaves the buckets in almost the opposite direction. The momentum of the water jet is transferred to the runner and its impulse exerts a torque on the Pelton turbine, which drives the rotation of the generator shaft [35]. In comparison with other hydro-turbines, the Pelton turbine is particularly eligible for high-pressure applications with power ratings up to 500 MW [19]. The Pelton turbine is a decoupled system and thus does not influence the components upstream of the hydraulic drivetrain.

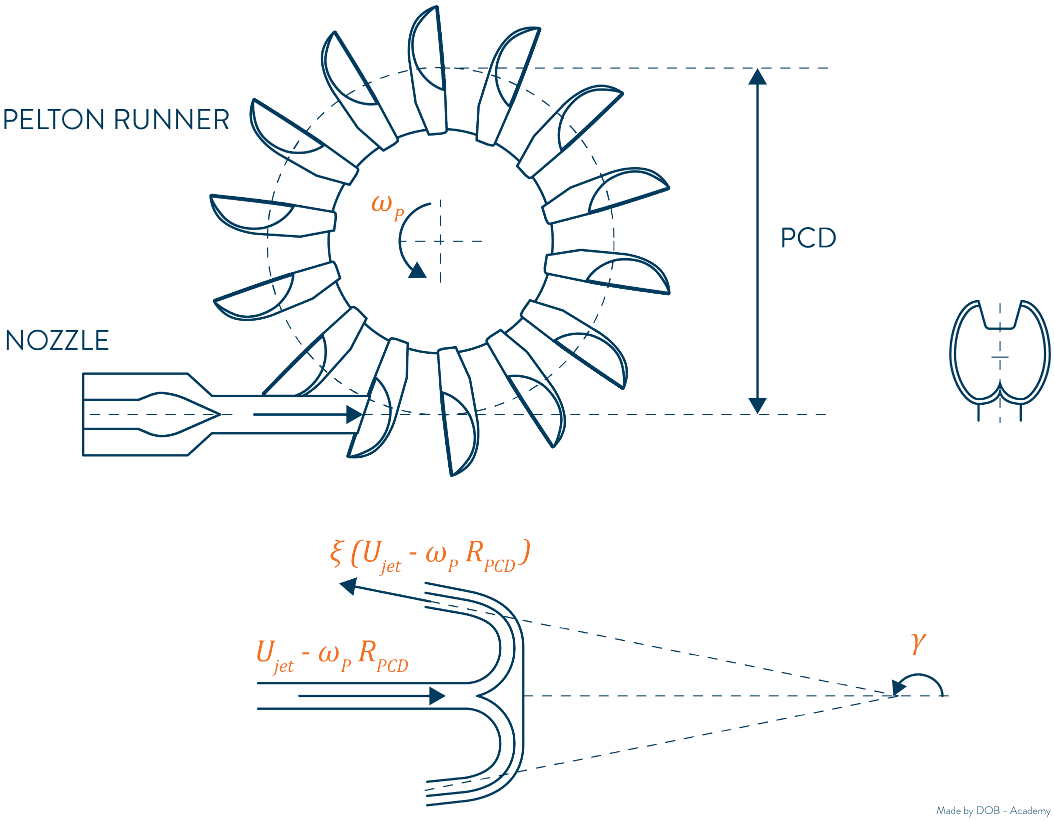

Figure 2-10: Schematic view of a Pelton turbine (top), and a simplified view of the flow in a Pelton bucket (bottom). The high-velocity jet exerts a torque on the Pelton buckets, inducing rotation. The Pelton turbine is mechanically coupled to a generator.

The hydraulic efficiency of the Pelton runner is calculated using the momentum law [80]

$$\eta_{\mathrm{pt}} = 2k_{\mathrm{u}}\left(1 - k_{\mathrm{u}}\right)\left(1 - \xi\cos\theta\right) \tag{2-56}$$

where the efficiency factor to account for the friction of the flow in the bucket is denoted by ξ, the angle between the circumferential and relative velocities of the flow is defined as θ, and k_{u} is the runner speed ratio, represented by the ratio v_{pt} between the tangential runner speed at the PCD and the water jet velocity v_{jet}

$$k_{\mathrm{u}} = \frac{v_{\mathrm{pt}}}{v_{\mathrm{jet}}} = \frac{\omega_{\mathrm{pt}} R_{\mathrm{PCD}}}{v_{\mathrm{jet}}}. \tag{2-57}$$

The theoretical maximum efficiency is obtained by solving $\delta\eta_{\mathrm{pt}}/\delta k_{\mathrm{u}} = 0$, which gives the optimal relation between the jet velocity and the angular velocity of the Pelton turbine, resulting into [35]

$$k_{\mathrm{u}}^{*} = \frac{1}{2}. \tag{2-58}$$

Substituting (2-58) in (2-57), gives

$$\omega_{\mathrm{pt}}^{*} = \frac{v_{\mathrm{jet}}}{2R_{\mathrm{PCD}}}. \tag{2-59}$$

The optimal Pelton rotation speed ω_{pt}^{*} can be used as a reference signal in generator torque control to maintain the optimal Pelton efficiency. The torque generated by the Pelton runner is described by

$$\tau_{\mathrm{pt}} = \frac{\eta_{\mathrm{pt}} P_{\mathrm{jet}}}{\omega_{\mathrm{pt}}}, \tag{2-60}$$

where ω_{pt} is the Pelton angular velocity. The Pelton turbine drives a generator shaft. The power produced by the generator is given by

$$P_{\mathrm{g}} = \omega_{\mathrm{pt}} \tau_{\mathrm{g}} \eta_{\mathrm{g}}, \tag{2-61}$$

where η_{g} is assumed to be a constant generator efficiency. The Pelton generator dynamics can be described by the Newton law of rotation

$$J_{\mathrm{pt}} \dot{\omega}_{\mathrm{pt}} = \tau_{\mathrm{pt}} - \tau_{\mathrm{g}}, \tag{2-62}$$

where J_{pt} is the combined inertia of the Pelton turbine and generator, τ_{g} is the generator torque. The generator torque can be controlled to regulate the angular velocity of the Pelton turbine for maintaining the optimal k_{u}^{*} value.

2-5-1 Fixed-speed Pelton turbine

In this work, a fixed-speed Pelton turbine is employed to drive a synchronous generator. The dynamics equation in (2-62) can be omitted and the performance of the Pelton runner and electrical conversion is now only given by equations (2-56), (2-57), and (2-61), resulting into,

$$P_{\mathrm{g}} = P_{\mathrm{jet}} \eta_{\mathrm{pt}} \eta_{\mathrm{g}}. \tag{2-63}$$

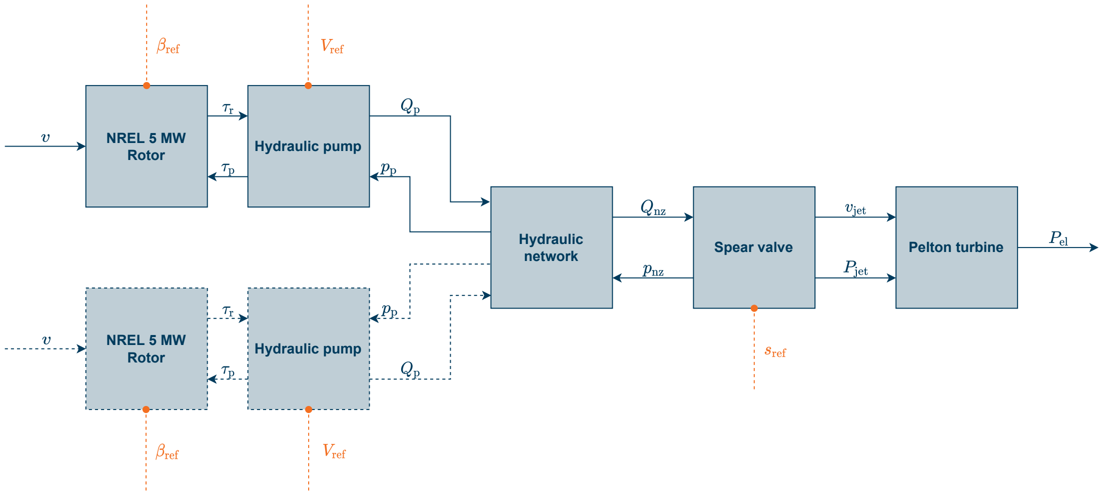

Figure 2-11: Block diagram of the implemented plant model. The diagram shows all the components of the system and their key inputs and outputs, which were introduced in the previous sections. The blocks with dashed black borders are only present in the two-turbine case. Furthermore, the control inputs are denoted as the red dashed lines.

2-6 System model implementation

This section gives an overview of the plant model that is implemented in this thesis.

By collecting the equations that describe the dynamics of the rotor speed (2-7), blade pitch actuator (2-4), pump displacement actuator (2-24), hydraulic network (2-36)-(2-37), and spear valve actuator (2-53), a model could be created.

The block diagram in Figure 2-11 shows a schematic overview of the implemented plant model, visualizing its components and key inputs and outputs. The system is modeled and implemented in MATLAB-Simulink using the `Control System Toolbox`.

2-6-1 Discretization

The system model is discretized to be used efficiently with a discrete-time model predictive control (MPC) controller within Simulink. To discretize the dynamics of all components, excluding the hydraulic network, given by equations (2-7) (2-4), (2-24), and (2-53), these equations are simply applied at all of the time steps k. The mapping between the discrete and continuous-time indications k and t is given by $t = t_0 + k\Delta t_{\text{s}}$, where $\Delta t_{\text{s}} = 0.01$ is the sampling time in seconds. An exception is formed by the discretization of the LPV hydraulic network dynamics. These dynamics are discretized employing the Runge-Kutta method as used in [13]. The choice for this method comes from the fact that a `Discrete Varying state-space` block is used. The method can be used to discretize the varying A, B, C, and D matrices during a Simulink simulation.

Chapter 3

Convex Economic MPC framework: Theoretical Overview

The computational tractability of nonlinear optimization problems is restricted by their nonlinear nature [41] and becomes critical for real-time implementation of large multivariable systems. The computational complexity is an important factor to take into account as the control framework developed in this thesis is intended to be scalable for the number of wind turbines. Furthermore, nonlinear optimization algorithms do generally not guarantee globally optima. This chapter describes a modified version of an existing convex economic model predictive control (CEMPC) framework [31]. The modification allows the framework to be used on hydraulic-drivetrain wind farms (HWFs) containing one, or multiple hydraulic-drivetrain wind turbines (HWTs). The controller exploits measurements, states, and outputs of all the wind turbines in the farm to find a global optimal solution to a farm-wide power maximization objective. Moreover, the CEMPC approach arguably offers better perspectives for limiting computational demand, thereby forming a promising opportunity to realize real-time implementation.

Since the Pelton turbine system does not affect the other subsystems, it can be considered as a system on its own and can therefore be excluded from the power maximizing objective [45]. Therefore, the HWF power maximizing objective refers to maximizing the power contained in the high-velocity water jet, leaving the shared drivetrain through the spear valve.

Section 3-1 describes a nonlinear internal control model of the system that can be modified for use in the CEMPC framework. Furthermore, it is explained that using this model leads to a nonlinear optimization problem. Section 3-2 elaborates on the transformation of the nonlinear optimization problem into a convex problem utilizing a change of variables.

3-1 Nonlinear internal control model

The internal control model is a simplified representation from the HWF model derived in Chapter 2. The rotor dynamics are considered as the only dynamics in the control model, hence, the hydraulic network and actuator dynamics are neglected.

For clarity, relevant equations which appeared in the previous chapter are repeated. The rotor dynamics are given by

$$J\dot{\omega} = \tau_{\mathrm{r}} - \tau_{\mathrm{p}}, \tag{3-1}$$

where $\dot{\omega}$ is the rotational acceleration of the rotor, J is the total rotational inertia of the drivetrain, τ_{r} is the rotor torque and τ_{p} is the pump torque. The total aerodynamic rotor power that is extracted by the rotor is given by

$$P_{\mathrm{r}} = \frac{1}{2}\rho_{\mathrm{a}} A C_{\mathrm{P}}(\beta, \lambda) v^3, \tag{3-2}$$

in which ρ_{a} is the air density, $A = \pi R^2$ is the rotor area with a rotor radius of R, C_{P} is the power coefficient as a function of λ and β being the tip-speed ratio (TSR) and collective blade pitch angles, respectively. The TSR is given by $\lambda = \omega R/v$, with ω the rotor speed and v the effective wind speed. The collective blade pitch angle is given by $\{\beta \subset \mathbb{R} \mid \beta_{\min} \leq \beta \leq \beta_{\max}\}$, with constant minimum and maximum actuator saturation values $\beta_{\min}$ and $\beta_{\max}$.

The rotor and pump torque are given by

$$\tau_{\mathrm{r}} = \frac{1}{2}\rho_{\mathrm{a}} A \frac{C_{\mathrm{P}}(\beta, \lambda) v^3}{\omega}, \tag{3-3}$$

$$\tau_{\mathrm{p}} = \frac{V_{\mathrm{p}} \Delta p_{\mathrm{p}}}{\eta_{\mathrm{m}}}, \tag{3-4}$$

where V_{p} is the volumetric pump displacement, Δp_{p} is the pressure over the pump, and η_{m} is the mechanical efficiency of the pump.

Since the hydraulic network dynamics are omitted in the control model, the pressure in the system is derived by,

$$\Delta p_{\mathrm{p}}(s) = \Delta p_{\mathrm{nz}}(s) = \frac{\rho_{\mathrm{w}}}{2}\left(\frac{Q_{\mathrm{nz}}}{C_{\mathrm{d}} A_{\mathrm{nz}}(s)}\right)^2, \tag{3-5}$$

where ρ_{w} is the density of seawater, C_{d} is the discharge coefficient, Q_{nz} is the flow passing the nozzle, and $A_{\mathrm{nz}}(s)$ is the aperture area of the spear valve, which is controlled by the spear valve position $\{s \subset \mathbb{R} \mid 0 \leq s \leq s_{\max}\}$, where $s_{\max}$ is the value for which the spear valve is fully open. Note that in the internal control model, pressures at the pumps Δp_{p} equal the nozzle pressure Δp_{nz}. The effective nozzle area is given by

$$A_{\mathrm{nz}}(s) = N_{\mathrm{s}}\pi\left(D_{\mathrm{nz}}^2/4 - (s_{\max} - s)^2 \tan^2(\alpha/2)\right), \tag{3-6}$$

where D_{nz} denotes the nozzle diameter, the spear coning angle is described by α, and N_{s} indicates the number of spear valves on one line.

As the hydraulic network dynamics are omitted in the control model, a static relation of the nozzle flow resulting from the pump flows generated in the HWF is given as

$$Q_{\mathrm{nz}} = \sum_{n=1}^{N} Q_{\mathrm{p},n} = \sum_{n=1}^{N} V_{\mathrm{p},n}\omega_n\eta_{\mathrm{v}}, \tag{3-7}$$

where η_{v} is the volumetric pump efficiency, and $Q_{\mathrm{p},n}$ and $V_{\mathrm{p},n}$ are, respectively, the produced pump flow and pump displacement of turbine $\{n \subset \mathbb{Z}^+ \mid 1 \leq n \leq N\}$, where N denotes the total number of turbines in the system. The volumetric- and mechanical power of the pump are given by

$$P_{\mathrm{p}}^{(v)} = Q_{\mathrm{p}}\Delta p_{\mathrm{p}} = V_{\mathrm{p}}\omega\Delta p_{\mathrm{p}}\eta_{\mathrm{v}}, \tag{3-8}$$

$$P_{\mathrm{p}}^{(m)} = \tau_{\mathrm{p}}\omega = V_{\mathrm{p}}\omega\Delta p_{\mathrm{p}}, \tag{3-9}$$

where P_{p} is used to denote the volumetric power $P_{\mathrm{p}}^{(v)}$ for the remainder of this work, the mechanical pump is always denoted with a superscript.

Finally, the power leaving the spear valve is calculated by summing up the power of all the hydraulic pumps in the plant,

$$P_{\mathrm{jet}} = \sum_{n=1}^{N} P_{\mathrm{p},n}. \tag{3-10}$$

By using the discussed equations, the dynamics of the N-turbine HWF can be written as the following nonlinear state-space form and nonlinear state:

$$\begin{cases} \dot{\omega}_n = \Phi_n(\beta_n, v_n, \omega_n) - \Theta_n V_{\mathrm{p},n}\left(\sum_{n=1}^{N} V_{\mathrm{p},n}\omega_n\eta_{\mathrm{v}}\right)^2 A_{\mathrm{nz}}^{-2}(s), \qquad \forall\, n \subset \mathbb{Z}^+, & (3\text{-}11) \\ P_{\mathrm{jet}} = \dfrac{\rho_{\mathrm{w}}}{2}\left(\sum_{n=1}^{N} V_{\mathrm{p},n}\omega_n\eta_{\mathrm{v}}\right)^3 \left(C_{\mathrm{d}}A_{\mathrm{nz}}(s)\right)^{-2}, & (3\text{-}12) \end{cases}$$

in which $\Phi_n(\beta_n, v_n, \omega_n) = J^{-1}\tau_{\mathrm{r},n}(\beta_n, v_n, \omega_n)$ and $\Theta_n = \rho_{\mathrm{w}}\left(2\eta_{\mathrm{m}}C_{\mathrm{d}}^2 J\right)^{-1}$. Equation (3-11) represents the rotor dynamics for every turbine n in the HWF. The states of the combined system are the rotor speeds of the turbines ω_n, the inputs are the blade pitch angles β_n, pump displacements $V_{\mathrm{p},n}$, and spear valve position s, the disturbances are the effective wind speeds v_n, and the output is the jet power P_{jet}. Note that as actuator dynamics are not considered in the internal model, the blade pitch angles, volumetric pump displacements, and spear position are instantaneous inputs. Furthermore, the pump efficiencies are assumed constant for the remainder of this chapter; their variability will be discussed in Section 4-2.

3-1-1 Nonlinear optimization problem

To show the nonlinear nature of the optimization problem that arises when employing the simplified wind farm model, the objective of jet power maximization is considered. The optimization problem is structured as

$$\max_{s(t),\beta_1(t),\ldots,\beta_N(t),V_{\mathrm{p},1}(t),\ldots,V_{\mathrm{p},N}(t)} \int_{t_0}^{t_1} P_{\mathrm{jet}}(t)dt \tag{3-13}$$

subjected to:

Dynamical system in Eq.(3-11) and Eq. (3-12),

$$\omega_{\mathrm{min}} \leq \omega_n(t) \leq \omega_{\mathrm{max}}, \qquad n \in \{1,2,\ldots,N\}, \tag{3-14}$$

$$\beta_{\mathrm{min}} \leq \beta_n(t) \leq \beta_{\mathrm{max}}, \qquad n \in \{1,2,\ldots,N\}, \tag{3-15}$$

$$0 \leq V_{\mathrm{p},n}(t) \leq V_{\mathrm{max}}, \qquad n \in \{1,2,\ldots,N\}, \tag{3-16}$$

$$P_{\mathrm{min}} \leq P_{\mathrm{p},n}(t) \leq P_{\mathrm{rated}}, \qquad n \in \{1,2,\ldots,N\}, \tag{3-17}$$

$$s_{\mathrm{min}} \leq s(t) \leq s_{\mathrm{max}}, \tag{3-18}$$

where the dependence on time t is explicitly shown in order to emphasize that the optimization occurs over a prediction horizon starting at t_0 and ending in the predicted future at time t_1. Note that the P_{min} and P_{rated} values regarding the model predictive control (MPC) optimization methods in this thesis denote the volumetric minimum and rated powers.

Within the framework described above, the objective function (3-13) as well as the inequality constraints given by (3-14)-(3-18), take a linear form. However, the equality constraints imposed by the system dynamics in (3-11) and (3-12) are undeniably nonlinear, which makes this a nonlinear optimization problem.

3-2 Convex economic model predictive control framework

This section is devoted to the derivation of a novel CEMPC framework for HWFs. The framework for HWTs is inspired by the pioneering work of Hovgaard, Boyd, and Jørgensen, presented in [31]. Multiple papers in state-of-the-art literature present extensions of the original framework for conventional wind turbines [18, 58–61], but to the best of the author's knowledge, there has not been an extension such it can be used for HWFs. Moreover, the existing CEMPC frameworks are created for the control of single turbines, where the framework created in this thesis is capable of calculating control signals for multiple HWTs in a farm. These control inputs are optimized to maximize the overall power production of the HWF. For this reason, the derivation of this CEMPC framework for HWFs is regarded as a novel contribution. A schematic overview of this framework is graphically presented in Figure 3-1.

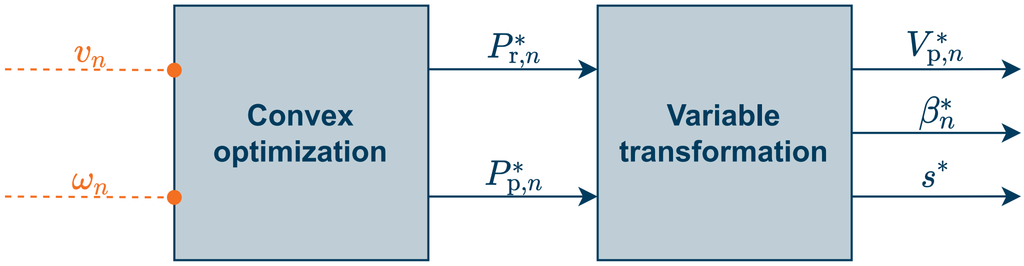

Figure 3-1: Block diagram of the convex economic model predictive framework. The framework uses the rotor speed inputs ω_n of all turbines n to calculate the rotor kinetic energy values at the initial time t_0 of an MPC cycle. The optimizer uses the rotor speed and rotor-effective wind speed inputs v_n in the convex system expression to optimize the rotor and pump power trajectories $P_{\mathrm{r},n}$ and $P_{\mathrm{p},n}$ over a prediction horizon of $[t_0, t_1]$. The optimization problem is restricted by state and input constraints. The results of the first time step are taken and transformed in the original system variables: pump displacements $V_{\mathrm{p},n}$, spear valve position s, and the collective blade pitch angles β_n.

A convex representation of the internal control model system is derived by rewriting the nonlinear optimization problem in terms of energies, powers, and pressure. The system representation is rewritten as a convex optimization problem of the form [15]

$$\min_x f(x) \tag{3-19}$$

$$\text{s.t.}\;\; g_i(x) \le 0, \quad \forall i, \tag{3-20}$$

$$h_k(x) = 0, \quad \forall k, \tag{3-21}$$

where x represents the optimization variables. The inequality constraints g_i and objective function f are convex, and all equality constraints h_k are affine. The essential change of variables in this work is described by

$$\left.\begin{aligned} x &= \omega \\ \mathbf{u} &= [V_\mathrm{p}\ \beta\ s]^\top \\ d &= v \end{aligned}\right\} \rightarrow \left\{\begin{aligned} x &= K \\ \mathbf{u} &= [P_\mathrm{r}\ P_\mathrm{p}]^\top \\ d &= v \end{aligned}\right. , \tag{3-22}$$

where the original variables are depicted on the left-hand side, and the new variables on the right-hand side, x denotes the system's state, $\mathbf{u}$ represents the system's input vector, d represents the system's disturbance, and K is the rotational kinetic energy of the drivetrain. Note that (3-22) describes the variable changes for a single turbine system. Extending this principle for a N-turbine wind farm, gives the following variable transformations:

$$\left.\begin{aligned}\mathbf{x} &= [\omega_1 \; \dots \; \omega_N]^\top \\ \mathbf{u} &= [V_{\mathrm{p},1} \; \dots V_{\mathrm{p},N} \; \beta_1 \; \dots \; \beta_N \; s]^\top \\ \mathbf{d} &= [v_1 \; \dots \; v_N]^\top\end{aligned}\right\} \rightarrow \left\{\begin{aligned}\mathbf{x} &= [K_1 \; \dots \; K_N]^\top \\ \mathbf{u} &= [P_{\mathrm{r},1} \; \dots \; P_{\mathrm{r},N} \; P_{\mathrm{p},1} \; \dots \; P_{\mathrm{p},N}]^\top \; . \\ \mathbf{d} &= [v_1 \; \dots \; v_N]^\top\end{aligned}\right. \tag{3-23}$$

3-2-1 Transforming the system dynamics

To obtain a convex representation of the system, such that a convex optimization problem as in (3-19) can be constructed, the variable change described in the previous subsection is performed. Note that linear rotor kinetic energy dynamics are imperative, as described by (3-21). First, consider the relationship between the rotational kinetic energy and rotor speed,

$$K = \frac{1}{2} J \omega^2. \tag{3-24}$$

The dynamics of the convex system representation are found by taking the derivative of (3-24) with respect to time and substituting (3-1) in the result.

$$\dot{K} = P_\mathrm{r} - \frac{P_\mathrm{p}}{\eta_\mathrm{v} \eta_\mathrm{m}}, \tag{3-25}$$

note that $P_\mathrm{p}/\eta_\mathrm{v} = P_\mathrm{p}^{(m)}$, which is the mechanical pump power.

The state-space representation of a N-turbine convex control model HWF system is described by

$$\begin{cases} \dot{K}_n = P_{\mathrm{r},n} - \dfrac{P_{\mathrm{p},n}}{\eta_\mathrm{v} \eta_\mathrm{m}}, \qquad \forall n \subset \mathbb{Z}^+, & (3\text{-}26) \\ P_\mathrm{jet} = \displaystyle\sum_{n=1}^{N} P_{\mathrm{p,n}}, & (3\text{-}10) \end{cases}$$

where the states are the rotational kinetic energies K_n, the inputs are the aerodynamic powers $P_{\mathrm{r},n}$ and volumetric pump powers $P_{\mathrm{p},n}$, note that there are no disturbances in this system representation, and the output is the jet power P_jet. The equation in (3-26) represents the rotational kinetic energy dynamics for every turbine n in the HWF. Finally, note that the system is linear and thus convex.

3-2-2 Transforming the inequality constraints

Having transformed the wind farm dynamics and output in (3-26) and (3-10), the remainder of the constraints posed by (3-14) - (3-18) will be transformed into a convex representation in this section.

First, the rotor kinetic energy dynamics in (3-26) are constrained by

$$K_{\mathrm{min}} \leq K_n \leq K_{\mathrm{max}}, \tag{3-27}$$

where $K_{\mathrm{min}} = J\omega_{\mathrm{min}}^2/2$ and $K_{\mathrm{max}} = J\omega_{\mathrm{max}}^2/2$.

The existing constraints on the pump powers $P_{\mathrm{p},n}$ is the same as in (3-17)

$$P_{\mathrm{min}} \leq P_{\mathrm{p},n} \leq P_{\mathrm{rated}}. \tag{3-28}$$

An additional constraint is needed to consider the bounds on the power posed by the pump displacements $V_{\mathrm{p},n}$, given by (3-16). The constraint is derived by substituting (3-24) in (3-8), which yields

$$0 \leq V_{\mathrm{max}} \sqrt{\frac{2K_n}{J}} \eta_{\mathrm{v}} \Delta p_{\mathrm{p}}, \tag{3-29}$$

where the rotor speed is substituted by $\omega_n = \sqrt{2K_n J^{-1}}$. Note that this constraint is nonlinear due to the multiplication of variables K_n and Δp_{p}. This poses a problem when trying to create a convex optimization problem. As explained in Section 1-3, one of the control objectives should be to maintain a constant network pressure, therefore, it is assumed that the variable Δp_{p} becomes a constant $\Delta\Delta\overline{p}_{\mathrm{p}}$, which remains constant along the MPC prediction horizon. From this point on forward, the constant pump pressure in the MPC representation will be denoted by $\Delta\overline{p}$. The new constraint becomes

$$0 \leq P_{\mathrm{p},n} \leq V_{\mathrm{max}} \sqrt{\frac{2K_n}{J}} \eta_{\mathrm{v}} \Delta\overline{p}. \tag{3-30}$$

The nozzle parameters are designed such that the system can operate at rated and maximum conditions. Therefore, the satisfaction of the constraints in (3-27) and (3-30) are enough to ensure the compliance to the constraint posed on the spear position s, given by (3-18).

The final constraint is needed to restrict the rotor power input. The rotor power P_{r} is limited by the maximum available power that could be captured by the wind turbine, given by

$$0 \leq P_{\mathrm{r},n} \leq \hat{P}_{\mathrm{av},n}(v_n, K_n), \tag{3-31}$$

where $\hat{P}_{\mathrm{av}}(v, K)$ represents a convex approximation of the available aerodynamic power P_{av} at a certain wind speed and kinetic energy. Note that the left-hand side is set to zero since the aerodynamic power can not be negative. The approximation method is discussed in the next section. The available power is defined by

$$P_{\mathrm{av}}(v, K) = \max_{\beta_{\min} \leq \beta \leq \beta_{\max}} \frac{1}{2} \rho A C_{\mathrm{P}}(\beta, \lambda) v^3. \tag{3-32}$$

As can be seen from the equation above, the last remaining original inequality constraint on β, given by (3-15), is used to define the upper bound on the aerodynamic power P_{r}.

By inspection of the constraints described in this section, it can be concluded that the inequalities in (3-27) and (3-30) are respectively linear and convex, and therefore satisfy the demands of the convex optimization form posed in (3-20). Similarly, (3-26) corresponds to the demanded affine form, as in (3-21). Moreover, the output equality constraint, posed in (3-10), is affine and thus conform with (3-19). At this point, the only constraints from which it is still uncertain if they comply with the convex optimization problem are the constraints on the rotor powers, denoted by (3-31). The approximated available powers $\hat{P}_{\mathrm{av},n}$ should be concave for the constraints to fall in line with the convex optimization problem.

3-2-3 Approximating the available power

This section is devoted to describing the method which is used to approximate the available rotor power as a concave function. The shape of the wind speed normalized true available power curves, denoted as the dotted lines in Figure 3-3, appear to be approximable by a concave function.

For every specific wind speed v_i, a piecewise linear approximation is created [32]:

$$\hat{P}_{\mathrm{av}}(v_i, K) = \min \left\{ a_1 K + b_1, \ldots, a_{n_{\mathrm{p}}} K + b_{n_{\mathrm{p}}} \right\} v_{\mathrm{i}}^3, \tag{3-33}$$

where the constants a and b form part of affine functions that each provide a local approximation of the available power curve, n_{p} is the total number of such affine functions. The following method is used to approximate $\hat{P}_{\mathrm{av}}(v_i, K)$.

First, the values of $\{K_i \subset K \mid K_{\min} \leq K \leq K_{\max}\}$ are collected for which a value is available in the power coefficient table $C_{\mathrm{P}}(\beta^*, \lambda)$. Note that, since the maximum available power occurs when operating at optimum pitch blade angle, β^* is assumed. The abovementioned rotor kinetic energy values can be found using

$$K_i = \frac{1}{2} J \left(\frac{\lambda v}{R} \right)^2, \tag{3-34}$$

where $\{\lambda \subset \mathbb{R}^+ \mid \lambda_{\min} \leq \lambda \leq \lambda_{\max}\}$, defined by the original C_{P} table seen in Figure 2-3. These values of K_i are used to derive the range of available power coefficient values $C_{\mathrm{P},i}(K_i)$, using a spline interpolation of the values of $C_{\mathrm{P}}(\beta^*, \lambda)$ over the values of K_i.

These values are used to find the available power equation as a function of the rotor kinetic energy.

$$P_{\mathrm{av}}(v_i, K_i) = \frac{1}{2}\rho_{\mathrm{a}} A C_{\mathrm{P},i}(K_i) v_i^3. \tag{3-35}$$

Next, the optimum of $P^*_{\mathrm{av}}(v_i, K^*_i)$ is found. The corresponding optimum kinetic rotor energy K^*_i is multiplied with a hard-coded partition vector, such that an n_{p} number of points of $\{K_{\mathrm{p}} \subset K_i \mid 0.5K^*_i \leq K_{\mathrm{p}} \leq 1.5K^*_i\}$ are selected around the optimum value K^*_i. The slope and bias of the true available power curve at these points are evaluated and stored in $\mathcal{A}_i$ and $\mathcal{B}_i$, respectively, given by

$$\mathcal{A}_i = [a_1, a_2, \ldots, a_{n_{\mathrm{p}}}], \tag{3-36}$$

$$\mathcal{B}_i = [b_1, b_2, \ldots, b_{n_{\mathrm{p}}}\ ] = P_{\mathrm{av}}(v_i, K_{\mathrm{p}}) - \mathcal{A}_i K_{\mathrm{p}}, \tag{3-37}$$

where the constants a and b denote the slopes and biases, respectively, measured at the evaluated partition points. Equation (3-33) can then be written as

$$\hat{P}_{\mathrm{av}}(v_i, K) = \mathcal{A}_i K + \mathcal{B}_i. \tag{3-38}$$

The method is graphically shown in Figure 3-2. The locations of the partitions $P_{\mathrm{av}}(v_i, K_{\mathrm{p}})$ on the curve and their corresponding linear functions are shown in Figure 3-2a. The minimum of these linear lines at each instant K can be used as an upper bound on the rotor power $P_{\mathrm{r}}(v_i)$. The resulting approximated curve is compared to the original curve in Figure 3-2b.

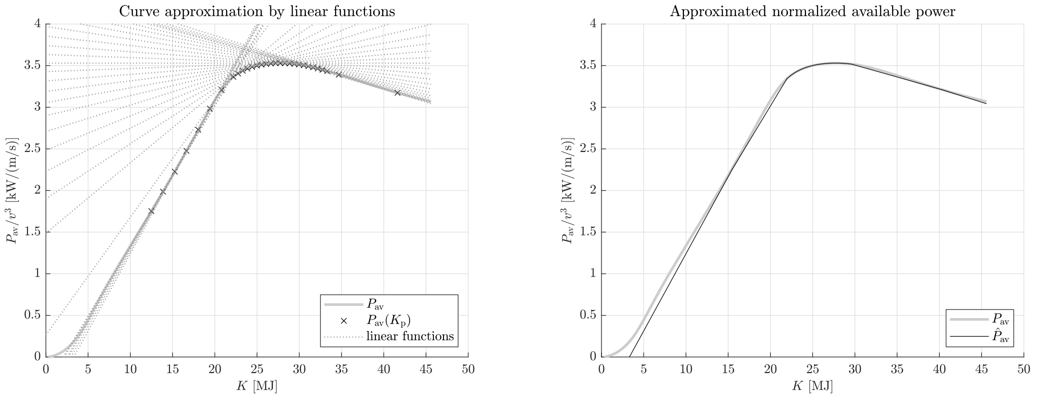

(a) Curve approximation by linear functions derived from the slope and bias of $P_{\mathrm{av}}(v_i, K_{\mathrm{p}})$.

(b) The true and approximated available power curve, P_{av} and $\hat{P}_{\mathrm{av}}$, respectively.

Figure 3-2: The available power approximation method for $v = 12$ m/s, normalized by v^3. (a) First, the optimum of the true available power curve P_{av} is found. The optimum value K^* is multiplied by a hard-coded partition vector to obtain n_{p} number of values of the curve around the optimum. The slope and bias are evaluated at these partition points, which are used to construct linear functions of which their combined minimum represents a linear approximation of the shape of the curve, as seen in (b). The approximated curve $\hat{P}_{\mathrm{av}}(v_i, K)$ can be used as the upper bound of the rotor power constraint in (3-31).

The approximated available powers for different wind speeds are presented in Figure 3-3. The corresponding original curves are shown as the dotted lines.

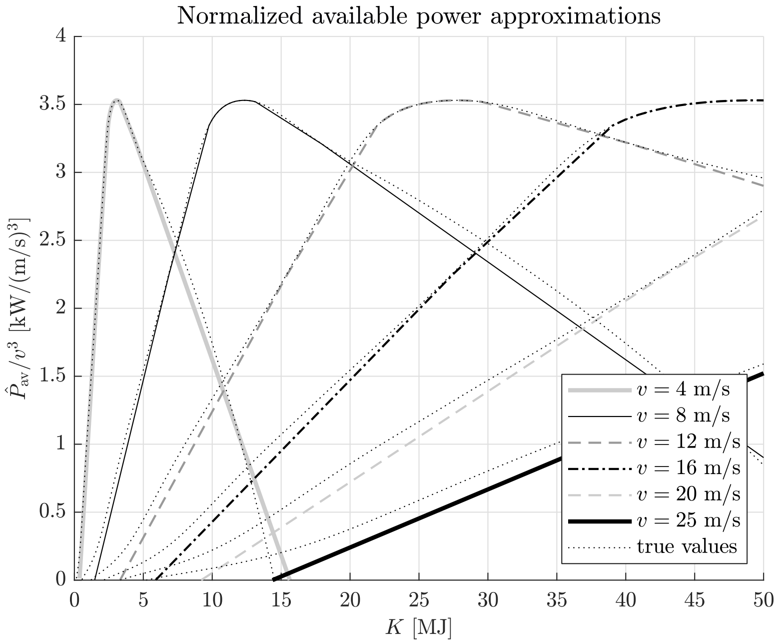

Figure 3-3: The linear approximated available power $\hat{P}_{\mathrm{av}}$, normalized by v^3, as a function of the rotational kinetic energy K for different wind speeds v. The true available power curves are also depicted as the dotted lines.

By using a linear interpolation between two neighboring wind speeds v_1 and v_2 for which a function of the form shown by (3-38) is available, a concave approximation of the available wind power can be constructed:

$$\hat{P}_{\mathrm{av}}(v, K) = \left(1 - \frac{v - v_1}{v_2 - v_1}\right) \hat{P}_{\mathrm{av},1}(K) + \left(\frac{v - v_1}{v_2 - v_1}\right) \hat{P}_{\mathrm{av},2}(K). \tag{3-39}$$

The resulting expression for $\hat{P}_{\mathrm{av}}(v, K)$ is concave because the sum of multiple concave functions remains concave.

3-2-4 Convex optimization problem

Using the convex control model dynamics constraints, with the new variables in terms of powers and energies, the originally nonlinear optimization problem discussed in Section 3-1-1 becomes convex and is given by

$$\max_{P_{\mathrm{r},1}(t),\ldots,P_{\mathrm{r},N}(t),P_{\mathrm{p},1}(t),\ldots,P_{\mathrm{p},N}(t)} \quad \int_{t_0}^{t_1} \sum_{n=1}^{N} P_{\mathrm{p},n}(t)dt \tag{3-40}$$

subjected to:

$$\dot{K}_n(t) = P_{\mathrm{r},n}(t) - \frac{P_{\mathrm{p},n}(t)}{\eta_\mathrm{v}\eta_\mathrm{m}}, \qquad n \in \{1,2,\ldots,N\}, \tag{3-26}$$

$$K_{\min} \leq K_n(t) \leq K_{\max}, \qquad n \in \{1,2,\ldots,N\}, \tag{3-27}$$

$$P_{\min} \leq P_{\mathrm{p},n}(t) \leq P_{\mathrm{rated}}, \qquad n \in \{1,2,\ldots,N\}, \tag{3-28}$$

$$P_{\mathrm{p,n}}(t) \geq 0, \qquad n \in \{1,2,\ldots,N\}, \tag{3-30}$$

$$P_{\mathrm{p,n}}(t) \leq V_{\max}\sqrt{\frac{2K_n(t)}{J}}\eta_\mathrm{v}\Delta\bar{p}, \qquad n \in \{1,2,\ldots,N\}, \tag{3-30}$$

$$0 \leq P_{\mathrm{r},n}(t) \leq \hat{P}_{\mathrm{av}}(v_n(t), K_n(t)), \qquad n \in \{1,2,\ldots,N\}, \tag{3-31}$$

where the dependence of the different variables on time t has again been included to highlight that the optimization occurs over the prediction horizon from t_0 to t_1. The presented optimization problem is convex as it satisfies the requirements discussed in (3-19)-(3-21): the objective of the maximization problem is of an affine form, and hence concave, the equality constraints and inequality constraints are linear, except for (3-30) and (3-31), which are concave.

3-2-5 Retrieving the original input variables

The computed solutions of the convex optimization problem, introduced above, can not directly be used to control the wind turbines. The optimized pump power P_p^* and P_r^* need to be transformed to the original input variables: pump displacements $V_{\mathrm{p},n}$, collective blade pitch angles β_n, and the spear valve position s.

First, the rotor speed of a turbine n can be retrieved using a modification of the kinetic rotor energy equation (3-24). Since K is constrained following the original constraint on the rotor speed (3-14), there is a one-to-one correspondence between K_n and ω_n, denoted as

$$\omega_n = \sqrt{\frac{2K_n}{J}}. \tag{3-41}$$

The optimal pump displacements $V_{\mathrm{p},n}$ are found by substituting the solution of (3-41) in the following equation, which is a modification of the pump power equation (3-8),

$$V_{\mathrm{p},n} = \frac{P_{\mathrm{p},n}}{\omega_n \eta_\mathrm{v} \Delta\bar{p}}. \tag{3-42}$$

Next, the nozzle area can be recalculated by using (3-5) and the substitution of $Q_{\mathrm{nz}} = \sum_{n}^{N} P_{\mathrm{p},n} \left(\Delta p_{\mathrm{p}}\right)^{-1}$, which comes from the pump power equation (3-8) and the fact that the nozzle flow is the sum of pump flows in the control model. The resulting equation for the nozzle area is given by

$$A_{\mathrm{nz}} = \sum_{n=1}^{N} P_{\mathrm{p},n} \left(C_{\mathrm{d}} \sqrt{\frac{2\Delta\overline{p}^3}{\rho_{\mathrm{w}}}} \right)^{-1}. \tag{3-43}$$

The corresponding value of the spear position is then given by the modification of (3-6),

$$s = s_{\mathrm{max}} - \sqrt{\frac{A_{\mathrm{nz}}/\pi - D_{\mathrm{nz}}^2/4}{-\tan^2(\alpha/2)}}. \tag{3-44}$$

The blade pitch angles β_{n} are found considering its role in determining the rotor power P_{r}, as described by (3-2). Assuming that the rotor-effective wind speed v_n can be estimated or measured by, e.g., a wind speed estimator or light detection and ranging (LIDAR) sensor. This enables the power coefficient $C_{\mathrm{P},n}$ to be calculated using

$$C_{\mathrm{P},n} = \frac{P_{\mathrm{r},n}}{\frac{1}{2}\rho_{\mathrm{a}} A v_n^2}. \tag{3-45}$$

The coefficient is dependent on both the blade pitch angle β_n and tip speed ratio λ_n. The tip speed ratio can be derived by combining (3-41) and the definition of the tip speed ratio (2-3),

$$\lambda_n = \frac{R}{v_n}\sqrt{\frac{2K_n}{J}}. \tag{3-46}$$

Since the power coefficient and the TSR are known, a corresponding pitch angle is obtained using the power coefficient data, shown in Figure 2-3. By searching for points of intersection between the calculated tip speed ratio and the contour line corresponding to the calculated power coefficient, one or multiple pitch angle candidates may be found. In the case that multiple possible pitch angle solutions are found, they should be evaluated on the pitch constraints posed by (3-15) and discarded if they do not comply. A lookup table is constructed to find the pitch angle which results in the lowest error between the calculated power coefficient value and known power coefficient table value:

$$\beta_n = \beta \mathrel{\widehat{=}} \min |C_{\mathrm{P}}(\beta, \lambda_n) - C_{\mathrm{P},n}|. \tag{3-47}$$

Chapter 4

Convex Economic MPC framework: Implementation and Additional Features

This chapter discusses the implementation of the theoretical convex economic model predictive control (CEMPC) framework, introduced in the previous chapter. Furthermore, it elaborates on additional framework features that improve the accuracy of the internal model and the performance of the controller when used on a simulated plant model.

First, the base implementation of the theoretical CEMPC framework is discussed in Section 4-1. Section 4-2 elaborates on the addition of varying pump efficiencies in the theoretical framework. The implementation of feedback measurements is described in Section 4-3. Next, Section 4-4 discusses additional optimization objectives that are implemented to improve the prediction and controller performance. The implemented optimization problem is presented in Section 4-5. Finally, an overview of the implemented control diagram is shown in 4-6.

4-1 Convex economic MPC implementation

The CEMPC that is implemented for the hydraulic-drivetrain wind farm (HWF) is shown in Figure 4-1. The controller uses measurements that are taken from all wind turbines in the power plant. The rotor speed is used together with measured blade pitch angles and pump torques to provide an estimate of the rotor-effective wind speed using an immersion and invariance (I&I) wind speed estimator [47]. Furthermore, in real life, controllers are employed on a digital computer system and true systems are continuous.

To simulate this difference, higher sampling rates are chosen for the true system model than for the CEMPC controller. For this reason, the control inputs that are provided by the controller need to be interpolated to avoid large input transients.

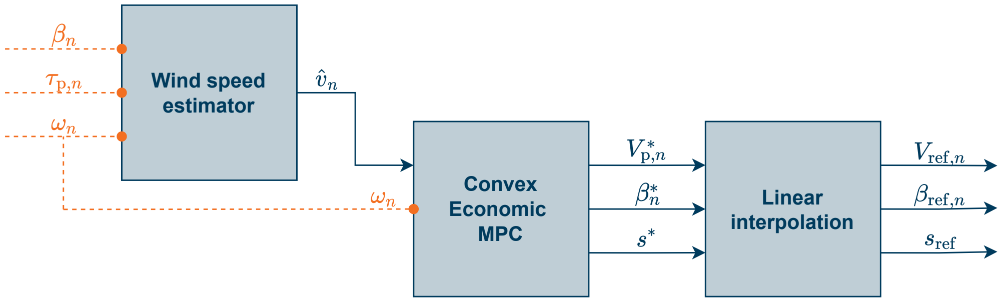

Figure 4-1: A block diagram that shows the basic features of the implemented CEMPC framework. Measurements of the blade pitch angles β_n, pump torques $\tau_{\mathrm{p},n}$, and rotor speeds ω_n are used by an I&I wind speed estimator to obtain estimated values $\hat{v}_n$ of the rotor effective wind speeds v_n acting on each wind turbine n. These values are fed into the CEMPC controller. Other inputs of the controller are the measured rotor speeds ω_n. The optimized controller outputs consist of the solution trajectories of the pump displacements $V_{\mathrm{p},n}$, blade pitch angles β_n, and spear valve position s. The solutions of the first time step in the predicted future are selected and linearly interpolated to avoid large input transients. Note that in this chapter additional features will be included, the final implemented control diagram is presented in Section 4-6.

4-1-1 Linear interpolation of controller outputs

In real controller implementations in wind farms, the frequency in which the controller is updated is very unlikely to be as fast as the frequency at which the real wind turbine plant states change. In this work, a difference in operating frequencies has been implemented in the form of using different sampling rates. The outputs of the controller are interpolated linearly between model predictive control (MPC) iterations to prevent large wind turbine input transients. The CEMPC framework can adequately account for the linear interpolation of the outputs by using a first-order-hold discretization method, which is discussed in Section 4-1-3.

4-1-2 Wind speed estimation

With current wind speed measuring devices, it is not possible to accurately measure the rotor effective wind speed v. Therefore, it is estimated by an I&I estimator [39, 47]. This estimator uses a smart adaptive parameter estimation technique to the rotor speed dynamics to generate an estimate for the effective wind speed. Measurements from the rotor speed and collective blade pitch angles, together with the measured reactive pump torque on the rotor shaft, are used in the rotor torque and rotor speed dynamics equations given by (2-6) and (2-7), respectively. The pump torques could be obtained using toque measurement techniques described in [79]. An easier approach would be to approximate the pump torque using a pump pressure measurement and the known pump displacement setting. In this thesis, it is assumed that the pump torque can be directly measured. For clarity, the rotor torque equation is repeated,

$$\tau_{\mathrm{r}}\left(\omega,v\right)=\frac{1}{2}\rho_{\mathrm{a}}A\frac{v^3}{\omega}C_P(\omega,v) \tag{4-1}$$

The I&I torque balance estimator for a direct-drive hydraulic-drivetrain wind turbine (HWT) is defined as

$$\begin{cases}\dot{\hat{v}}^I=\frac{\gamma}{J}\left[\tau_{\mathrm{p}}-\tau_{\mathrm{r}}\left(\omega,\hat{v}^I+\gamma\omega\right)\right]\\ \hat{v}=\hat{v}^I+\gamma\omega\end{cases}, \tag{4-2}$$

where $\hat{v}$ is the estimate of the wind speed v and $\gamma>0$ is an adaption gain. By selecting a sufficient high adaption gain, the estimator offers asymptotic convergence to not only constant but also variable wind speeds. Interested readers are referred to [39, 47] for more details.

In this work, it is assumed that the controller does not have the ability to perform wind speed previewing. Such that the controller framework, proposed in this thesis, could be compared with existing or future controllers which do not consider wind speed previewing. Instead, the estimated wind speed $\hat{v}$ is assumed to remain constant throughout the entire prediction horizon.

4-1-3 Discretization

Most practical applications of MPC are based on discrete-time models [74]. As such, this thesis will focus on the discrete-time implementation of the CEMPC. Therefore, the continuous-time optimization problem, described in Section 3-2-4, needs to be discretized.

First, the mapping between the discrete and continuous time indications k and t, is given by $t=t_0+k\Delta t_{\mathrm{MPC}}$, where Δt_{MPC} is the MPC step size. The discrete MPC optimization for N_{p} prediction time steps, is shown in the equations (4-3)-(4-11). The integral in (3-40) can be approximated by the sum of the objective terms at the discrete intervals within the time horizon, displayed in (4-3). To discretize the inequality constraints posed by (3-27), (3-28), (3-30), and (3-31), simply apply each of these equations at all the time steps k within the prediction horizon. The resulting optimization objective with inequality constraints for every turbine n in the system are given by,

$$\max_{\underline{P}_\mathrm{r},\underline{P}_\mathrm{p}} \quad \sum_{k=1}^{N_\mathrm{p}}\sum_{n=1}^{N} P_{\mathrm{p},n}[k] \tag{4-3}$$

subjected to:

$$
\begin{aligned}
&K_n[k] \geq K_\mathrm{min}, && k \in \{1,2,\dots,N_\mathrm{p}\},\, n \in \{1,2,\dots,N\}, && \text{(4-4)}\\
&K_n[k] \leq K_\mathrm{max}, && k \in \{1,2,\dots,N_\mathrm{p}\},\, n \in \{1,2,\dots,N\}, && \text{(4-5)}\\
&P_{\mathrm{p},n}[k] \geq P_\mathrm{min}, && k \in \{1,2,\dots,N_\mathrm{p}\},\, n \in \{1,2,\dots,N\}, && \text{(4-6)}\\
&P_{\mathrm{p},n}[k] \leq P_\mathrm{rated}, && k \in \{1,2,\dots,N_\mathrm{p}\},\, n \in \{1,2,\dots,N\}, && \text{(4-7)}\\
&P_{\mathrm{p},n}[k] \geq 0, && n \in \{1,2,\dots,N\}, && \text{(4-8)}\\
&P_{\mathrm{p},n}[k] \leq V_\mathrm{max}\sqrt{\frac{2K_n[k]}{J}}\eta_\mathrm{v}\Delta\overline{p}, && k \in \{1,2,\dots,N_\mathrm{p}\},\, n \in \{1,2,\dots,N\}, && \text{(4-9)}\\
&P_{\mathrm{r},n}[k] \geq 0, && k \in \{1,2,\dots,N_\mathrm{p}\},\, n \in \{1,2,\dots,N\}, && \text{(4-10)}\\
&P_{\mathrm{r},n}[k] \leq \hat{P}_\mathrm{av}(v_n[k],K_n[k]), && k \in \{1,2,\dots,N_\mathrm{p}\},\, n \in \{1,2,\dots,N\}, && \text{(4-11)}
\end{aligned}
$$

where N is the total amount of turbines in the system, $\underline{P}_\mathrm{r}$, and $\underline{P}_\mathrm{p}$ are matrices containing the aerodynamic power and pump power of each turbine at every time step within the prediction horizon, given as

$$\underline{P}_\mathrm{r} = \begin{bmatrix} P_{\mathrm{r},1}[1] & P_{\mathrm{r},1}[2] & \dots & P_{\mathrm{r},1}[N_\mathrm{p}] \\ P_{\mathrm{r},2}[1] & P_{\mathrm{r},2}[2] & \dots & P_{\mathrm{r},2}[N_\mathrm{p}] \\ \vdots & \vdots & \ddots & \vdots \\ P_{\mathrm{r},n}[1] & P_{\mathrm{r},n}[2] & \dots & P_{\mathrm{r},n}[N_\mathrm{p}] \end{bmatrix}^\top, \tag{4-12}$$

$$\underline{P}_\mathrm{p} = \begin{bmatrix} P_{\mathrm{p},1}[1] & P_{\mathrm{p},1}[2] & \dots & P_{\mathrm{p},1}[N_\mathrm{p}] \\ P_{\mathrm{p},2}[1] & P_{\mathrm{p},2}[2] & \dots & P_{\mathrm{p},2}[N_\mathrm{p}] \\ \vdots & \vdots & \ddots & \vdots \\ P_{\mathrm{p},n}[1] & P_{\mathrm{p},n}[2] & \dots & P_{\mathrm{p},n}[N_\mathrm{p}] \end{bmatrix}^\top. \tag{4-13}$$

As described in Section 2-6, the control inputs computed by the MPC algorithm are linearly interpolated before they are used by the true system model because of a difference in sampling times. Therefore, the rotor speed dynamics are discretized using the first-order-hold method. The resulting discrete representation of the rotor kinetic energy dynamics are given by

$$x_{\mathrm{d},n}[k+1] = A_\mathrm{d}x_{\mathrm{d},n}[k] + B_\mathrm{d}\left[P_{\mathrm{r},n}[k] \quad P_{\mathrm{p},n}[k]\right]^\top, \tag{4-14}$$

$$K_n[k] = C_\mathrm{d}x_{\mathrm{d},n}[k] + D_\mathrm{d}\left[P_{\mathrm{r},n}[k] \quad P_{\mathrm{p},n}[k]\right]^\top, \tag{4-15}$$

where discrete variables are denoted with the subscript 'd', x_d is the discrete state that is used to describe the rotor kinetic energy dynamics (3-26), together with the discrete state space matrices $A_\mathrm{d}, B_\mathrm{d}, C_\mathrm{d}, D_\mathrm{d}$.

When applying (4-14) and (4-15) to all the N_p steps within the prediction horizon, one single matrix equality can be derived that defines all the kinetic energies given the current, measured kinetic energy and the MPC inputs:

$$\underline{K} = \mathcal{A}\underline{K_0} + \mathcal{B}_\mathrm{r}\underline{P}_\mathrm{r} + \mathcal{B}_\mathrm{p}\underline{P}_\mathrm{p}, \tag{4-16}$$

where $\mathcal{A}$, $\mathcal{B}_\mathrm{r}$, and $\mathcal{B}_\mathrm{p}$ contain the state-space matrices of (4-14) and (4-15) for all wind turbines in the system and all time steps, $\underline{K_0}$ is a vector containing the current rotor kinetic energies of all wind turbines N, used as initial condition for the MPC iteration,

$$\underline{K_0} = \begin{bmatrix} K_1[0] & K_2[0] & \dots & K_n[0] \end{bmatrix}^\top, \tag{4-17}$$

and $\underline{K}$ is a matrix containing the kinetic rotor energy of every time step within the prediction horizon for all turbines, given as

$$\underline{K} = \begin{bmatrix} K_1[0] & K_1[1] & K_1[2] & \dots & K_1\left[N_\mathrm{p}\right] \\ K_2[0] & K_2[1] & K_2[2] & \dots & K_2\left[N_\mathrm{p}\right] \\ \vdots & \vdots & \vdots & \ddots & \vdots \\ K_n[0] & K_n[1] & K_n[2] & \dots & K_n\left[N_\mathrm{p}\right] \end{bmatrix}^\top. \tag{4-18}$$

4-1-4 Time step size and prediction horizon length selection

The choice of the time step size Δt_MPC and the prediction horizon length N_p are important for the effective implementation of the MPC controller. The step size should be small enough such that the internal prediction model is able to correctly resemble the dynamics of the controlled system. The prediction horizon determines how many predicted steps in the future the MPC controller considers in the optimization. If a control action in the system is known to have a long-term effect on the system output, it may be beneficial to have a long prediction horizon, such that the MPC controller can take this effect into account in the optimization of the control inputs. However, the combination of small step sizes and long prediction horizons result in long computation times, which may cause the controller to become too slow to effectively control the system. Therefore, it is important to diligently tune both parameters.

In the original CEMPC framework, developed by Hovgaard et al. in [31], the step size is set to $\Delta t_\mathrm{MPC} = 0.2$ seconds and a prediction horizon of $N_\mathrm{p} = 50$ time steps, resulting in a prediction time of 10 seconds. It is found that for the implemented system model, the original prediction is sufficiently long for the controller to steer the system towards a predicted optimal steady-state.

4-2 Addition of varying pump efficiencies

In the current description of the CEMPC, the consequences of the optimized control actions on the varying pump efficiencies, described in Section 2-2-1, are not taken into account. This contributes to a model mismatch between the internal control model and the implemented model of the true system. In this section, an effort is made to include varying pump efficiencies in the convex control model.

For clarity, the original equations of the pump efficiencies are restated

$$\eta_{\mathrm{v},n} = 1 - C_{\mathrm{s}} \frac{\Delta \bar{p}}{V_{\mathrm{p},n} \mu \omega_n}, \tag{4-19}$$

$$\eta_{\mathrm{m},n} = \left(1 + C_{\mathrm{damp}} \frac{\mu \omega_n}{\Delta \bar{p}} + C_{\mathrm{f}}\right)^{-1}. \tag{4-20}$$

These equations can not directly be used by the internal control model, as they are described by the original system variables. To conform to the CEMPC requirements, it is imperative to transform the efficiency formulations in terms of P_{p} or P_{r}, while considering the convexity of the control model dynamics (3-26) and pump power constraint (3-30). The volumetric efficiency term can be modified into a convex function of the pump power by using the substitution $V_{\mathrm{p}} = P_{\mathrm{p},n}/(\omega \eta_{\mathrm{v}} \Delta \bar{p}_n)$ in (4-19) and the constant pressure assumption, described in Section 3-2-2,

$$\eta_{\mathrm{v},n} = \left(1 + \frac{C_{\mathrm{s}} \Delta \bar{p}^2}{\mu P_{\mathrm{p,n}}}\right)^{-1}. \tag{4-21}$$

The resulting response is presented in Figure 4-2a. It must be noted that it is assumed that the laminar leakage coefficient of the pump is known.

Where it is possible to obtain a function of the volumetric efficiency in terms of the available variables, this is unfortunately not the case for the mechanical efficiency function posed in equation (4-20). However, when examining the values of η_{m} for different pressures and rotor speeds displayed in Figure 4-2b, it is seen that the mechanical efficiency does not deviate much from the rated value 0.97 for the posed operating range. Therefore, this efficiency term is assumed to remain constant at $\eta_{\mathrm{m}} = 0.97$.

The new convex kinetic rotor energy dynamics are obtained by substituting (4-21) in (3-26) and given by

$$\dot{K}_n = P_{\mathrm{r},n} - \frac{P_{\mathrm{p},n}}{\eta_{\mathrm{m}}} - \frac{C_s \Delta \bar{p}^2}{\mu \eta_{\mathrm{m}}}. \tag{4-22}$$

The constraint posed in (4-7) is altered to the following expression:

$$P_{\mathrm{p},n}[k] \leq V_{\max} \sqrt{\frac{2K_n[k]}{J}} \Delta \bar{p} - \frac{C_s \Delta \bar{p}^2}{\mu \eta_{\mathrm{m}}}, \quad k \in \{1, 2, \ldots, N_{\mathrm{p}}\}, \, n \in \{1, 2, \ldots, N\}. \tag{4-23}$$

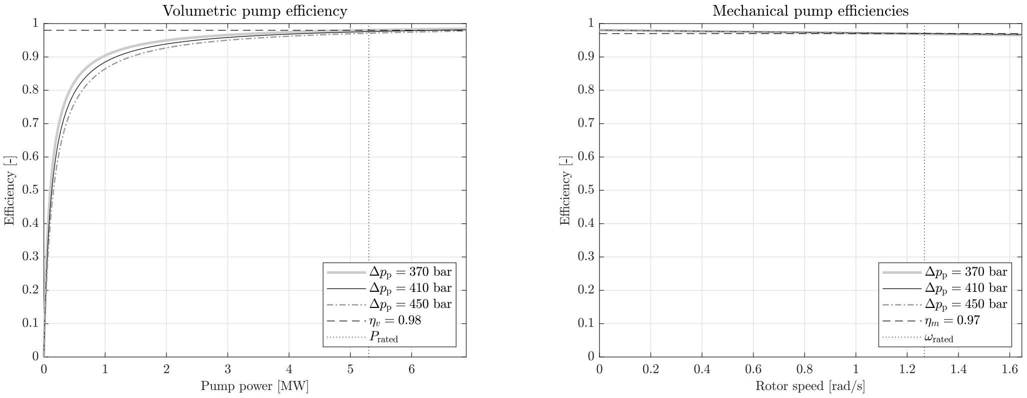

(a) Volumetric pump efficiency as a convex function of the rotor power P_p.

(b) Original mechanical pump efficiency as a function of the rotor speed ω.

Figure 4-2: Pump efficiency functions. (a) The simulated volumetric efficiency η_v as a function of the pump power P_p for different pressures around the nominal value $\Delta p_\text{p} = 410$ bar. The rated values of $\eta_\text{v} = 0.98$, $\eta_\text{m} = 0.97$, ω_rated, and P_rated are also depicted. (b) The original mechanical efficiency as a function of ω. The efficiency value remains very close to the rated value throughout the entire operation region.

4-3 Plant measurements and feedback implementation

The internal MPC control model is a simplified model of the plant. Hence, when only using the internal control model, an error between the implemented control model and the true system accumulates over time. To minimize this error, feedback is included in the CEMPC framework by implementing hard equality constraints on the kinetic rotor energies at the current time k=0 and soft power offset penalizing optimization objectives for the first time step k=1. Moreover, measurements of the pump and nozzle pressures are used to obtain a more accurate convex to original control variable mapping of the nozzle area, described in Section 3-2-5. Finally, an additional constraint is included to prevent the pump flow to become lower than the cut-in flow, described in Section 2-3-2.

Pressure measurements

Up until this point, it is assumed by the CEMPC framework that the pressures throughout the network are all equal, but as it is possible to measure each pump and nozzle pressure, the CEMPC is able to consider these differences.

$$\Delta\overline{p}_n = \Delta p_{\mathrm{pm},n}, \tag{4-24}$$

$$\Delta\overline{p}_{\mathrm{nz}} = \Delta p_{\mathrm{nz_m}}, \tag{4-25}$$

$$\tag{4-26}$$

where $\Delta p_{\mathrm{pm},n}$ are the measured pump- and $\Delta p_{\mathrm{nz_m}}$ nozzle pressure.

The dynamics and constraint equations in (4-22) and (4-23), are modified to

$$\dot{K}_n = P_{\mathrm{r},n} - \frac{P_{\mathrm{p},n}}{\eta_\mathrm{m}} - \frac{C_s \Delta\overline{p}_n^2}{\mu\eta_\mathrm{m}}, \tag{4-27}$$

$$P_{\mathrm{p},n}[k] \leq V_{\max}\sqrt{\frac{2K_n[k]}{J}}\Delta\overline{p}_n - \frac{C_s\Delta\overline{p}_n^2}{\mu\eta_\mathrm{m}}, \quad k \in \{1,2,\ldots,N_\mathrm{p}\}, \, n \in \{1,2,\ldots,N\}, \tag{4-28}$$

where the dynamics in (4-27) are discretized using the method discussed in Section 4-1-3.

Kinetic rotor energy feedback

By using rotor speed measurements, the kinetic rotor energies at the current time $k = 0$ can be derived, which is then used as a hard constraint in

$$K_n[0] = \frac{1}{2}J\omega_{\mathrm{m},n}^2, \tag{4-29}$$

where $\omega_{\mathrm{m},n}$ are the measured rotor speeds.

Power feedback

To provide feedback on the aerodynamic and pump power, wind speed estimates $\hat{v}_n$ together with measurements of the pitch angles, pump displacements, rotor speeds, and pump pressures are used to find estimates of the powers at the start of each MPC cycle.

$$P_{\mathrm{r0},n} = \frac{1}{2}\rho A C_\mathrm{P}\left(\beta_{\mathrm{m},n}, \frac{\omega_{\mathrm{m},n}R}{\hat{v}_n}\right)\hat{v}_n^3, \tag{4-30}$$

$$P_{\mathrm{p0},n} = V_{\mathrm{pm},n}\omega_{\mathrm{m},n}\Delta\overline{p}_n, \tag{4-31}$$

in which $\beta_{\mathrm{m},n}$ are the measured pitch angles, $V_{\mathrm{pm},n}$ are the measured pump displacements. The estimates are used in the following optimization objectives which need to be maximized:

$$\epsilon_\mathrm{r} = -\left(P_{\mathrm{r},n}[1] - P_{\mathrm{r0},n}\right)^2, \tag{4-32}$$

$$\epsilon_\mathrm{p} = -\left(P_{\mathrm{p},n}[1] - P_{\mathrm{p0},n}\right)^2. \tag{4-33}$$

The abovementioned optimization objectives pose a soft constraint on the optimized rotor and pump powers for the first predicted time step at $k = 1$. Values that are far from the measured values will be penalized. This way, the first predicted rotor and pump powers remain close to the estimated true values, and therefore the model-mismatch between the internal control model and true system is mitigated.

Improved nozzle area retrieval

Using the measured nozzle pressure in (4-25), a more accurate mapping of optimized convex control variables $P_{\mathrm{p},n}$ and K_n to the original spear valve area control variable, described in (3-43) becomes

$$A_{\mathrm{nz}} = \sum_{n=1}^{N} V_{\mathrm{p},n}\omega_n \Delta\overline{p}_{\mathrm{nz}}\eta_{\mathrm{v},n} \left(C_{\mathrm{d}}\sqrt{\frac{2\Delta\overline{p}_{\mathrm{nz}}^{3}}{\rho_{\mathrm{w}}}} \right)^{-1}, \tag{4-34}$$

note that $V_{\mathrm{p},n}$, ω_n, and η_{v} are derived from $P_{\mathrm{p},n}$ and K_{n}.

Cut-in flow constraint

To avoid the hydrailic dynamics to become unstable for operations at low wind speeds, an additional constraint is introduced to prevent the pump flow to decrease below the cut-in value described in Section 2-3-2. As the flow can be described by $Q_{\mathrm{p},n} = P_{\mathrm{p},n}/\Delta\overline{p}$, the following constraint is added:

$$P_{\mathrm{p},n} \geq Q_{\mathrm{cutin}}\Delta\overline{p}. \tag{4-35}$$

4-4 Additional optimization objectives

The performance of the CEMPC framework can be improved by including additional optimization objectives. These objectives aim to either increase the realism of the optimized predictions and control signal sequence or enhance the capability of the controller to mitigate negative effects that could occur in the system.

4-4-1 Limiting power and kinetic energy rates

To ensure a smooth predicted power sequence, and as an attempt to account for hydraulic- and actuator dynamics, equations (4-32) and (4-33) can be extended such that the rate of change of the kinetic rotor energies, rotor powers, and pump powers in the optimized input sequence is limited. The resulting expressions are given by

$$\epsilon_{\mathrm{K},n}[k] = \Big\{ -\left(K_n[k] - K_n[k-1]\right)^2, \quad \forall k, \tag{4-36}$$

$$\epsilon_{\mathrm{r},n}[k] = \begin{cases} -\left(P_{\mathrm{r},n}[k] - P_{\mathrm{r_0},n}\right)^2, & \text{for } k=1 \\ -\left(P_{\mathrm{r},n}[k] - P_{\mathrm{r},n}[k-1]\right)^2, & \text{otherwise} \end{cases}, \tag{4-37}$$

$$\epsilon_{\mathrm{p},n}[k] = \begin{cases} -\left(P_{\mathrm{p},n}[k] - P_{\mathrm{p_0},n}\right)^2, & \text{for } k=1 \\ -\left(P_{\mathrm{p},n}[k] - P_{\mathrm{p},n}[k-1]\right)^2, & \text{otherwise} \end{cases}. \tag{4-38}$$

4-4-2 Overspeeding

When the rotor operates at an angular velocity larger than the rated rotor speed, acoustic noise, and centrifugal forces may arise [18]. The controller should mitigate these negative effects by attempting to limit the rotational speed to its rated value [4]. An additional objective is therefore introduced, penalizing any kinetic rotor energy that surpasses the rated kinetic rotor energy. The anti-overspeeding objective can be written as a linear optimization objective combined with linear constraints, which is described in the method below [18].

In conformity with the discretization method described in Section 4-1-3, the discrete anti-overspeeding objective is given as

$$\epsilon_{\mathrm{o},n}[k] = -\max\left\{K_n[k] - K_{\mathrm{rated}}\ , 0\right\}. \tag{4-39}$$

The sum is taken from $k = 1$ instead of the current time step $k = 0$ because the kinetic rotor energy $K[0]$ is determined by the equality constraint posed in Section 4-3. Reckon that (4-39) can be reformulated as a linear function

$$\max\{a, b\} = \frac{a+b}{2} + \frac{|a-b|}{2}, \tag{4-40}$$

where a and b are two real numbers.

By utilizing (4-40) in (4-39), the anti-overspeeding objective yields

$$\epsilon_{\mathrm{o},n}[k] = -\frac{K_n[k] - K_{\mathrm{rated}}}{2} - \frac{|K_n[k] - K_{\mathrm{rated}}\ |}{2}. \tag{4-41}$$

The absolute values $|K[k] - K_{\mathrm{rated}}\ |$ are replaced with new 'overspeed' variables $\sigma_{\mathrm{K},n}[k]$, which make the objective in accordance with the convex optimization problem requirements. The final representation of the objective is given by

$$\epsilon_{\mathrm{o},n}[k] = -\frac{1}{2}\left(K_n[k] - K_{\mathrm{rated}}\ + \sigma_{\mathrm{K},n}[k]\right). \tag{4-42}$$

The new introduced ovespeed variables need to be bound by affine constraints

$$\sigma_{\mathrm{K},n}[k] \geq K[k] - K_{\mathrm{rated}}\ , \qquad k \in \{1, 2, \ldots, N_{\mathrm{p}}\}\,,\ n \in \{1, 2, \ldots, N\}\,, \tag{4-43}$$

$$\sigma_{\mathrm{K},n}[k] \geq -K[k] + K_{\mathrm{rated}}\ , \qquad k \in \{1, 2, \ldots, N_{\mathrm{p}}\}\,,\ n \in \{1, 2, \ldots, N\}\,. \tag{4-44}$$

The vector containing the overspeed variables of every time step within the prediction horizon is given as

$$\underline{\sigma_{\mathrm{K}}} = \begin{bmatrix} \sigma_{\mathrm{K},1}[1] & \sigma_{\mathrm{K},1}[2] & \ldots & \sigma_{\mathrm{K},1}\,[N_{\mathrm{p}}] \\ \sigma_{\mathrm{K},2}[1] & \sigma_{\mathrm{K},2}[2] & \ldots & \sigma_{\mathrm{K},2}\,[N_{\mathrm{p}}] \\ \vdots & \vdots & \ddots & \vdots \\ \sigma_{\mathrm{K},n}[1] & \sigma_{\mathrm{K},n}[2] & \ldots & \sigma_{\mathrm{K},n}\,[N_{\mathrm{p}}] \end{bmatrix}^{\top}. \tag{4-45}$$

4-4-3 Turnpike mitigation

A common problem in economic model predictive control (EMPC) implementations that the authors of the original CEMPC framework do not discuss in [31] is a problem named 'turnpike'. Turnpike occurs when the kinetic rotor energy is not restricted at the end of the prediction horizon $k = N_{\mathrm{p}}$. The controller will increase the pump power throughout the end of the prediction horizon by decreasing the kinetic rotational energy in the process [18]. It is possible to account for turnpike by including the term [18]

$$\epsilon_{\mathrm{tp},n} = \eta_{\mathrm{m}} K_n \left[N_{\mathrm{p}}\right], \tag{4-46}$$

which is maximized by the optimization algorithm [28].

A downside of this objective is that it is contradictory to the anti-overspeeding objective, as it rewards kinetic rotor energy values above the rated kinetic energy value. Therefore, a modified representation is used, in which only kinetic rotor energies below the rated rotor kinetic energy are rewarded [18]:

$$\epsilon_{\mathrm{tp},n} = \eta_{\mathrm{m}} \left[K_n \left[N_{\mathrm{p}}\right] - \frac{1}{2}\left(K_n \left[N_{\mathrm{p}}\right] - K_{\mathrm{rated}} \ + \sigma_{\mathrm{K},n}\left[N_{\mathrm{p}}\right]\right)\right], \tag{4-47}$$

in which the subtracted term denotes rotor kinetic energies higher than the rated value.

4-5 Implemented optimization problem

When collecting all the original, modified, and additional objectives and constraints, presented in the previous sections, the resulting optimization problem is given by

$$
\begin{aligned}
\min_{\underline{P}_{\mathrm{r}},\underline{P}_{\mathrm{p}},\underline{\sigma}_{\mathrm{K}}} \quad \sum_{n=1}^{N} \Bigg[& \underbrace{\alpha_2 \left(P_{\mathrm{r},n}[1] - P_{\mathrm{r0},n}\right)^2}_{\text{rotor power feedback}} + \underbrace{\alpha_3 \left(P_{\mathrm{p},n}[1] - P_{\mathrm{p0},n}\right)^2}_{\text{pump power feedback}} \\
& + \sum_{k=1}^{N_{\mathrm{p}}} \left(- \underbrace{\alpha_1 P_{\mathrm{p},n}[k]}_{\text{maximize power}} + \underbrace{\alpha_5 \frac{K_n[k] - K_{\mathrm{rated}} + \sigma_{\mathrm{K},n}[k]}{2}}_{\text{minimize overspeeding}} + \underbrace{\alpha_4 \left(K_n[k] - K_n[k-1]\right)^2}_{\text{minimize kinetic energy variations}} \right) \\
& + \sum_{k=2}^{N_{\mathrm{p}}} \left(\underbrace{\alpha_2 \left(P_{\mathrm{r},n}[k] - P_{\mathrm{r},n}[k-1]\right)^2}_{\text{minimize rotor power variations}} + \underbrace{\alpha_3 \left(P_{\mathrm{p},n}[k] - P_{\mathrm{p},n}[k-1]\right)^2}_{\text{minimize pump power variations}} \right) \\
& - \underbrace{\alpha_6 \eta_{\mathrm{m}} \left[K_n\left[N_{\mathrm{p}}\right] - \frac{1}{2}\left(K_n\left[N_{\mathrm{p}}\right] - K_{\mathrm{rated}} + \sigma_{\mathrm{K},n}\left[N_{\mathrm{p}}\right]\right) \right]}_{\text{turnpike mitigation}} \Bigg]
\end{aligned}
$$

subjected to:

$$\tag{4-48}$$

$$
\begin{aligned}
\underline{K} &= \mathcal{A}\underline{K_0} + \mathcal{B}_{\mathrm{r}}\underline{P}_{\mathrm{r}} + \mathcal{B}_{\mathrm{p}}\underline{P}_{\mathrm{p}}, && && \text{(4-16)}\\
K_n[0] &= K_{0,n}, && k \in \{1,2,\dots,N_{\mathrm{p}}\},\ n \in \{1,2,\dots,N\}, && \text{(4-29)}\\
K_n[k] &\geq K_{\mathrm{min}}, && k \in \{1,2,\dots,N_{\mathrm{p}}\},\ n \in \{1,2,\dots,N\}, && \text{(4-4)}\\
K_n[k] &\leq K_{\mathrm{max}}, && k \in \{1,2,\dots,N_{\mathrm{p}}\},\ n \in \{1,2,\dots,N\}, && \text{(4-5)}\\
P_{\mathrm{p},n}[k] &\geq P_{\mathrm{min}}, && k \in \{1,2,\dots,N_{\mathrm{p}}\},\ n \in \{1,2,\dots,N\}, && \text{(4-6)}\\
P_{\mathrm{p},n}[k] &\geq Q_{\mathrm{cutin}}\Delta\overline{p}, && k \in \{1,2,\dots,N_{\mathrm{p}}\},\ n \in \{1,2,\dots,N\}, && \text{(4-35)}\\
P_{\mathrm{p},n}[k] &\leq P_{\mathrm{rated}}, && k \in \{1,2,\dots,N_{\mathrm{p}}\},\ n \in \{1,2,\dots,N\}, && \text{(4-7)}\\
P_{\mathrm{p},n}[k] &\geq 0, && k \in \{1,2,\dots,N_{\mathrm{p}}\},\ n \in \{1,2,\dots,N\}, && \text{(4-10)}\\
P_{\mathrm{p},n}[k] &\leq V_{\mathrm{max}}\sqrt{\frac{2K_n[k]}{J}}\Delta\overline{p}_n - \frac{C_s\Delta\overline{p}_n^2}{\mu\eta_{\mathrm{m}}}, && k \in \{1,2,\dots,N_{\mathrm{p}}\},\ n \in \{1,2,\dots,N\}, && \text{(4-23)}\\
P_{\mathrm{r},n}[k] &\geq 0, && k \in \{1,2,\dots,N_{\mathrm{p}}\},\ n \in \{1,2,\dots,N\}, && \text{(4-10)}\\
P_{\mathrm{r},n}[k] &\leq \hat{P}_{\mathrm{av}}(v_n[k], K_n[k]), && k \in \{1,2,\dots,N_{\mathrm{p}}\},\ n \in \{1,2,\dots,N\}, && \text{(4-11)}\\
\sigma_{\mathrm{K},n}[k] &\geq K[k] - K_{\mathrm{rated}}\ , && k \in \{1,2,\dots,N_{\mathrm{p}}\},\ n \in \{1,2,\dots,N\}, && \text{(4-43)}\\
\sigma_{\mathrm{K},n}[k] &\geq -K[k] + K_{\mathrm{rated}}\ , && k \in \{1,2,\dots,N_{\mathrm{p}}\},\ n \in \{1,2,\dots,N\}, && \text{(4-44)}
\end{aligned}
$$

where the symbols α represent the objective weights, which are used to tune the MPC objective, N_{p} the prediction horizon length, and N denote the number of turbines in the HWF. Note that the obtained objectives are convex, and therefore eligible for the CEMPC control strategy. To make tuning of the objective function more convenient, inputs and states of the system are normalized by their rated and nominal values.

The optimization problem can be solved using a second-order cone programming (SOCP) optimization approach. It is possible to rewrite this optimization problem as a quadratic programming (QP) problem, but it would need some modifications in the used methodology, which are out of the scope of this research. Interested readers are referred to the thesis of R. Dinkla in [18].

4-6 Implemented control diagram for continuously variable displacement pumps hydraulic-drivetrain wind farm

The implemented control diagram is shown in Figure 4-3. The CEMPC framework described can be used for the control of HWFs containing continuously variable displacement pumps. However, as there are HWF concepts that use digital displacement pumps, such as the Delft Offshore Turbine (DOT) turbines, a solution must be found to cope with the discrete nature of the available pump displacements. Solutions found in this thesis will be discussed in the following chapter.

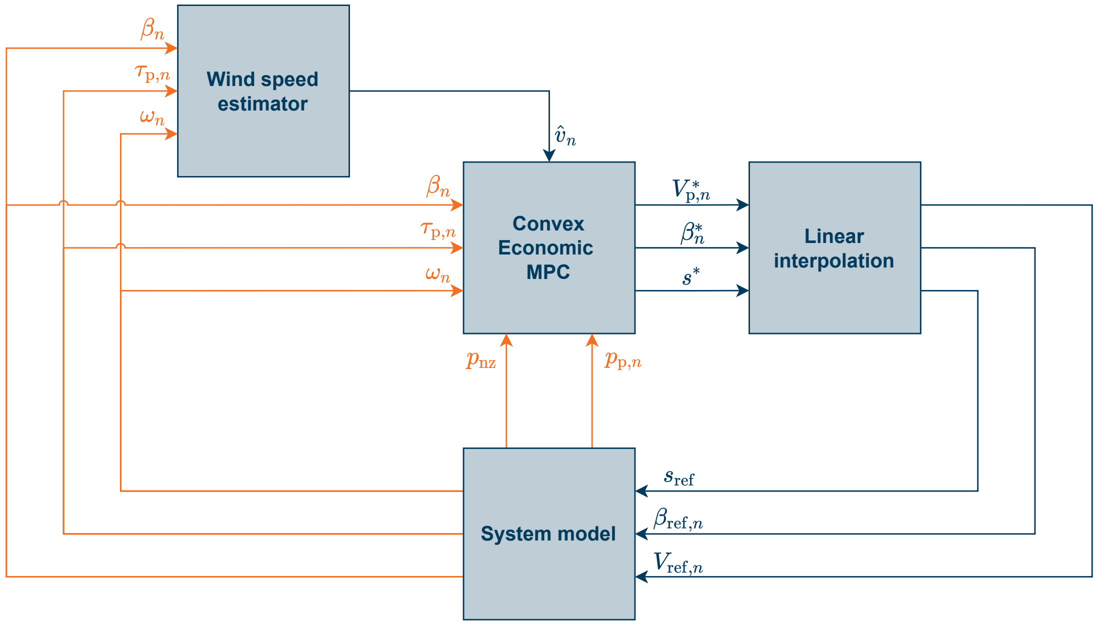

Figure 4-3: A control diagram that shows the dependencies between different controller components and the investigated HWF. A rotor-effective wind speed estimates $\hat{v}_n$ of the wind speeds v_n acting on each wind turbine n is provided to the implemented CEMPC block by an I&I wind speed estimator. Other inputs of the controller comprise measurements of the blade pitch angles β_n, pump torques $\tau_{\mathrm{p},n}$, rotor speeds ω_n, pump pressures $p_{\mathrm{p},n}$, and nozzle pressure p_{nz}. The optimized controller outputs consist of the solution trajectories of the pump displacements $V_{\mathrm{p},n}$, blade pitch angles β_n, and spear valve position s. The solutions of the first time step in the predicted horizon are selected and linearly interpolated to avoid large input transients. These final optimized values are used as inputs of the system model of the HWF.

Chapter 5

Digital Displacement Pump Control

The convex economic model predictive control (CEMPC) framework, derived in the previous chapter, is able to control a hydraulic-drivetrain wind farm (HWF) with turbines that contain continuously variable displacement pumps (CDPs). However, this study is aimed at providing a controller for both CDP- and digital displacement pump (DDP)-hydraulic-drivetrain wind turbines (HWTs). Therefore, an additional algorithm is developed to determine which displacement to select from the discrete set of available pump displacement settings.

First, Section 5-1 explains how the available displacement candidate is derived, based on the CEMPC algorithm provided optimized displacement value. Next, Section 5-2 describes the switching logics used to limit the amount of switching by the algorithm. Finally, an overview of the implemented control diagram for the control of DDP-HWFs is given in Section 5-3.

5-1 Available pump displacement candidate selection

Where a continuously variable displacement pump can realize all the values between the minimum pump displacement $V_{\min}$ and maximum pump displacement $V_{\max}$, a digital displacement pump only has a final set of available displacement settings dependent on the number of active piston chambers, as described in Section 2-2. The available displacement settings are given by the following equation, which is restated from (2-8):

$$V_{\text{p}} = n_{\text{c},i} V_{\text{c}}, \tag{2-8}$$

where $V_{\text{p}} \in \mathbb{Z}^+$ is the total volumetric displacement of the pump, $\{n_{\text{c},i} \subset \mathbb{Z}^+ \mid 1 \leq n_{\text{c},i} \leq n_{\text{c}}\}$ is the number of active piston chambers with n_{c} the maximum number of active pistons, and V_c is the fixed volumetric displacement a single piston chamber for a pump shaft revolution.

A candidate displacement setting is proposed employing a lookup table which finds the closest digital displacement setting of the set $V_\mathrm{p} \in \mathbb{Z}^+$ to the optimized value V_p^* given by the CEMPC algorithm,

$$V_\mathrm{candidate} = \min |V_\mathrm{p}^* - V_\mathrm{p}|. \tag{5-1}$$

5-2 Switching logics

A problem that occurs when only using the selection rule, described in the previous section, is that the controller will switch frequently between the available pump settings. The sudden change in pump displacement can cause the excitation of pipeline dynamics, with undesired pressure and flow peaks as a result. Therefore, it is beneficial to minimize the number of pump displacement switches. By adding barriers for the controller to switch too frequently to the derived displacement candidate, extensive switching is prevented. Two switching rules are used in conjunction for the implemented switching logic.

The first rule only allows the controller to switch when the optimized displacement input V_p^* is within a boundary band of the proposed displacement candidate $V_\mathrm{candidate}$,

$$V_\mathrm{new} = \begin{cases} V_\mathrm{candidate}, & \text{if } |V_\mathrm{p}^* - V_\mathrm{candidate}| < \tau_\mathrm{s} V_\mathrm{c}, \\ V_\mathrm{prev}, & \text{otherwise,} \end{cases} \tag{5-2}$$

where V_new denotes the new displacement setting, V_prev represents the previously selected displacement setting, and τ_s is the switching threshold. In this study, the threshold is chosen to be a percentage of the fixed volumetric displacement of a single-piston chamber V_c. Note that for the threshold value τ_s to have an effect, concerning the nearest available displacement candidate selection described in the previous section, its value should be lower than 0.5. Moreover, when the threshold is not crossed, the selected displacement remains equal to the displacement of the previous time step.

The second switching rule is based on whether switching will reduce the distance to the maximum achievable pump power output, which is estimated using the immersion and invariance (I&I) estimated rotor effective wind speed,

$$P_\mathrm{p,max} = \frac{1}{2}\rho_a A C_\mathrm{P,max} \hat{v}^3 \eta_\mathrm{m} \eta_\mathrm{v}. \tag{5-3}$$

The powers resulting from the new and previously selected displacement settings, V_new and V_prev, respectively, are derived using

$$P_\mathrm{new} = V_\mathrm{new} \omega_\mathrm{m} \eta_\mathrm{v} \Delta p_{\mathrm{p_m}}, \tag{5-4}$$

$$P_\mathrm{prev} = V_\mathrm{prev} \omega_\mathrm{m} \eta_\mathrm{v} \Delta p_{\mathrm{p_m}}, \tag{5-5}$$

where ω_m and $\Delta p_{\mathrm{p_m}}$ are the measured values of the rotor speed and pump pressure, respectively.

The proposed displacement V_new is selected when the distance to the maximum achievable pump power is reduced

$$V_\mathrm{dp} = \begin{cases} V_\mathrm{new}, & \text{if } |P_\mathrm{new} - P_\mathrm{p,max}| < |P_\mathrm{prev} - P_\mathrm{p,max}|, \\ V_\mathrm{prev}, & \text{otherwise.} \end{cases} \tag{5-6}$$

The algorithm stores the selected displacement value as follows:

$$V_\mathrm{prev} = V_\mathrm{dp}. \tag{5-7}$$

5-3 Implemented control diagram for digital displacement wind turbines

The implemented control diagram for the control of HWFs containing digital displacement pumps is shown in Figure 5-1. The performance of the control framework for both CDP-HWTs and DDP-HWTs are presented and discussed in the following chapter.

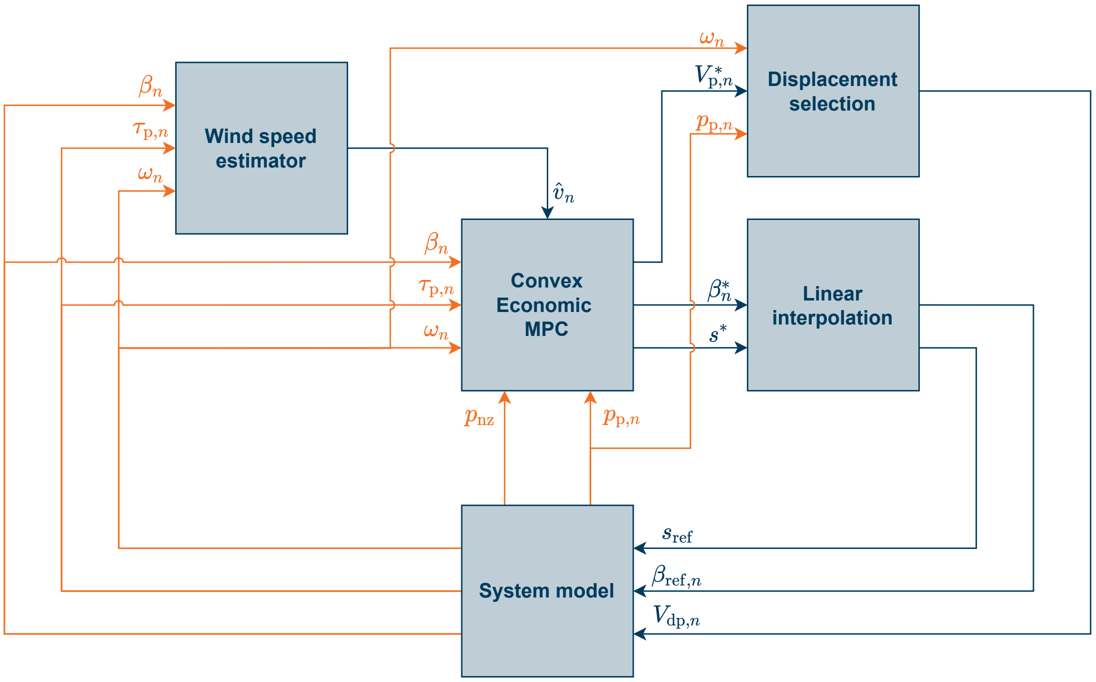

Figure 5-1: A control diagram that shows the dependencies between different control components and the investigated HWF. A rotor-effective wind speed estimates $\hat{v}_n$ of the wind speeds v_n acting on each wind turbine n is provided to the implemented CEMPC block by an I&I wind speed estimator. Other inputs of the controller comprise measurements of the blade pitch angles β_n, pump torques $\tau_{\mathrm{p},n}$, rotor speeds ω_n, pump pressures $p_{\mathrm{p},n}$, and nozzle pressure p_{nz}. The optimized controller outputs consist of the solution trajectories of the pump displacements $V_{\mathrm{p},n}$, blade pitch angles β_n, and spear valve position s. The pitch angle and spear valve position solutions of the first time step in the predicted horizon are selected and linearly interpolated to avoid large input transients. The optimized pump displacement values $V^*_{\mathrm{p},n}$ are used in the displacement selector block to find the suitable discrete displacement settings which can be realized by the digital displacement pumps. These final optimized and selected values are used as inputs of the system model of the HWF.

Chapter 6

Simulation and Results

The previous two chapters presented the convex economic model predictive control (CEMPC) framework for hydraulic-drivetrain wind farms (HWFs) containing continuously variable displacement pumps (CDPs) and digital displacement pumps (DDPs), respectively. This chapter illustrates how these frameworks are incorporated within simulations and presents the results that are obtained. Furthermore, it compares the simulation results of single-turbine and two-turbine HWF control using the proposed CEMPC framework.

Section 6-1 explains the setup with which the CEMPC framework is simulated and elaborates on the goals of the simulation. Thereafter, the optimization objective weight selection is discussed in Section 6-2. Next, the results of the CEMPC for single- and two-turbine HWFs are discussed and compared for four different wind cases. The first wind case, presented in Section 6-3, concerns stair wind profiles throughout the entire operating region of the wind turbines and is used to unravel the behavior of the controller frameworks. Section 6-4 presents the simulation results for a below-rated turbulent wind case. The performance of the framework for simulations of near-rated turbulent wind conditions is discussed in Section 6-5. Section 6-6 refers to above-rated results. A comparison of the estimated yearly energy generation of the controlled hydraulic-drivetrain wind turbines (HWTs) and idealized National Renewable Energy Laboratory (NREL) 5-MW wind turbines is presented in Section 6-7. Finally, concluding remarks are given in Section 6-8.

6-1 Simulation strategy

The goal of the simulation study is to serve as a proof of concept. Moreover, it is used to evaluate the behavior and performance of the novel proposed scalable CEMPC controller framework. The results of controlling single-turbine and two-turbine HWFs are compared. Furthermore, the differences of controlling CDP- and DDP-HWFs are investigated. The two different pump cases will respectively be denoted as (C) and (D) in the remainder of this chapter. An overview of all the simulation, controller, and plant model parameters is given in Appendix A.

Wake effects are out of the scope of this work, therefore, the two turbines in the multi-turbine case are assumed to be placed parallel to each other, as depicted in Figure 6-1, such that their perceived wind is not affected by wake interaction.

The controller performance is evaluated for four different wind speed profiles.

- **Case 1:** Staircase wind signal throughout the complete operational regime
- **Case 2:** Below-rated turbulent wind profile
- **Case 3:** Near-rated turbulent wind profile
- **Case 4:** Above-rated turbulent wind profile

The first wind scenario considers 10-minute (600-second) staircase wind profiles throughout the full operation region and is used to investigate the steady-state performance of

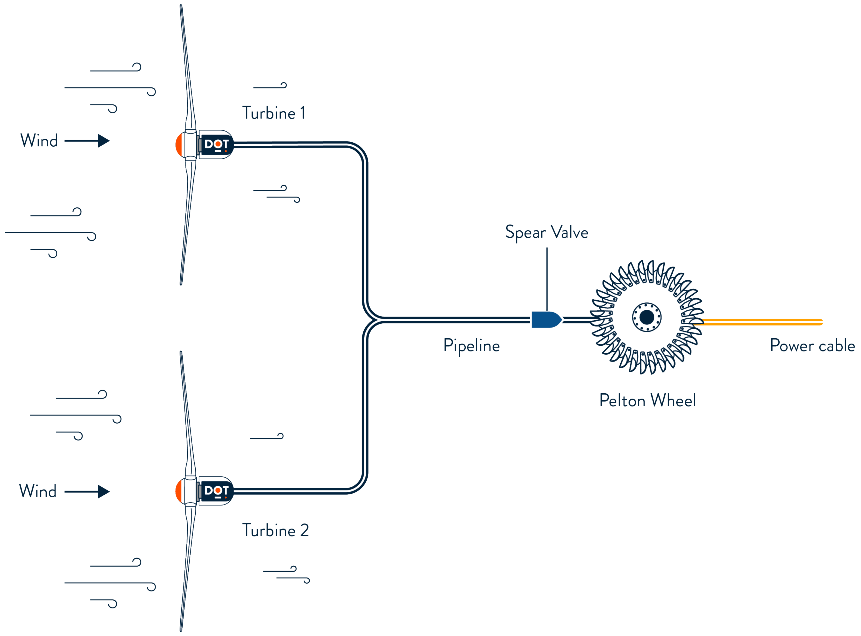

Figure 6-1: Parallel two-turbine HWF setup for the simulation study. It is assumed that there is no wake interaction between the two turbines.

the CEMPC framework and controlled system. Moreover, it shows how the controller reacts to instantaneous wind speed changes. Data from the Dutch Offshore Wind Atlas (DOWA) [77], suggest that the average offshore wind speed at 100 m height in Dutch wind farms roughly ranges between 8-12 m/s over the year. In this thesis, the performance of the controllers is investigated in a wind speed range of 7-18 m/s for a hub height of 90 m.

The other three wind cases contain 15-minute (900-second) turbulent below-rated, near-rated, and above-rated wind speed profiles with a mean of 8 m/s, 12 m/s, and 16 m/s, respectively. These wind cases are used to evaluate the performance when exposed to more realistic dynamic wind speed inputs. Two turbulent wind speed profiles are created for each of the aforementioned wind speed cases. The first wind speed profile is used as an input for the single-turbine case and the first turbine in the two-turbine case. The second wind speed profile is only used as an input for the second turbine in the two-turbine case.

The turbulent wind speed profiles are generated using the turbulent wind speed simulator TurbSim [37], created by NREL. A 15 by 15 grid-point matrix, representing a 145 m by 145 m grid, is used to simulate 1000 second wind speed profiles at 90 m hub height with a time step of 0.01 seconds. The first 100 seconds are used for initialization purposes. The International Electrotechnical Comission (IEC) Kaimal Normal Turbulence Model (NTM) is used, resulting in turbulence intensities of 24%, 19%, and 18%, corresponding to the below-rated, near-rated, and above-rated mean wind speeds, respectively.

The simulations are performed using the control diagrams shown in Figure 4-3 and Figure 5-1. The system model and CEMPC framework described in Section 2-6, Section 4-6, and Section 5-3 are simulated within a MATLAB Simulink environment. An immersion and invariance (I&I) wind speed estimator is employed to estimate the rotor-effective wind speed. The estimator gain is tuned such that the estimated wind speed converges fast, but stable. The plant model runs at a sample rate of 0.01 seconds and the CEMPC framework at 0.2 seconds. The second-order cone programming (SOCP) optimization problem is solved using MOSEK. As mentioned in the previous paragraph, the first 100 seconds of the turbulent wind cases are used for initialization purposes and are not shown in the results.

The electrical power generation of the HWTs will be compared with the results of employing idealized NREL 5-MW reference turbines. The assumption is made that the reference turbines are capable of obtaining maximum power coefficient values in below-rated regions, and perfectly track their rated power in above-rated regions. Accordingly, the following static equation describes the reference turbine power throughout the simulation:

$$P_{\mathrm{g,NREL}} = \min\left(\frac{1}{2}\rho_{\mathrm{a}} A C_{\mathrm{P,max}} \hat{v}^3 \eta_{\mathrm{g}}, 5 \times 10^6\right), \tag{6-1}$$

where $C_{\mathrm{P,max}}$ is the maximum power coefficient, $\hat{v}$ is the estimated wind speed, and η_{g} is the generator efficiency. The total generated electrical power of the HWF is compared to that of the reference turbines and expressed as η_{NREL}.

6-2 Optimization objective weight selection

Tuning the objective weights of the CEMPC optimization problem, shown in (4-48), is a nontrivial task. As mentioned in Section 4-5, the optimization variables are normalized to facilitate the tuning process. To compare the basic performance of a single and two-turbine controller, the optimization weights are considered equal for the two cases. The resulting weights are given by Table 6-1. Note that the normalized values of the tuned weights with respect to each other determine the actual contribution to the optimization objectives.

Table 6-1: Weights of the optimization problem that is solved by the implemented CEMPC framework. The first weight α_1 values the maximization objective of the collective power, α_2 the minimization of rotor power variations, α_3 the minimization of pump power variations, α_4 the minimization of the kinetic rotor energy state variations, α_5 the minimization of overspeeding, and α_6 represents the weight for the minimization of turnpike mitigation.

Tuned optimization weights

W	α_1	α_2	α_3	α_4	α_5	α_6
V	2	1	5	30	1	2

In the tuning process, it is seen that the weight on the power maximization objective, α_1, has a great influence on the maximum attained power coefficient in below-rated conditions. However, when making the weight too high, the controlled system shows aggressive and oscillatory behavior. Therefore, there is a tradeoff between power maximization and smooth system behavior.

The rate-limiting objectives for the rotor power, pump power, and rotor kinetic energy, respectively weighted by α_2 and α_3, determine the allowed speed in actuating the blade pitch angles, pump displacements, and indirectly the spear position. By tuning these weights, an attempt is made to compensate for the omitted actuator and hydraulic dynamics. Moreover, the acceleration of the rotor speed is reduced by increasing α_4. It is seen that limiting the kinetic rotor energy results in less excitation of the hydraulic dynamics and smoother power responses. Too high values for the aforementioned weights may result in undesired actuator interference, such as blade pitch control in below-rated regions and excessive pump displacement control in above-rated operation. The last two weights are tuned such that the controller prevents overspeeding and turnpike.

6-3 Wind case 1: Staircase throughout the operating regime

This section presents the adequacy of the novel HWF-CEMPC frameworks to control CDP- and DDP-HWFs throughout the entire operating wind speed regime. Figure 6-2 shows the employed wind speed signals and the corresponding I&I estimated values for the first and second wind turbines. The graphs clearly display the wind speed estimator delay, as the algorithm needs time to converge. The rated wind speed, denoted as the dashed line, is valued at 11.4 m/s. Note that for the single-turbine control case, only the first signal is used.

The results presented in this section show that the CEMPC framework is capable of controlling single-turbine and two-turbine HWTs. An effort is made to maximize the power capture in below-rated wind regions and to maintain the pump power at its rated conditions at above-rated conditions. This resembles the state-of-the-art control strategy described in Section 1-3. Note, however, that the controller has not been given any explicit information about different control strategies for different wind speed regions. It merely maximizes the objective function while considering the state and input constraints. Furthermore, the controller mitigates overspeeding. The following subsections discuss the results in more detail.

Note that the mechanical pump powers will be presented in the remainder of this chapter with a corresponding rated value of 5.3 MW.

6-3-1 Single-turbine control

This section first elaborates on the by the CEMPC envisioned performance, resulting from the internal control model responses, including the optimized powers and retrieved states and control inputs. Next, the measured HWF outputs will be discussed.

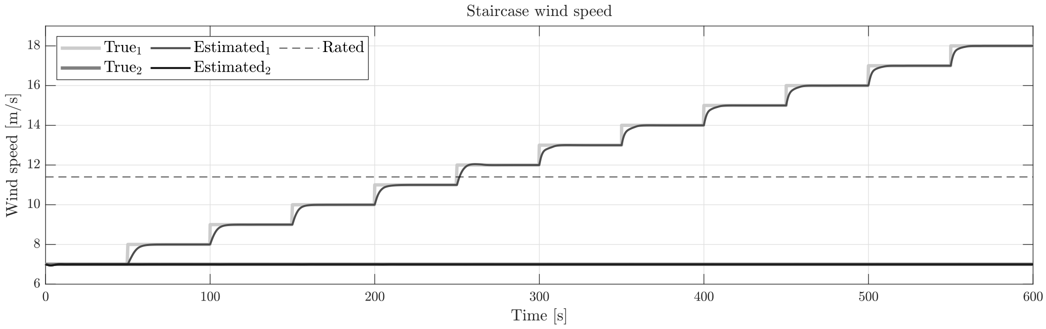

Figure 6-2: Hub height staircase wind speed signals for two wind turbines, covering the operational wind speed envelope. The true, I&I estimated, and rated wind speeds are depicted for two wind turbines. Note that the wind signal of the first turbine diverges, covering the wind envelope, where the second signal remains constant at 7 m/s.

CEMPC internal control model responses and resulting control inputs

Figure 6-3 shows the CEMPC optimized power responses, rotor states delivered by the internal control model. Moreover, the computed control inputs are presented. These results reveal the controller's intention on controlling the HWTs.

In below-rated regions, the controller's effort to maximize wind power extraction is visible in the power coefficient and tip-speed ratio (TSR) graphs. The controller steers the system towards the optimal TSR to maximize the power coefficient. The pump displacement and spear valve area are employed to obtain the desired pump torque. Note that in this operational area, the rotor speed is mainly regulated by controlling the pump torque, such that no useful energy is lost by pitching the blades.

It is found that the optimal TSR is not perfectly tracked at steady-state conditions. The tradeoff between the multiple control objectives, described in Section 6-2, certainly plays a significant role. Another possible contribution could be an error in the approximated available aerodynamic power, which is used as an upper bound in the optimization problem of the CEMPC (Section 3-2-2). A lower approximated aerodynamic power than the true value may pose a limitation on the maximum rotor speed, aerodynamic power, TSR, and power coefficient values. Finally, an increased pump pressure may lead to unattainable TSRs. This is further discussed later in this section.

When the rated pump power limit is reached, the controller starts actively regulating the blade pitch angles to keep the system within its constraints by rejecting excess aerodynamic power. The pump displacement is controlled towards its maximum value and the spear position converges. The latter varies slightly to preserve nominal nozzle pressure, but does not significantly contribute to rotor speed control. Pump displacements are used in above-rated conditions to mitigate transients induced by the instantaneous wind speed steps. Finally, note that the controller actively counters rotor overspeed.

Measured HWF responses

The results shown in Figure 6-4 present the measured HWT outputs as a result of the control inputs given by the CEMPC.

The differences between the measured plant outputs and the internal control model outputs are small, but slightly deviate. The measured aerodynamic rotor power response changes rapidly with the instantaneous step in wind speed, as it is directly affected. The convergence time of the I&I wind speed estimator results in a delayed aerodynamic power response in the internal control model. This results in lagged controller reaction and results in slower downstream power responses. Moreover, hydraulic network dynamics and actuator dynamics are not taken into account by the CEMPC framework. This may result in oscillatory behavior, rated pump power overshoots, and longer settling times.

Nevertheless, the controlled HWTs show satisfactory power maximization in below-rated regions and aerodynamic power rejection in above-rated regions. However, the controller

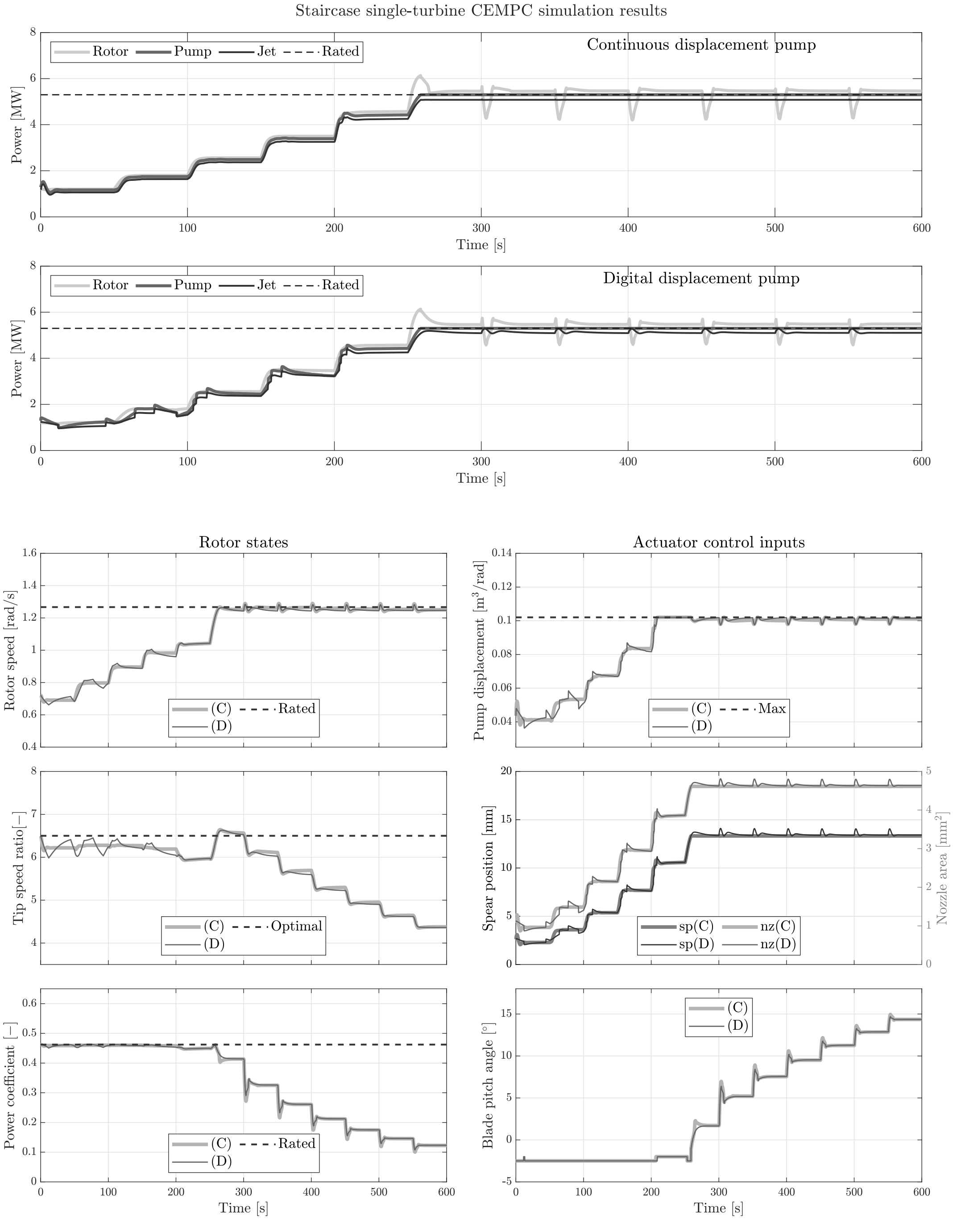

Figure 6-3: Staircase single-turbine CEMPC envisioned responses for the (C) and (D) cases. The upper plots show the power responses. The rotor states and actuator control inputs are shown in the lower matrix of plots. The transition from maximizing farm power to rejecting excess aerodynamic power is clearly visible in the power plots. Overspeed mitigation is notable, and the TSR graph shows that optimal TSR is not perfectly tracked.

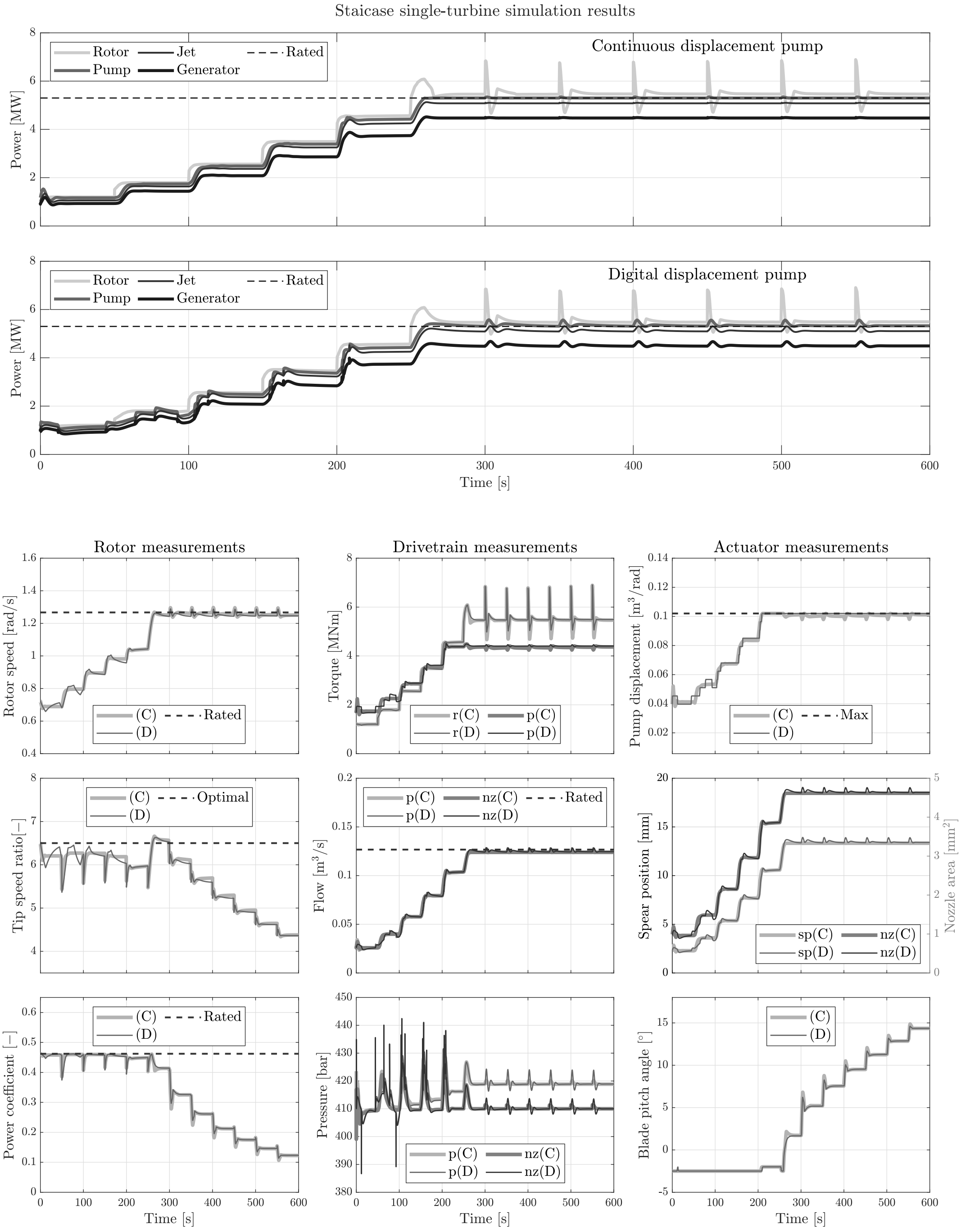

Figure 6-4: Staircase single-turbine measured (C) and (D) HWF outputs. The upper plots show the power responses. Rotor, drivetrain, and actuator measurements are shown in the lower plot matrix. The controller successfully controls the HWF throughout the operation window. Note that the (D) pump displacements switch near-instantaneously. Moreover, an increasing pressure offset and unmet rated pump conditions are visible.

framework does not perform adequately on keeping the nozzle pressure at the nominal value. The controller is capable of selecting the correct nozzle area values at steady-state conditions, but is unable to compensate for fast changes in pressure. This is visible in the pressure graph in Figure 6-4, which displays large deviations from the nominal value. A possible explanation could be the difference in execution rate of the control framework and the HWT plant model, and the, therefore, interpolated control inputs. Moreover, the mapping from the optimized convex CEMPC variables to the nozzle area required to maintain nominal nozzle pressure, in (3-43), is not perfect.

Power limiting system characteristics

When investigating the staircase results in Figure 6-4, several power limiting system characteristics were found. The following paragraphs elaborate on these problems.

At around 200 seconds, the power coefficient settles at a lower value than before, while rated pump power conditions are not attained yet. This is caused by the fact that the maximum pump displacement limit is reached. Therefore, the system converges on a suboptimal operation point where blade pitch control is necessary for below-rated conditions, and available useful wind power is not captured. This problem could be addressed by improving the pump design by increasing the maximum pump displacement.

A problem that can be seen in the pressure responses is the increasing offsets between pump and nozzle pressures. This phenomenon is caused by larger pressure losses due to increased friction at higher flows, explained in Section 2-3. An increase in pressure results in higher pump torques and -powers regarding the same flow. Considering the pump design and the corresponding power constraints (Section 4-5), the abovementioned phenomenon renders it impossible to operate at maximum pump displacement and rated rotor speed simultaneously when exposed to above-nominal pump pressures. Accordingly, the controller slightly reduces the rotor speed and the volumetric displacement to compensate for the increased pump pressures at rated pump conditions. This is clearly visible in the above-rated rotor speed and pump displacement responses of (C) in Figure 6-3.

This prevents the pumps to operate at rated conditions, leading to suboptimal flow production at rated pump power. As the jet power is defined as the product of the nozzle flow and the nozzle pressure, which is maintained at the nominal value, the maximum attainable jet power decreases for pump pressures above the nominal value. This is visible in the power responses in Figure 6-4, where the offset between pump and jet power increases. This effect could be mitigated by designing the pump for the increased pressure at rated conditions instead of the nominal pressure. Note, however, that this may lead to decreased pump efficiencies for lower flow operation.

Difference in employed pumps

When comparing the results of (C) and (D) in Figure 6-4, differences in controller behavior become visible. This is discussed in the following paragraphs.

From the power responses, it can be seen that the aerodynamic rotor power performances are similar. Larger differences are visible in the downstream power responses, as the near-instantaneous switching of the DDP pump displacement directly alters the pump flow, -torque, and -power. The combination of a rapid change in pump flow and spear position as a reaction, excite the hydraulic dynamics and induce large pressure and flow peaks, affecting the produced jet power. As this also affects the jet velocity, this results in less stable generator power outputs compared to the (C) case. It must be noted that the Pelton generator inertia and dynamics are not taken into account. In this study, the generator power changes instantly for a jet power and jet velocity change, whereas in reality the inertia of the Pelton runner will add damping and facilitate a more stable generator power response.

Note that the differences in the responses of (C) and (D) become smaller at rated conditions, where the pump displacement in (D) is retained at its maximum value. Still, the controller in (C) is more adequate in mitigating power oscillations, as it is capable of using small pump displacement variations. In the (D) case, the controller is unable to alter the digital pump displacements in near-rated conditions due to limited pump displacement availability and switching thresholds posed by the displacement selection algorithm. The controller is not compensating for the difference in the CEMPC calculated continuous displacement and the selected digital displacement. The applied blade pitch angles are based on the optimized aerodynamic power, without considering the effect of the abovementioned difference in the selected pump displacement. This allows the selection of controller input combinations leading to rated pump power crossing.

6-3-2 Two-turbine control

The previous section considered the control of a single HWT. This section will elaborate upon two-turbine HWF cases.

Figure 6-5 shows the outputs of a CEMPC controlled two-turbine HWF for the case where both turbines are exposed to the same wind speed signal. The controllers of the single- and two-turbine cases exhibit similar characteristics. Visible differences are that the jet power, generator power, and flows are roughly doubled by the addition of the extra wind turbine. Furthermore, the pressure offset at rated conditions is increased to a gap of almost 20 bar. Finally, the turbine outputs show more oscillatory behavior, due to the increased complexity of the control of the coupled system dynamics introduced by the drivetrain-sharing wind turbines.

In real-world scenarios, it is unlikely that two turbines experience equal wind speeds. Therefore, the abovementioned equal wind profile case will be compared with a situation where the wind turbines experience different wind speed signals.

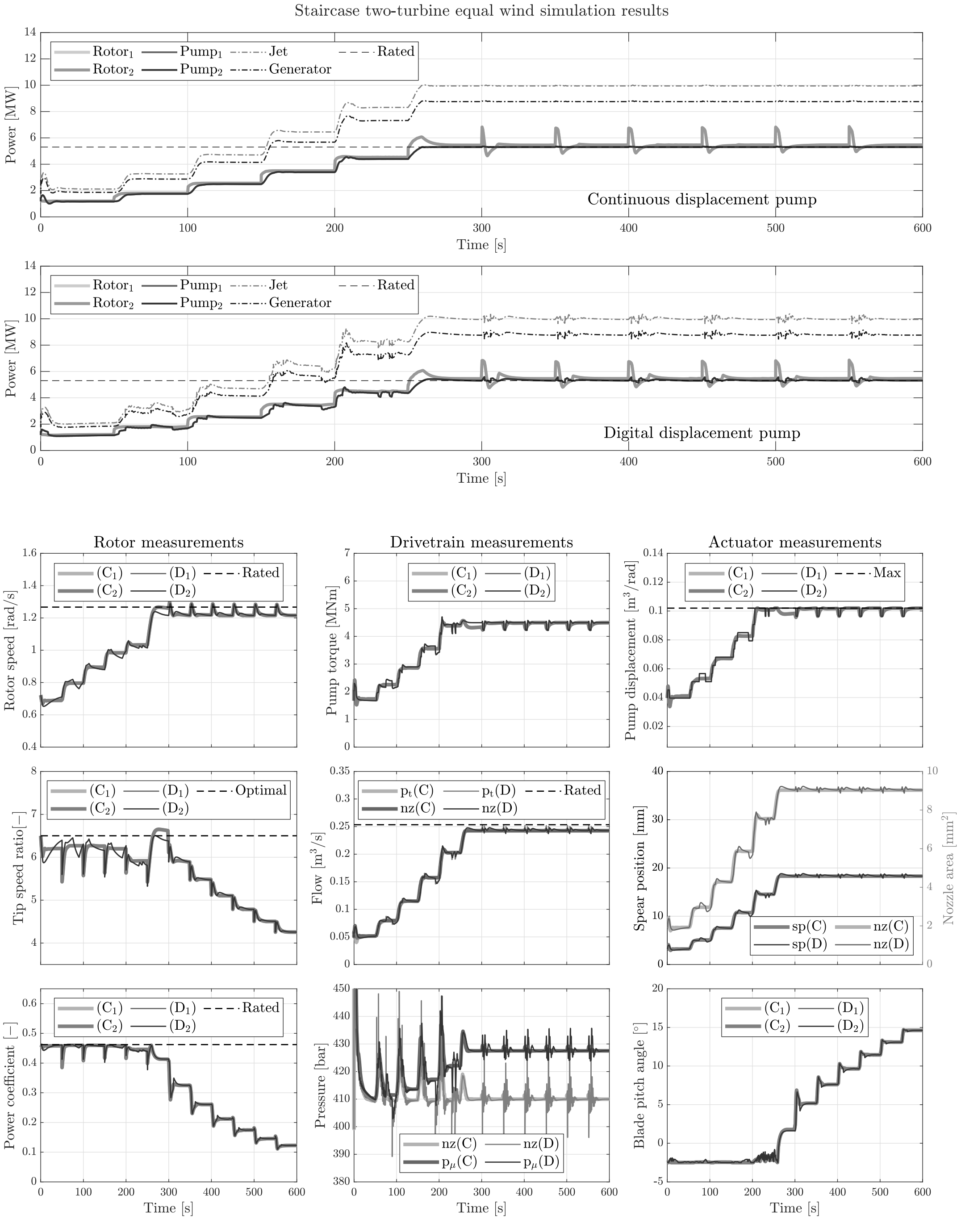

Figure 6-5: Staircase two-turbine HWF outputs for equal wind speed profiles. The combined pump flow is denoted as p_t and the mean pressure of the two pumps as p_μ. Note that the controller behavior is similar to the single-turbine case. The flow, jet power, and generator power are roughly doubled. Moreover, the pressure offset has increased to approximately 20 bar. Finally, increased oscillatory behavior due to dynamic coupling is visible.

Table 6-2: Comparison of single-turbine (ST) and two-turbine (TT) HWF performance for the equal wind and diverting wind cases. The energy generated by the two pumps and the total number is given, moreover, η denotes the efficiency of the two-turbine case with respect to the combined results from the two separate working single-turbine HWFs.

	E_{ptot} [kWh]	η_{p}	E_{jet} [kWh]	η_{jet}
Eq. wind (ST)	1352.2	-	1328.1	-
Eq. wind (TT)	1350.8	99.897%	1305.1	98.269%
Div. wind (ST)	852.69	-	840.45	-
Div. wind (TT)	851.47	99.857%	837.24	99.618%

Comparison between equal and diverting wind speed cases

Figure 6-2, presents the wind speed profiles perceived by the two wind turbines in the diverting wind speed case. The wind speed of the second wind turbine is maintained at 7 m/s while the staircase signal of the previous subsection is used for the first turbine. The resulting responses are visualized in Figure D-1 in Appendix D.

Table 6-2 displays pump power performances of single-turbine and two-turbine CDP-HWFs for equal- and diverting wind cases. In the single-turbine cases, two parallel working single-turbine HWFs are considered, having separate hydraulic drivetrains and spear valves. In the two-turbine cases, the two turbines share a hydraulic drivetrain and are controlled by the same spear valve. The efficiencies given in the table denote the efficiency of the two-turbine farm with respect to two single-turbine power plants.

In both wind cases, the two separate single-turbine power plants are capable of producing more combined pump and jet energy compared to the two-turbine farm. This can be allocated to the fact that in the two-turbine farm, the system is harder to control due to coupled dynamics. Furthermore, due to increased flow in the two-turbine case, larger friction losses are induced and thereby the jet power efficiency is decreased even more than the pump power efficiency.

It is noticeable that the pump energy efficiency is lower in the diverting wind case than in the equal wind case. This can be explained by the fact that the optimal pump pressure values of the individual wind turbines deviate for diverging wind speed signals. Since the spear position is used in an effort to maintain nominal nozzle pressure, obtaining the desired pump torque is dependent on regulating the pump pressures using pump displacements. Increased oscillatory pressure behavior is induced by the addition of the second wind turbine, which makes optimal pump pressure tracking more complex, especially when having limited pump displacement choice as in (D). It is expected that a two-turbine DDP-HWF would show significantly lower performances in this wind case.

The jet energy efficiency, however, is higher for the diverting wind case. The total network flow is lower than in the equal wind case due to lower wind speed values for the second turbine, resulting in fewer pipeline losses and higher drivetrain efficiency.

6-4 Wind case 2: Below-rated turbulent wind profile

Where in the previous section the steady-state performance of the controllers in different wind speed regions were analyzed, the following sections will focus on the performance for more realistic turbulent wind speed cases. This section elaborates on the performance of the controllers for the below-rated turbulent wind speed signals, shown in Figure 6-6. Note again that for the single-turbine control case, only the first signal is used.

Single-turbine control

The simulated power responses and plant measurements for the below-rated single-turbine case are shown in Figure 6-7. The obtained results are summarized in Table 6-3. Note that the values presented in this table are rounded to two significant digits for conciseness.

The behavior of the controlled system resembles the conventional turbine control strategy for below-rated wind speed conditions, as described in the previous wind case.

When comparing the results of the (C) and (D) cases in Figure 6-7 and Table 6-3 it can be concluded that the performance of both cases is similar. It must be noted that in the far digits, the (C) is capable to obtain higher power means with respect to (D). A visible difference is that the deviations in the (D) case are higher due to the instantaneous switching of pump displacements. This is also seen in the pressure response and eventually leads to a less stable generator power response.

Finally, 88% of the maximum attainable power (considering maximum pump and generator efficiencies) is extracted by the power plant. This corresponds to 84% of the energy that the NREL 5-MW turbine could produce for the given wind, assuming that the reference turbine is able to operate at the maximum power coefficient.

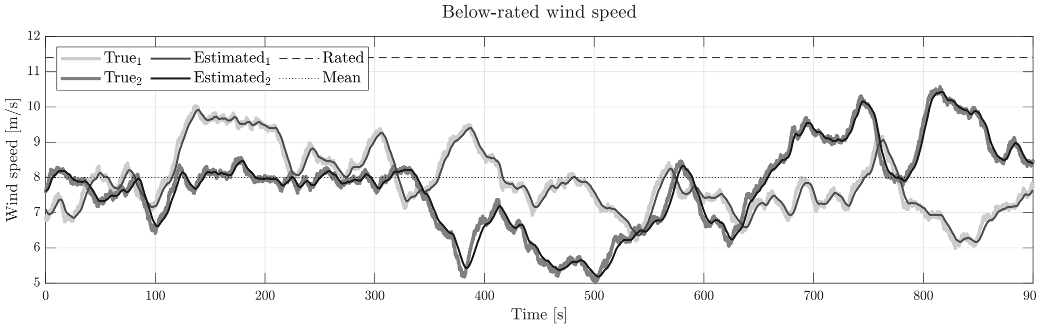

Figure 6-6: Hub height below-rated wind speed signals with an 8 m/s mean and a turbulence intensity of 24%. The true, I&I estimated, rated, and mean wind speeds are depicted for two wind turbines.

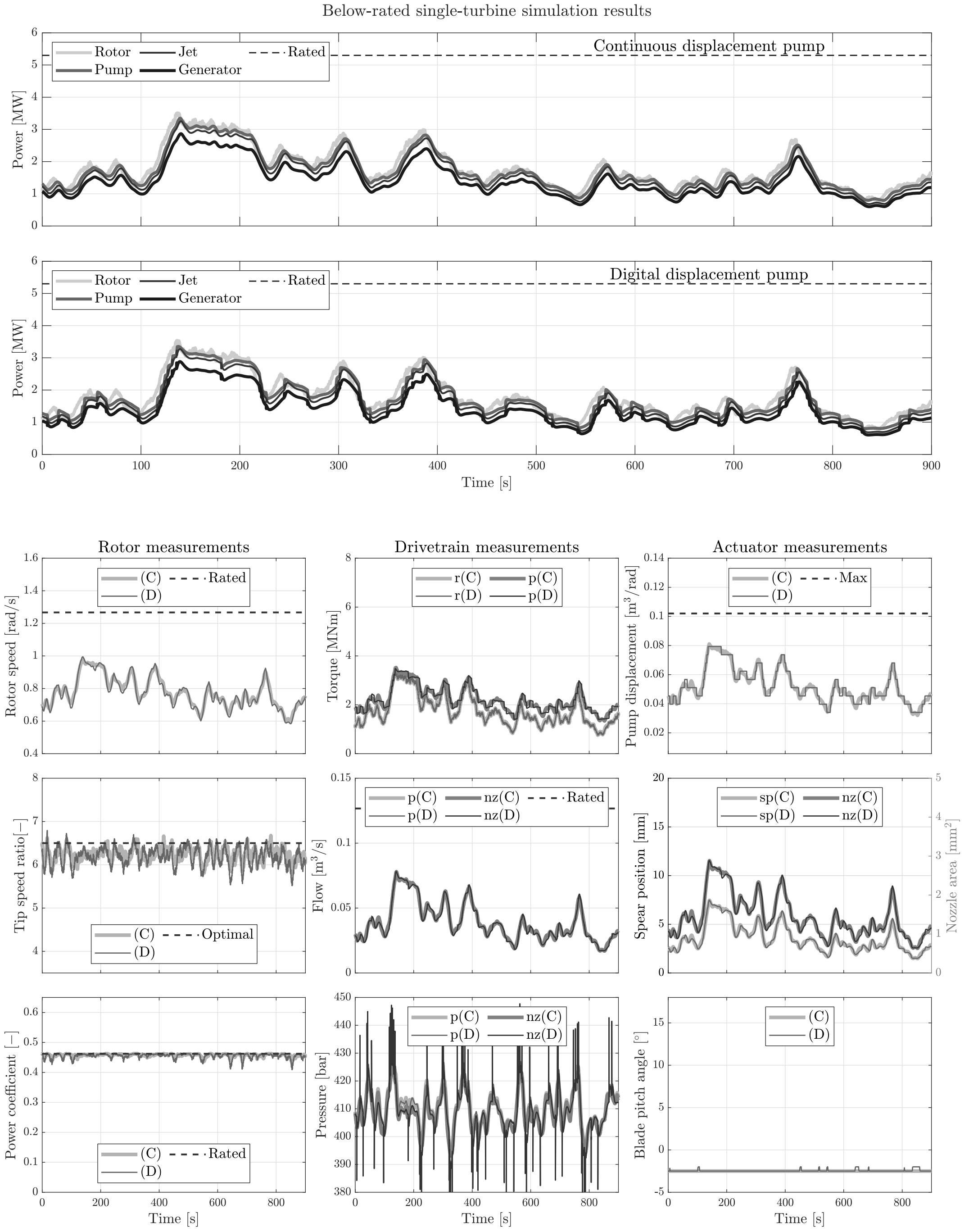

Figure 6-7: Below-rated single-turbine results for a turbulent wind profile. The upper plots show the power responses of the (C) and (D) cases. Note that the depicted pump power is the mechanical pump power. The plant measurements are presented in the lower plots. The power coefficient plot shows the controller's effort to maximize the wind power capture. Note that the nozzle pressure deviates from the nominal value.

Table 6-3: Dynamic single-turbine HWF performance of the CDP and DDP case at below-rated turbulent wind speeds. The mean μ and standard deviations σ and σ/μ of various parameters are presented. Total produced energies are given by E, the portion of this energy that is obtained by powers above the rated pump power constraint is given by E_O, and maximum overshoot percentage by P_O. Note that for below-rated conditions, there is no rated pump power overshoot. The efficiency with respect to the maximum attainable power, considering maximum pump and generator efficiencies, is described by η_max. The efficiency compared to NREL 5-MW reference turbines is denoted by η_NREL.

	(C)			(D)		
Turbine 1	μ	σ	σ/μ	μ	σ	σ/μ
Rotor power [MW]	1.8	0.62	35%	1.8	0.63	36%
Pump power [MW]	1.6	0.60	37%	1.6	0.61	38%
Jet power [MW]	1.6	0.60	37%	1.6	0.62	39%
Generator power [MW]	1.4	0.53	38%	1.4	0.54	39%
Power coefficient [-]	0.46	0.0041	0.89%	0.46	0.0082	1.8%
Pump efficiency [-]	0.91	0.084	9.2%	0.91	0.11	12%
Pipeline efficiency [-]	1.0	0.021	2.2%	1.0	0.032	3.2%
Pelton efficiency [-]	0.88	7.3×10^{-4}	0.083%	0.88	8.3×10^{-4}	0.094%
Pump pressure [bar]	410	6.6	1.6%	410	7.3	1.8%
Nozzle pressure [bar]	409	6.3	1.5%	409	7.1	1.7%
	E	E_O	P_O	E	E_O	P_O
Pump Energy [MWh]	0.40	0.0%	0.0%	0.40	0.0%	0.0%
	E	η_max	η_NREL	E	η_max	η_NREL
Electrical energy [MWh]	0.35	88%	84%	0.35	88%	84%

Two-turbine control

The simulated power responses and plant measurements for the below-rated two-turbine case are shown in Figure 6-8, and summarized in Table 6-4.

When comparing the results of the first turbine in Table 6-4 with the results of the single-turbine case in Table 6-3, it is seen in the far decimals that the average power coefficient value of the two-turbine case is lower than the single-turbine case. This means that the individual wind power capture performances decrease for the addition of wind turbines. Furthermore, the drivetrain efficiency decreases due to additional pressure loss induced by higher flows. A positive effect is increased damping, which results in a more stable nozzle pressure and more stable generator power outputs, seen by declined standard deviations.

It can be seen that the (D) case is slightly less efficient and produces less energy. This is induced by the negative effects induced by limited pump displacement settings and near-instantaneous switching of the pump displacements. Finally, it can be seen that the controller uses blade pitch control in below-rated regions to compensate for the coupled dynamics.

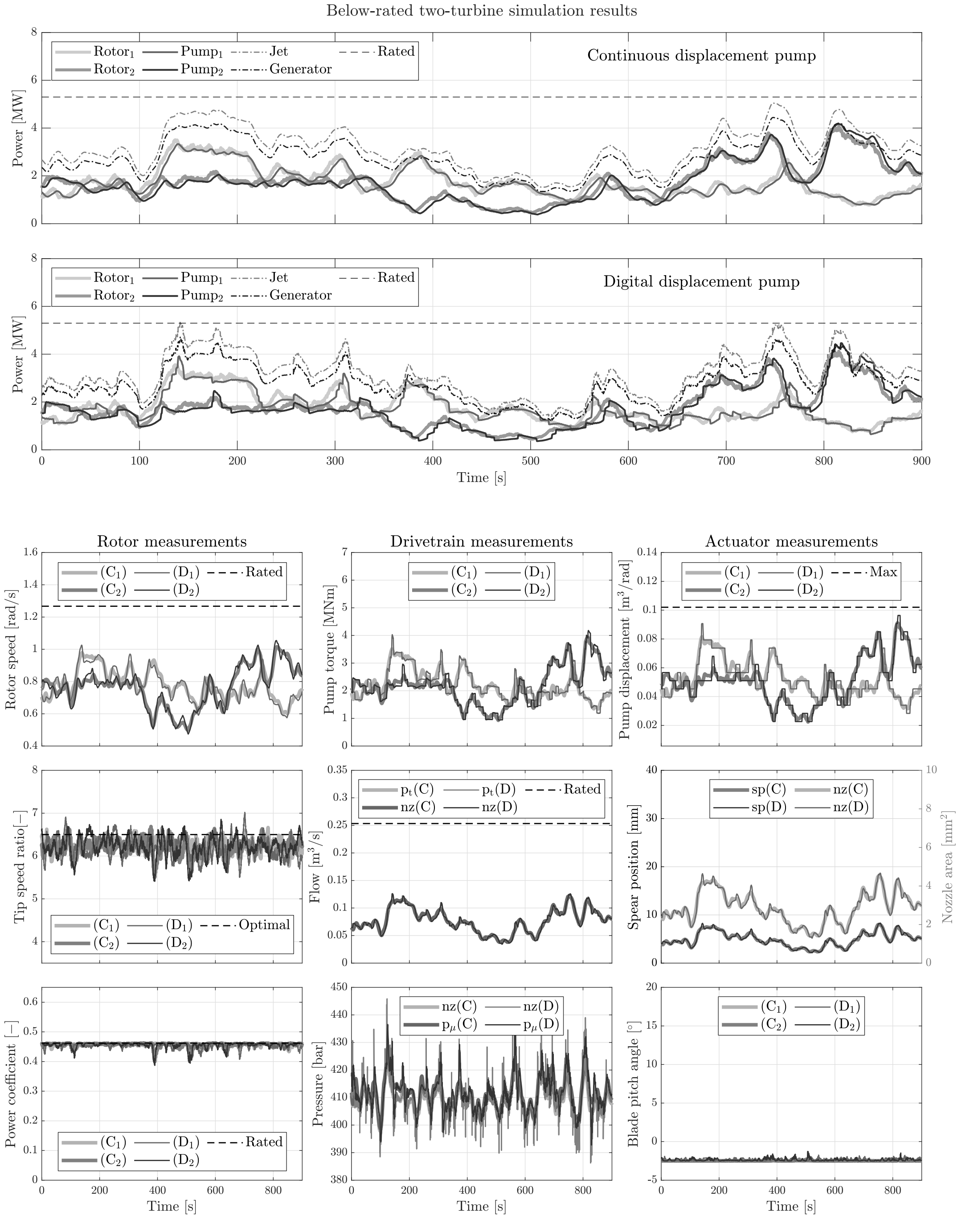

Figure 6-8: Below-rated turbulent two-turbine HWF outputs. The combined pump flow is denoted as p_t and the mean pressure of the two pumps as p_μ. Note that the flow, jet power, and generator power are increased. Moreover, the increased flow adds damping to the pressure response. Furthermore, increased oscillatory behavior due to dynamic coupling is visible. For this reason, blade pitch control is used in below-rated conditions.

Table 6-4: Dynamic two-turbine HWF performance of the CDP and DDP case at below-rated turbulent wind speeds. Note that the values are rounded to two significant digits for conciseness. The pipeline efficiency is decreased compared to the single-turbine case due to higher pressure losses. Nominal nozzle pressure tracking is improved due to added hydraulic damping, resulting in lower generator power deviations. Finally, it is notable that the (D) HWF is less efficient.

	(C)			(D)		
Turbine 1	μ	σ	σ/μ	μ	σ	σ/μ
Rotor power [MW]	1.8	0.62	35%	1.8	0.62	36%
Pump power [MW]	1.6	0.60	37%	1.6	0.62	39%
Power coefficient [-]	0.46	0.0041	0.90%	0.45	0.0079	1.7%
Pump efficiency [-]	0.91	0.084	9.3%	0.91	0.11	13%
Pump pressure [bar]	411	5.3	1.3%	411	6.4	1.6%
	E	E_{O}	P_{O}	E	E_{O}	P_{O}
Pump energy [MWh]	0.40	0.0%	0.0%	0.40	0.0%	0.0%
Turbine 2	μ	σ	σ/μ	μ	σ	σ/μ
Rotor power [MW]	1.7	0.80	46%	1.7	0.80	46%
Pump power [MW]	1.6	0.77	49%	1.6	0.78	50%
Power coefficient [-]	0.46	0.0067	1.5%	0.46	0.0099	2.2%
Pump efficiency [-]	0.90	0.098	11%	0.90	0.13	14%
Pump pressure [bar]	411	5.3	1.3%	412	6.5	1.6%
	E	E_{O}	P_{O}	E	E_{O}	P_{O}
Pump energy [MWh]	0.39	0.0%	0.0%	0.39	0.0%	0.0%
Collective	μ	σ	σ/μ	μ	σ	σ/μ
Jet power [MW]	3.2	0.89	28%	3.2	0.92	29%
Generator power [MW]	2.8	0.78	28%	2.8	0.81	29%
Pipeline efficiency [-]	0.99	0.013	1.3%	0.99	0.026	2.6%
Pelton efficiency [-]	0.88	5.4×10^{-4}	0.062%	0.88	6.7×10^{-4}	0.076%
Nozzle pressure [bar]	409	4.9	1.2%	409	6.1	1.5%
	E	η_{max}	η_{NREL}	E	η_{max}	η_{NREL}
Electrical energy [MWh]	0.7	88%	84%	0.69	88%	83%

6-5 Wind case 3: Near-rated turbulent wind profile

Inspecting the performance of the CEMPC framework at near-rated conditions is important, as the controller has to prevent the system from exceeding its design limits. Tuning a controller to switch smoothly between below- and above-rated operation is generally considered as a challenge. The performance and behavior of the proposed controller concepts are evaluated for near-rated wind signals with a 12 m/s mean, displayed in Figure 6-9. The two wind speed profiles are used as inputs for the first and second wind turbine, respectively.

The results show a smooth transition between maximizing power capture in below-rated conditions and excess aerodynamic power rejection in above-rated conditions. Small pump power overshoots are detected and mitigated by the controller.

Single-turbine control

The power responses, presented in Figure 6-10 show a smooth transition between power maximization and excess aerodynamic power rejection. However, in both cases (C) and (D), the rated pump power is occasionally exceeded, as can be seen in the portion of generated energy obtained by above-rated pump power (E_O) and power overshoot (P_O) percentages in Table 6-5. The modeling errors of the internal control model, induced by omitted system dynamics, contribute to rated pump power overshoots. In the (D) case, the rated power is crossed more often. This is explained by the limiting pump displacement variability and the lack of compensation for the effect of the difference in CEMPC optimized, and ultimately selected pump displacement, discussed in Section 6-3-1.

It can be seen that the standard deviations of the powers decrease as the powers are maintained more stable when the pump power reached its limit. The pump efficiencies

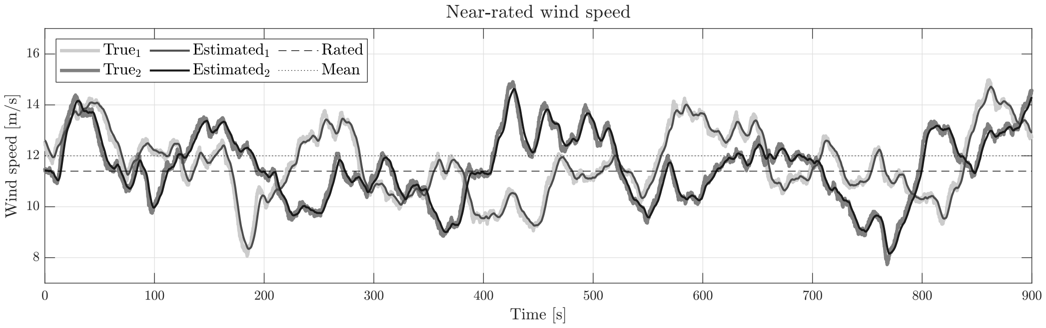

Figure 6-9: Hub height near-rated wind speed signals with a 12 m/s mean and 19% turbulence intensity. The true, I&I estimated, rated, and mean wind speeds are depicted for two wind turbines.

Table 6-5: Dynamic single-turbine HWF performance at near-rated turbulent wind speeds. Note that the pump efficiencies are increased, but pipeline efficiency is decreased compared to the below-rated results due to larger pressure loss at larger flows. This also leads to higher pump pressures. Nominal nozzle pressure tracking is improved due to added damping in the hydraulic network. Furthermore, it is clearly seen in E_O and P_O that the rated pump power is exceeded more often in the (D) case. Finally, it is seen by η_max and η_NREL that the overall plant efficiency is improved.

	(C)			(D)		
Turbine 1	μ	σ	σ/μ	μ	σ	σ/μ
Rotor power [MW]	4.9	0.90	18%	4.9	0.92	19%
Pump power [MW]	4.6	0.76	16%	4.6	0.80	17%
Jet power [MW]	4.5	0.75	16%	4.6	0.78	17%
Generator power [MW]	4.0	0.66	16%	4.0	0.69	17%
Power coefficient [-]	0.40	0.072	18%	0.41	0.07	17%
Pump efficiency [-]	0.95	0.092	9.7%	0.95	0.096	10%
Pipeline efficiency [-]	0.98	0.016	1.6%	0.98	0.019	1.9%
Pelton efficiency [-]	0.88	9.3×10^{-4}	0.11%	0.88	9.9×10^{-4}	0.11%
Pump pressure [bar]	417	7.6	1.8%	417	8.1	1.9%
Nozzle pressure [bar]	410	6.6	1.6%	410	7.2	1.8%
	E	E_O	P_O	E	E_O	P_O
Pump Energy [MWh]	1.2	0.04%	0.62%	1.2	0.66%	5.1%
	E	η_max	η_NREL	E	η_max	η_NREL
Electrical energy [MWh]	1.0	91%	88%	1.0	92%	89%

increase as the volumetric pump operates closer to its rated conditions, but pipeline efficiencies decrease due to friction induced by larger flows. This also results in increasing pump pressures. The nozzle pressure becomes better controllable as the pump displacement values deviate less in rated power conditions and therefore the hydraulic network is less excited. Finally, the η_max and η_NREL values show that the efficiency with respect to the maximum attainable performance and NREL 5-MW performance, respectively, is increased.

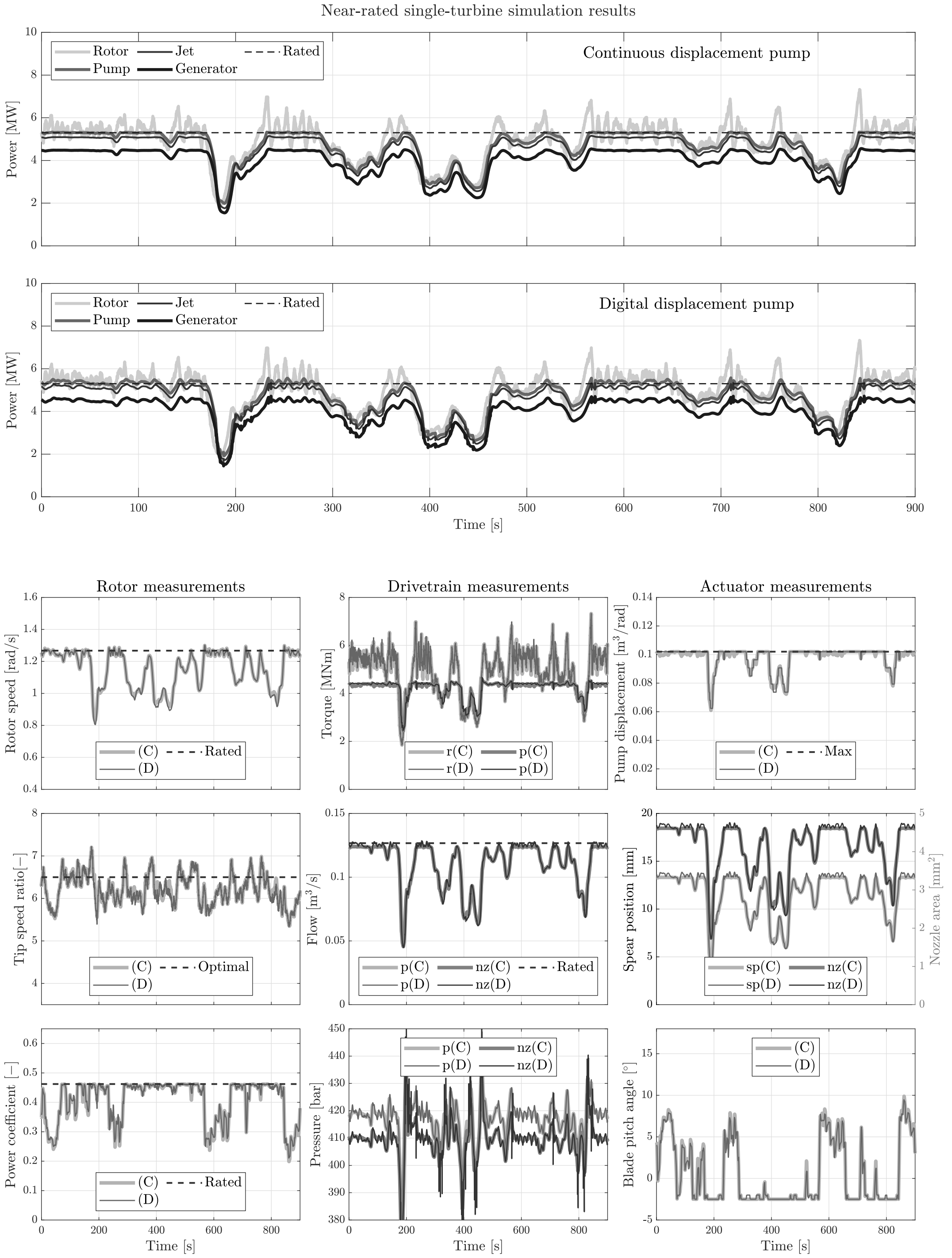

Figure 6-10: Near-rated single-turbine results for turbulent wind profiles. Note the switch from a power maximization objective at below-rated conditions and excess aerodynamic power rejection at above-rated conditions. The rated pump power is occasionally crossed.

Two-turbine control

The simulated power responses and plant measurements for the rated two-turbine case are shown in Figure 6-11, and summarized in Table 6-6. Comparing the obtained rated two-turbine results with the single-turbine results, similar differences are seen as described in the below-rated two-turbine turbulent wind case. Note, however, that the occurrence of overspeeding and overshoot is increased due to a more complex control problem due to the coupled dynamics of the wind farm.

Table 6-6: Dynamic two-turbine HWF performance of the (C) and (D) cases at near-rated turbulent wind speed profiles. Similar differences are found between single-turbine and two-turbine control, as described in the previous subsection and previous wind profile cases. Note that pump power overshoot values E_O and P_O of turbine 1 are higher due to increased control complexity of the coupled dynamics of the two-turbine system.

	(C)			(D)		
Turbine 1	μ	σ	σ/μ	μ	σ	σ/μ
Rotor power [MW]	4.9	0.91	19%	4.9	0.93	19%
Pump power [MW]	4.6	0.77	17%	4.6	0.80	17%
Power coefficient [-]	0.40	0.073	18%	0.40	0.072	18%
Pump efficiency [-]	0.95	0.093	9.7%	0.95	0.099	10%
Pump pressure [bar]	424	5.5	1.3%	424	6.2	1.5%
	E	E_O	P_O	E	E_O	P_O
Pump energy [MWh]	1.2	0.044%	0.69%	1.2	0.56%	6.2%
Turbine 2	μ	σ	σ/μ	μ	σ	σ/μ
Rotor power [MW]	4.8	1	21%	4.8	1.0	21%
Pump power [MW]	4.5	0.88	19%	4.5	0.91	20%
Power coefficient [-]	0.41	0.068	17%	0.41	0.067	16%
Pump efficiency [-]	0.95	0.088	9.2%	0.95	0.097	10%
Pump pressure [bar]	424	5.6	1.3%	424	6.3	1.5%
	E	E_O	P_O	E	E_O	P_O
Pump energy [MWh]	1.1	0.055%	0.87%	1.1	0.58%	6.2%
Collective	μ	σ	σ/μ	μ	σ	σ/μ
Jet power [MW]	8.8	1.0	12%	8.8	1	12%
Generator power [MW]	7.8	0.90	12%	7.8	0.92	12%
Pipeline efficiency [-]	0.97	0.0089	0.93%	0.97	0.014	1.4%
Pelton efficiency [-]	0.88	4.6×10^{-4}	0.052%	0.88	5.3×10^{-4}	0.061%
Nozzle pressure [bar]	410	4.0	0.97%	410	4.7	1.2%
	E	η_max	η_NREL	E	η_max	η_NREL
Electrical energy [MWh]	1.9	90%	87%	1.9	90%	87%

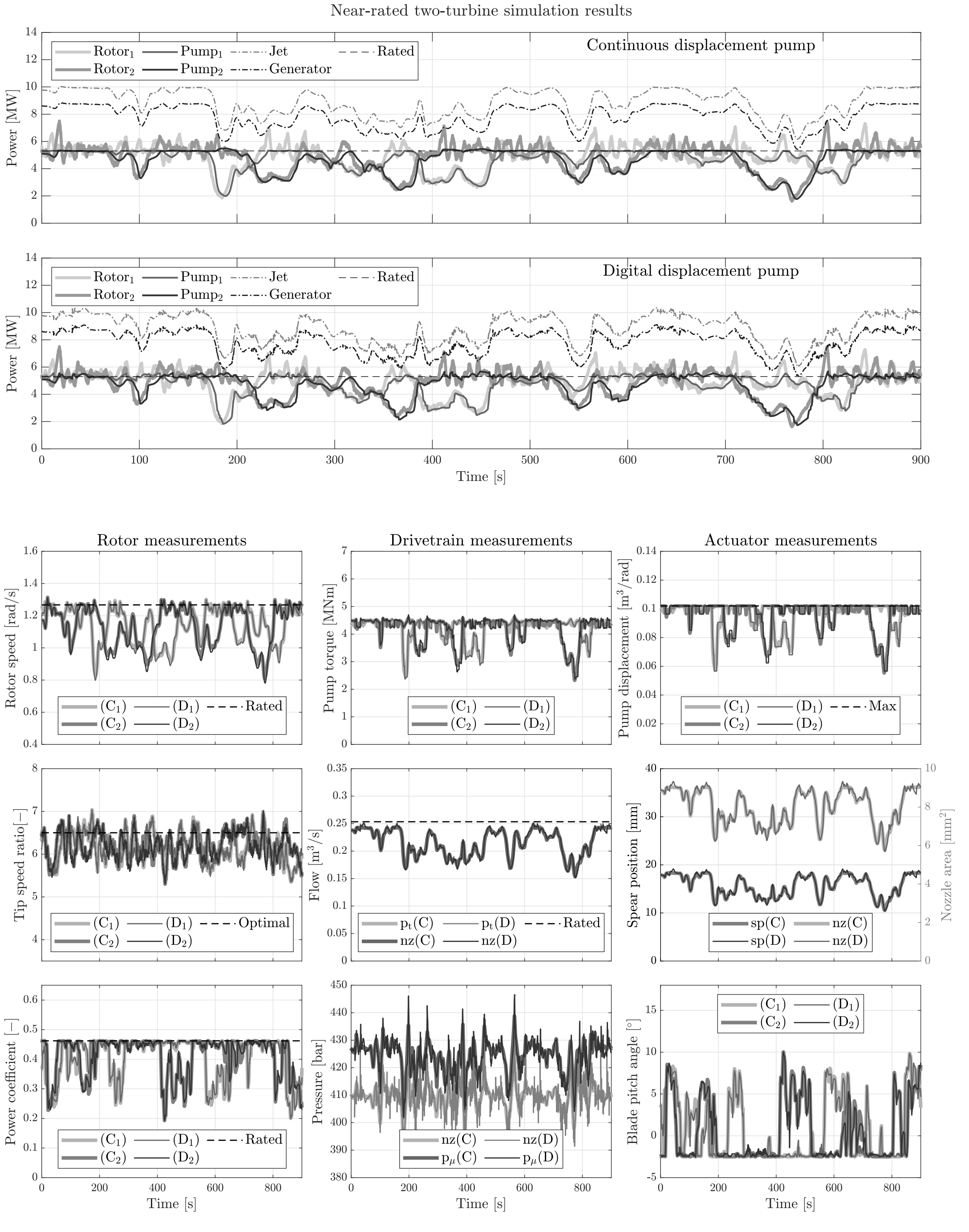

Figure 6-11: Near-rated two-turbine results for turbulent wind profiles. Similar controller behavior is visible as in the single-turbine case and as described in the previous wind cases. An increased occurrence of overspeeding and overshoot is notable, as the turbine operates close to its limits more frequently.

6-6 Wind case 4: Above-rated turbulent wind profile

A similar analysis as the below- and near-rated wind speed cases has been performed for above-rated wind conditions. However, for reasons of conciseness, these simulation results are included in Appendix D. Similar results have been found as described for the above-rated regions in the near-rated turbulent wind cases. However, oscillatory behavior in the power responses increases as the controller rejects excess aerodynamic power more aggressively to prevent overspeeding and rated pump power overshoot at higher wind speeds. For this reason, the rate and intensity of the use of the pump displacement in above-rated conditions rises. Finally, higher and more frequent rated power overshoots occur.

6-7 Yearly electrical energy generation estimation

A comparison with the yearly energy generation of CDP-HWFs and conventional NREL 5-MW wind turbines is presented in this section.

Wind speed data from DOWA [77] suggests that the yearly mean wind speed at the Noorden Waddeneilanden wind farm zone (2008-2017) has been roughly 10 m/s. Therefore, the potential of the different wind turbine concepts have been examined for a 10 m/s steady-state wind speed.

When assuming that the conventional wind turbines can be precisely controlled at optimal TSR and have a generator efficiency of 94.4%, the yearly generated electrical energy of a single turbine is equal to 29.19 GWh. This is enough to provide 10576 Dutch households (in 2020) with electricity [11].

When performing a 10-minute (600 second) simulation of a single-turbine HWT for the 10 m/s steady-state wind speed case, a generated electrical power of 477.04 kWh is obtained. When extrapolating this to a yearly generation, a value of 25.07 GWh is found, enough to supply 9083 households with electricity. The efficiency of the HWT is 85.90% with respect to the reference turbine.

For a two-turbine HWF, the yearly electricity generation is 49.71 GWh. Normalized with respect to the number of wind turbines, this value becomes 24.85 GWh (9003 households) per wind turbine, which is 85.14% with respect to the reference turbine.

The difference in generated energy between the conventional- and hydraulic-drivetrain concept wind turbines in the single- and two-turbine case (4.12 GWh and 4.34 GWh) would have been enough to power, respectively, 1492 and 1572 extra households per wind turbine. To conclude, the efficiency has dropped by 0.88% by adding a second HWT in the wind farm.

6-8 Concluding remarks

From the conducted simulation study, it can be concluded that the proposed scalable CEMPC framework is capable of controlling single-turbine and two-turbine CDP-HWFs. Moreover, the displacement selector algorithm can be used to extend this framework to the domain of DDP-HWFs. Real-time solving of both the system model and CEMPC framework is achieved in both single-turbine and two-turbine cases.

It is found that the controller framework maximizes the power production for below-rated conditions using spear position- and pump displacement-based pump torque control. In the two-turbine cases, blade pitch control is employed in this operational region to compensate for coupled turbine dynamics. The optimal TSR and hence the maximum power coefficient are not reached, which could be explained by the inclusion of other optimization objectives than power maximization. Moreover, errors in available aerodynamic power approximation could contribute to lower attainable rotor power, -speed, TSR, and power coefficient. More tuning efforts and a more accurate aerodynamic power approximation could further improve the controller performance.

In above-rated conditions, the controllers reject excess rotor power to keep the mechanical pump power close to its rated value. It is found that due to modeling errors in the internal control model of the CEMPC optimization problem, the rated power is occasionally exceeded, but the overshoot remains low.

The controller framework is capable of determining the correct spear position to maintain nominal nozzle pressure for steady-state conditions, but is unable to compensate for rapid pressure transients. Additionally, current pump displacement design prevents the system to operate optimally in near-rated conditions. Furthermore, larger network flows induce increased pressure loss, which results in an offset between the nozzle and pump pressures. This gives rise to decreased drivetrain efficiencies, but the increased pump pressures also restrict the pumps to produce rated pump flows, which results in decreased maximum attainable jet power. This shows that there is some room for pump design improvements to address these problems.

The main difference between the performance of CDP and DDP HWFs is the reduced DDP torque controllability due to the discrete set of realizable pump displacement values. This results in the fact that the required pump torque for maximum power capture can often not be realized. Therefore, the maximum achievable rotor performances and hence plant power generation are typically lower for this type of HWFs. Moreover, the near-instantaneous switching in below-rated conditions induces pressure and flow peaks in the hydraulic network, making the generator response less smooth than in the CDP cases. It must be noted that the inertia and dynamics of the Pelton generator are not taken into account in this study. Finally, whereas the pump displacement can be used in above-rated conditions to mitigate negative effects in CDP-HWTs, DDP-HWTs have a finite set of pump displacements and frequent switching is prevented by the displacement selector algorithm. Thereby, DDP-HWTs have less controllability to mitigate negative effects. Finally, the difference in the CEMPC optimized continuous pump displacement value and the ultimately by the displacement selector algorithm selected digital pump displacement setting is not compensated by any means, resulting in reduced controller performance.

The main differences between single-turbine and two-turbine performances are the slightly reduced control performances due to increased control complexity introduced by the coupled system dynamics. This causes problems with obtaining the required torque for acquiring the optimal tip speed ratio. Furthermore, larger offsets between the nozzle and pump pressures appear due to the increased network flow, leading to decreased wind farm efficiency. On a positive note, the increase in flow also adds damping to the flow and pressure responses, which results in lower pressure peak amplitudes and transients, improving nominal nozzle pressure tracking.

The efficiency with respect to the maximum attainable energy varies between 87%-92% in the turbulent wind cases. Moreover, the controlled HWFs generate between 83%-90% of the energy that could be generated by ideally operating NREL 5-MW wind turbines. Finally, the HWF concept is able to supply the yearly electrical power for roughly 9080 households per wind turbine with a decrease of 0.88% by adding the second wind turbine.

Chapter 7

Conclusions and Recommendations

7-1 Conclusions

This master thesis aims to provide a novel optimization-based controller framework for maximizing the centralized power generation of hydraulic-drivetrain wind farms (HWFs) that is yet absent within the existing literature. The convex economic model predictive control (CEMPC) framework for conventional wind turbines appears promising, but in its existing form, it is not applicable for the domain of HWFs. For this reason, the following goal was posed in the Introduction of this thesis:

Thesis goal: Develop a CEMPC framework, maximizing the overall power generation of individual hydraulic wind turbines and multi-turbine hydraulic wind farms.

The contributions of this thesis aim to stimulate advancements in wind turbine technology and facilitate the development of next-generation wind turbines, with the ultimate goal of lowering the cost of wind energy. To fulfill this goal, the (dynamical) modeling and control of HWFs and the state-of-the-art CEMPC methods in wind turbine control were further explored in this thesis. As a result, the existing CEMPC framework for conventional wind turbines is adapted to be compliant to the domain of HWFs, which is regarded as a novel contribution. Another novelty of the proposed framework is its scalability for the control of multiple hydraulic-drivetrain wind turbines (HWTs). With respect to state-of-the-art HWF control, the proposed CEMPC framework provides an optimization-based control method for the control of continuously variable displacement pump (CDP)-based HWFs. The framework is able to compute control actions for all wind turbines such that the overall plant power is maximized. Finally, an additional algorithm is proposed to extend the applicability of this framework to the domain of digital displacement pump (DDP)-HWTs. According to the sub-questions stated in the Introduction, the conclusions on the different parts of this thesis are presented next:

A simulation study is conducted as a proof of concept. Therefore, an adequate simulation model was key for the evaluation of the proposed controller framework. Moreover, the development of a CEMPC compliant internal control model was necessary. For these reasons, the first research question proposed in this thesis was:

I: How to develop an adequate, turbine scalable hydraulic-drivetrain wind farm simulation model for evaluation purposes, and how can this model be modified for the use as an internal control model in the CEMPC framework?

The nonlinear rotor dynamics and aerodynamic power capture of HWTs can be described by the well-known actuator disk model. Static hydraulic pump relations are employed in combination with varying pump efficiency terms. A linear parameter-varying (LPV) state-space method is utilized to capture the nonlinear hydraulic network dynamics. The model simulates water hammering effects and pressure losses due to increased flow. Simulations show that there are cut-in flow conditions. Flow beneath this point results in unstable dynamical behavior. To model the nozzle and fixed-speed Pelton generator, static relations are applied. Finally, the dynamics of spear position, blade pitch angle, and pump displacement actuators are included using simple first-order actuator models. Regarding the CEMPC internal control model, the hydraulic- and actuator dynamics are omitted to be able to conform to the requirements of the convex optimization problem.

Due to differences in working principles, control variables, and system constraints of the conventional and hydraulic-drivetrain wind turbine concepts, the currently established CEMPC frameworks in literature are not applicable for HWFs, therefore the following research question was formulated:

II: How is the existing CEMPC framework for conventional turbines altered for the control of single-turbine and multi-turbine hydraulic-drivetrain wind farms?

In this thesis, the existing framework for conventional wind turbines is adapted for the domain of HWTs. Additionally, the ability to control multiple turbines in a HWF is provided. Modifications that have been performed include the development of a simplified convex, and turbine scalable, internal predictive control model. Moreover, a formulation of the volumetric pump efficiency as a function of the convex variables, plant measurements, and feedback objectives are employed. Furthermore, a constraint is implemented to maintain the system within stable flow conditions. Finally, rate-limiting objectives for the CEMPC predicted states and control inputs are included as an attempt to compensate for system delays.

When controlling HWTs containing a DDP, the choice of pump displacements is limited to a finite set of realizable settings. The limited pump displacement selection range has consequences for wind turbine and wind farm performances. Moreover, the control challenge arises on how to identify and select the desired available pump settings. To this extent, the following research question is formulated:

III: How can the control of digital displacement pumps be incorporated within the in **II** developed CEMPC framework? And how does the performance differ when controlling turbines containing continuously variable displacement pumps and digital displacement pumps?

A supplementary pump displacement selection algorithm is included in the established controller framework to select the most suited available pump displacement setting of the DDPs. The selection algorithm prevents excessive switching by employing several switching logics. When comparing the performance of HWFs containing CDPs and DDPs, the performance of the two turbine concepts is similar. However, the latter comprises limited pump torque controllability due to the discrete set of realizable pump displacement values as the desired pump torque can, in most occasions, not be adopted. Additionally, whereas the pump displacement can be used in above-rated conditions to mitigate negative effects in the CDP case, this is typically not possible in the DDP case due to the limited amount of digital displacement settings and the switching limiting switching logics of the selection algorithm. Moreover, less smooth generator responses are acquired due to pressure and flow peaks in the hydraulic network, induced by the near-instantaneous displacement switching.

Successful real-time application of the CEMPC framework for single-turbine and two-turbine HWFs is demonstrated in a simulation study. The established controller framework aims to maximize the centralized power production using pump torque control in below-rated conditions by regulating the spear position and pump displacements. Furthermore, it rejects excess wind power using blade pitch control in above-rated conditions to maintain rated mechanical pump power. Thereby, the first part of the following subquestion is answered:

IV: Is the established CEMPC framework, capable of adequately controlling both single hydraulic-drivetrain wind turbines and multi-turbine hydraulic-drivetrain wind farms? How does the overall power generation performance change when extending towards a multi-turbine wind farm, and what is the performance compared to conventional wind turbines?

The addition of an extra wind turbine to a single-turbine HWF leads to attenuated individual rotor controllability due to coupled rotor and drivetrain dynamics. Moreover, increased pressure losses are induced by the larger flow of the two wind turbines. This results in reduced collective generator power production. It is shown that the yearly electrical energy generation drops by 0.88% when adding the second wind turbine.

The considered HWTs are capable of generating roughly 25 GWh a year, enough to supply about 9080 Dutch households. The power generation efficiency of the HWT concept with respect to NREL 5-MW reference turbines ranges between 83%-90%. To reduce the levelized cost of energy, the hydraulic-drivetrain wind farm concept has to provide at least an equivalent cost reduction over the lifetime of the wind farm. The scalability in number of controlled turbines of the CEMPC framework could be promising in realizing this cost reduction.

7-2 Recommendations for future work

This work has presented advances for a computationally tractable, in turbine scalable, optimization-based control method for hydraulic-drivetrain wind turbines. In the course of the research, potential interesting opportunities for further improvements, extensions, and applications for future work were identified. These recommendations are presented in this section, which is divided into two subsections. The first subsection summarizes recommendations regarding improvements that could be included in the proposed CEMPC framework, whereas the second subsection elaborates on potential interesting extensions and applications of the proposed controller framework.

Recommended improvements for the proposed controller framework

1. The strength of the HWF concept is that by using a shared hydraulic drivetrain, the construction and maintenance costs can be reduced. The larger the number of employed wind turbines sharing the same drivetrain, the more cost-efficient the wind farm will become (in terms of construction and maintenance). The performance of the established CEMPC framework is evaluated for a single-turbine and two-turbine wind farm. It is recommended to investigate the performance of controlling larger wind farms.

2. The results of this thesis show that there is room for improvement in the design of the HWF system. It is recommended to improve the pump design by increasing the maximum pump displacement. Moreover, a thorough investigation of the pipeline dimensions and hydraulic characteristics would be valuable to reduce the pressure loss throughout the system. These improvements may increase the power potential of the controlled hydraulic-drivetrain wind farms.

3. The obtained results indicate that the power is not maximized as effectively as physically possible in below-rated conditions. Moreover, in above-rated conditions, the rated pump power is exceeded while this has been constrained in the optimization program. More extensive tuning efforts could improve the results of the proposed method. However, part of these negative results can be allocated to modeling errors within the convex system representation and constraints in the CEMPC optimization problem. Several recommendations could be made:

    (a) The piecewise-linear approximation of the available aerodynamic power, which is used as an upper bound of the aerodynamic rotor power variable in the optimization problem, regularly leads to a lower estimate of the maximum power with respect to the true available power. This results in the fact that the maximum true aerodynamic power can not be attained. To minimize this error, one could use a piecewise-linear aerodynamic power approximation that makes use of more affine segments. Moreover, there are other, more accurate methods to approximate the aerodynamic power [31].

   (b) To consider the nonlinear hydraulic network dynamics in the optimization process, the inclusion of the LPV model into the internal control model should be investigated. As the model uses linear relations, this might be possible. The inputs of the model should be described by available optimization variables, and the overall system dynamics should stay linear and the constraints convex. The addition of hydraulic dynamics might enable the explicit description and optimization of the nozzle pressure or the spear position in the convex internal model to effectively maintain nominal nozzle pressure.

   (c) The incorporated rate-limiting constraints of the aerodynamic power, pump power, and kinetic rotor energy were introduced in this study as an attempt to compensate for the omitted actuator dynamics. It would be more effective if methods could be added that compensate for the actuator dynamics more accurately. This requires additional and transformed aerodynamic power constraints and additional optimization variables and objectives [18]. The addition of the network dynamics and an explicit optimization variable for the spear position, described in the previous item, will make the addition of spear actuator dynamics easier.

   (d) The employed simulation model and internal control model of the system are based on simplified dynamics. In reality, the dynamics of wind turbines and hydraulic systems are more complex. Therefore, the obtained controller performances and internal control model accuracy may not be representative for controlling a real-life HWF. For this reason, it is recommended to develop a high-fidelity plant model to evaluate the proposed CEMPC framework. A possible outcome could be that the framework does not perform as well as in this thesis. This calls for the development of a more accurate (first-principle) internal control model.

   Model-based or model-free adaptive methods in the internal control model could be useful tools to make the CEMPC framework more suitable for real-life application, e.g., by employing adaptive estimated parameters or a parallel Gaussian process to compensate for nonlinear dynamics that are not captured by the internal model, respectively. Besides minimizing the error between the internal control model and the controlled real-life system such that the power maximization objective could be better performed, the adoption of an adaptive model may also enable the capture of efficiency deterioration due to external factors or age and wear. In this light, the development of an adaptive convex internal control model is recommended.

4. To improve nominal nozzle pressure tracking, a feedback with feedforward compensation (FB-FFC) control scheme can be employed [8]. The CEMPC can be used to calculate the required nozzle area based on the optimized controller inputs, while an additional simple feedback loop is applied to compensate for smaller and fast pressure changes in the system to trim the nozzle pressure to the nominal value. A proof of concept is given in Appendix E, but needs to be further developed.

5. No measurement noise and dynamics were assumed in this work. To make the results more realistic, sensor models, considering the noise and dynamic characteristics of the different measurement instruments, should be included. Moreover, one sampling time step is assumed as control delay. A more thorough investigation into the communication system in wind turbines should be performed to consider realistic control delay values.

6. To further improve the computational tractability of the control framework, the optimization problem could be written as a quadratic programming problem. This type of optimization problem is intrinsically easier than second-order cone programming optimization problems and therefore faster to solve using existing highly efficient optimizers. A quadratic programming (QP) problem demands a convex, quadratic objective function and a set of linear equality and inequality constraints [15]. Hence, modifications are necessary to conform to the abovementioned requirements [18].

7. With regard to the control of the DDP-HWTs, the proposed control framework does not consider the hybrid nature of the digital displacement pump in the optimization problem. Therefore, the executed control variables are typically not optimal. Even worse, the difference between the optimized continuous pump displacement and the ultimately selected digital pump displacement is not counterbalanced by any means. For this reason, it is recommended to investigate the applicability of hybrid optimization methods like mixed-integer programming, and the development of a mixed-integer convex economic model predictive control (MICEMPC) framework for DDP-HWF. If the research is not fruitful, pressure or rotor speed compensation should be investigated for the rectification of the aforementioned displacement error.

Potential HWF-CEMPC framework extensions

1. The controller framework in this thesis is designed for the objective of overall farm power maximization. However, in the state-of-the-art literature about the CEMPC framework for conventional wind turbines, more extensions and objectives are applied, such as load mitigation [18, 57], the use of individual pitch control (IPC) [18], and power smoothing using a complementary energy storage device [57]. Moreover, the author in [60] introduces a LIDAR-assisted CEMPC method and an adaptive parameter to search for the true optimal tip-speed ratio during wind turbine operation. The inclusion of wind previewing could substantially improve the CEMPC predictions and optimized control inputs. Future wind speeds could be provided by LIDAR measurements [56]. Also, the development of a predictive wake model to enable wind previewing would be interesting. The CEMPC framework for HWFs proposed in this thesis is suited for the abovementioned extensions.

2. The increasing amount of renewable energy sources connected to the grid also gives rise to challenges. Their power outputs are often fluctuating and uncertain. This reduces the stability of the grid and increases utility grid power balancing costs. Authorities have set up grid codes to which wind farms need to comply to [66]. Wind farms should be able to provide grid balancing services using active power control [5, 62]. The objective of active power control, as in [6], is not yet implemented in a convex model predictive control formulation for wind turbines. Therefore, the development of a reference-based convex model predictive control framework for HWFs would be necessary. Note that a representation of the Pelton turbine needs to be included in the CEMPC framework in order to accurately control the active electrical power of a HWF.

3. Building upon the previously stated recommendation, to use the full potential of the wind farm, excess electrical power that can not be fed onto the grid could be redirected towards energy storage units or hydrogen plants in wind farms [1, 23]. Another interesting solution for HWFs is the inclusion of reversed osmosis (RO) units in an additional side branch of the hydraulic pipeline network [64, 72]. When the maximum attainable HWF power is higher than required on the electricity grid, excess power contained in the produced water flow can be redirected towards the RO units by controlling a flow valve. The redirected water flow is desalinated by the filters and can be used to produce fresh water. The inclusion of additional energy storage systems or RO units in the CEMPC framework should be further investigated.

4. In this study, wake interaction of wind turbines is not regarded, and the developed CEMPC framework is not capable of mitigating the corresponding negative effects. However, the development and adoption of wake control methods are considered as number one priority in wind farm control [73]. Therefore, the development of an interface that facilitates the possibility to add parallel wake controllers and wake models to the proposed CEMPC framework would be a valuable extension. Wake steering, wake induction, and wake mixing could be provided by deriving yaw angles, rotor power targets, and blade pitch angle references, respectively.

   An example could be an additional parallel yaw angle controller which periodically optimizes the yaw angles based on the mean wind speed directions from, e.g., the past 15 minutes, as developed in [6]. In this way, the yaw steering controller aims to maximize the incoming rotor effective wind power.
   A more complex combination would be the addition of a wake steering controller using a predictive dynamic wake model, which provides future wind speeds for all wind turbines in the farm. This way, wake steering is performed using the yaw angles provided by the parallel controller, and induction control is performed by the collaboration of the CEMPC controller and the predictive wake model. Note that the prediction horizon of the CEMPC should be long enough.
   The adoption of IPC in the CEMPC framework as in [18] could enable more complex wake mixing control strategies in the future.

Appendix A

Time-Domain Simulation Parameters

The parameters used in the simulation study and their source or motivation are presented in the following tables. Note that all the values obtained from Delft Offshore Turbine (DOT) are fictive.

Simulation

Symbol	**Description**	**Value**	**Unit**	**Source or motivation**
Δt_{s}	Plant model sampling time	0.01	s	Dinkla [18]
$\Delta t_{\mathrm{s,MPC}}$	CEMPC framework sampling time	0.2	s	Hovgaard [32]
$t_{\mathrm{s,staircase}}$	Staircase wind case simulation time	600	s	-
$t_{\mathrm{s,turbulent}}$	Staircase wind case simulation time	900	s	-

Controller

Symbol	**Description**	**Value**	**Unit**	**Source or motivation**
N_{p}	MPC prediction horizon	50	–	Hovgaard [32]
Δt_{MPC}	MPC time step size	0.2	s	Hovgaard [32]
α_1	Power maximization weight	2	–	Tuning
α_2	Rotor power rate limiting weight	1	–	Tuning
α_3	Pump power rate limiting weight	5	–	Tuning
α_4	Kinetic rotor energy rate limiting weight	30	–	Tuning
α_5	Overspeeding weight	1	–	Tuning
α_6	Turnpike weight	2	–	Tuning
γ	I&I wind speed estimator gain	15	–	Tuning
τ_{s}	pump displacement selector threshold	0.2	–	Tuning

Constraints

Symbol	**Description**	**Value**	**Unit**	**Source or motivation**
P_{rated}	Rated mechanical pump power	5.3	MW	NREL [36]
ω_{rated}	Rated rotor speed	1.2671	rads^{-1}	NREL [36]
ω_{min}	Minimum rotor speed	0.4294	rads^{-1}	NREL [36]
ω_{max}	Maximum rotor speed	1.6472	rads^{-1}	NREL [36]
ω_{max}	Maximum rotor speed	1.6472	rads^{-1}	NREL [36]
Δp_{nom}	Nominal network pressure	410	bar	DOT
V_{max}	Maximum pump displacement	0.1020	$\mathrm{m}^3\mathrm{rad}^{-1}$	DOT
V_{min}	Minimum pump displacement	0.0057	$\mathrm{m}^3\mathrm{rad}^{-1}$	DOT
s_{max}	Maximum spear position	0.0453	m	DOT
β_{min}	Minimum blade pitch angle	-5	$^\circ$	NREL [36]
β_{max}	Maximum blade pitch angle	20	$^\circ$	NREL [36]
λ^*	Optimal tip-speed ratio	6.5	–	NREL [36]
$C_{\mathrm{P,max}}$	Maximum power coefficient	0.4622	–	NREL [36]
Q_{cutin}	Cut-in flow single-turbine	0.02	m^3/s	Simulation
Q_{cutin}	Cut-in flow two-turbine	0.016	m^3/s	Simulation

Wind turbine

Symbol	**Description**	**Value**	**Unit**	**Source or motivation**
R	Rotor radius	63	m	NREL [36]
J	Combined mass moment of inertia	3.59e7	kgm^2	NREL [36] & DOT
ρ_{a}	Density of air	1.225	kgm^{-3}	Mulders [44]
t_β	Pitch actuator time constant	0.5	s	Mulders [44]

Hydraulic pump				
Symbol	**Description**	**Value**	**Unit**	**Source or motivation**
V_c	Constant displacement of single pump piston chamber	0.0057	$\mathrm{m}^3/\mathrm{rev}$	DOT
n_pistons	Amount of pump piston chambers	18	–	DOT
$\eta_\mathrm{v,rated}$	Rated volumetric pump efficiency	0.98	–	DOT
$\eta_\mathrm{m,rated}$	Rated mechanical pump efficiency	0.97	–	DOT
C_f	Dry friction coefficient	0.02	–	Diepeveen [17]
C_s	Laminar leakage coefficient	1e-13	$\mathrm{m}^3\mathrm{s}^{-1}\mathrm{Pa}^{-1}$	Derived in Section 2-2-1
C_damp	Viscous damping coefficient	2.72e8	Nms	Derived in Section 2-2-1
t_p	Pump displacement actuator time constant	0.05	s	Assumed to be fast

Hydraulic network				
Symbol	**Description**	**Value**	**Unit**	**Source or motivation**
L_L	Pipeline branch length single-turbine case	1000	m	Derived in Section C
L_L	Pipeline branch length two-turbine case	500	m	Derived in Section C
R_L	Pipeline diameter	0.08	m	Derived in Section C
ρ_w	Density of seawater	1026	kgm^{-3}	Van Didden [70]
μ	Dynamic viscosity of seawater	1.3e-3	Pas	Van Didden [70]
E_e	Effective bulk modulus	2.33e9	Pa	Van Didden [70]
ϵ_L	Relative internal surface roughness	5e-5	–	Van Didden [70]

Spear valve				
Symbol	**Description**	**Value**	**Unit**	**Source or motivation**
N_s	Number of spear valves	1	–	Selected in Section 2-4
D_nz	Nozzle diameter single-turbine case	0.0299	m	Derived in Section 2-4
D_nz	Nozzle diameter two-turbine case	0.0422	m	Derived in Section 2-4
α	Spear coning angle	50	°	Mulders [44]
C_d	Discharge coefficient	0.95	–	Laguna [35]
C_v	Vena-contracta coefficient	0.99	–	Laguna [35]
t_s	Spear actuator time constant	1.63	s	Mulders [44]

Pelton turbine				
Symbol	**Description**	**Value**	**Unit**	**Source or motivation**
R_PCD	Runner pitch circle radius	1.5	m	Laguna [35]
ζ	Pelton bucket friction factor	0.9	–	Laguna [35]
θ	Jet relative angle	165	°	Laguna [35]
η_g	Generator efficiency	0.944	–	NREL [36]

Appendix B

Two-Turbine Linear Parameter-Varying Hydraulic Network Model

When expanding the hydraulic pipeline model, derived in Section 2-3, towards a hydraulic network for a two-turbine farm, a model is needed to represent the hydraulic network connecting the two turbines to the spear valve and Pelton generator. A model can be constructed assuming two parallel pipeline segments, as shown in Figure B-1, coming from the two turbines, which come together in one single segment leading to the spear valve, as shown in Figure B-2. For clarity, the system equations for a single-pipeline model are restated,

$$\dot{p}_{\mathrm{c}} = \frac{1}{C_{\mathrm{H}}} Q_{\mathrm{c}}, \tag{2-32}$$

$$\dot{Q}_{\mathrm{c}} = \frac{R_2}{L_2}\left(Q_{\mathrm{i}} - Q_{\mathrm{c}}\right) + \dot{Q}_{\mathrm{i}} - \frac{1}{L_2} p_{\mathrm{c}} + \frac{1}{L_2} p_{\mathrm{o}}, \tag{2-34}$$

$$\ddot{p}_{\mathrm{c}} = \frac{R_2}{C_{\mathrm{H}} L_2} Q_{\mathrm{i}} - \frac{R_2}{L_2} \dot{p}_{\mathrm{c}} + \frac{1}{C_{\mathrm{H}}} \dot{Q}_{\mathrm{i}} - \frac{1}{C_{\mathrm{H}} L_2} p_{\mathrm{c}} + \frac{1}{C_{\mathrm{H}} L_2} p_{\mathrm{o}}, \tag{2-35}$$

Three assumptions are made. The first assumption is that the input flow of the third segment is the sum of the output flows of the two parallel segments

$$Q_{\mathrm{i}_3} = Q_{\mathrm{o}_1} + Q_{\mathrm{o}_2} = Q_{\mathrm{i}_1} - Q_{\mathrm{c}_1} + Q_{\mathrm{i}_2} - Q_{\mathrm{c}_2}, \tag{B-1}$$

$$\dot{Q}_{\mathrm{i}_3} = \dot{Q}_{\mathrm{o}_1} + \dot{Q}_{\mathrm{o}_2} = \dot{Q}_{\mathrm{i}_1} - \dot{Q}_{\mathrm{c}_1} + \dot{Q}_{\mathrm{i}_2} - \dot{Q}_{\mathrm{c}_2}. \tag{B-2}$$

Equation (B-2) can be rewritten as

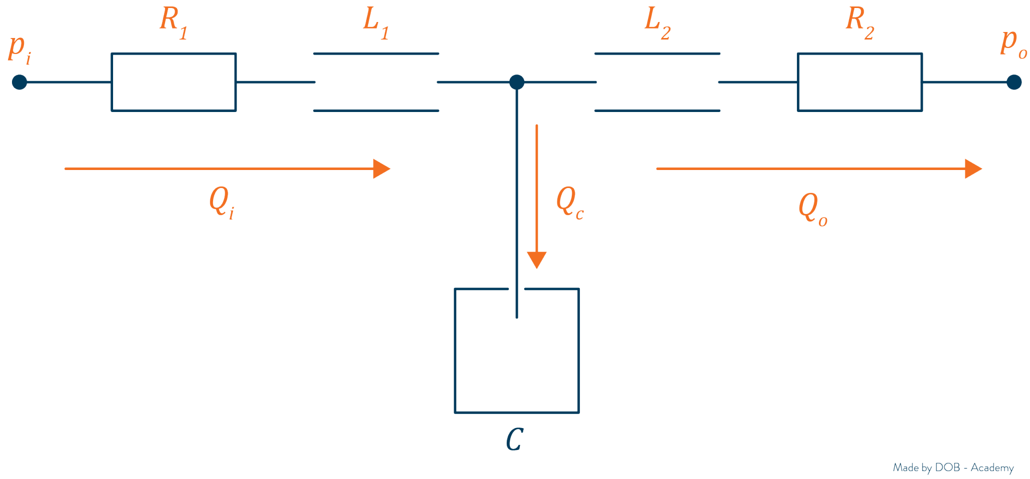

Figure B-1: Schematic overview of a pipeline segment, described in the electrical analogy. The inlet, net, and outlet pressure and flow of the pipeline segment are represented by p_i, Q_i, p_c, Q_c, p_o, and Q_o, respectively. The hydraulic resistance, induction, and capacitance terms are denoted as R_1, R_2, L_1, L_2, and C, respectively

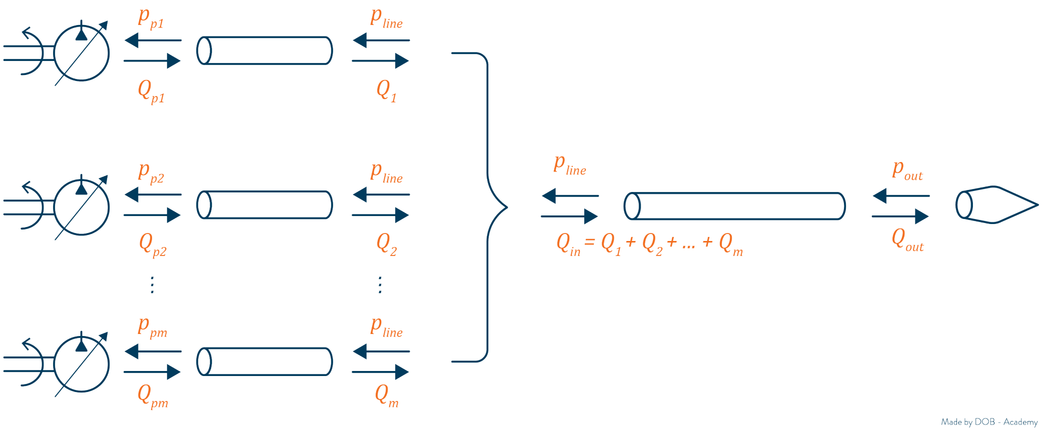

Figure B-2: A schematic overview of a multi-turbine hydraulic network model. Each cylinder represents a pipe segment, as depicted in Figure B-1. The m parallel pipelines originating from the wind turbines come together in a single pipe segment which leads to the spear valve. The inlet flow of this final pipeline is determined by the sum of the flows of its predecessors. It is assumed that the pressure p_line is equal for the parallel pipeline outlets.

$$\dot{Q}_{\mathrm{i}_3} = \frac{1}{L_1} p_{\mathrm{c}_1} + \frac{1}{L_2} p_{\mathrm{c}_2} + \frac{R_{21}}{L_1}\left(Q_{\mathrm{c}_1} - Q_{\mathrm{i}_1}\right) + \frac{R_{22}}{L_2}\left(Q_{\mathrm{c}_2} - Q_{\mathrm{i}_2}\right) - \left(\frac{1}{L_1} + \frac{1}{L_2}\right) p_{\mathrm{i}_3}, \tag{B-3}$$

The second assumption is that the pressure at the end of the first and second pipeline are equal to the pressure at the inlet of the third collective pipeline.

$$p_{\mathrm{i}_3} = p_{\mathrm{o}_1} = p_{\mathrm{o}_2} = p_{\mathrm{c}_3} + R_{13} Q_{\mathrm{i}_3} + L_3 \dot{Q}_{\mathrm{i}_3}. \tag{B-4}$$

When substituting (B-1) and (B-3) in (B-4), the following yields

$$\begin{aligned} p_{\mathrm{i}_3} = {} & \frac{\frac{1}{L_3}}{\frac{1}{L_1} + \frac{1}{L_2} + \frac{1}{L_3}} p_{\mathrm{c}_3} + \frac{\frac{R_{21}}{L_1} - \frac{R_{13}}{L_3}}{\frac{1}{L_1} + \frac{1}{L_2} + \frac{1}{L_3}}\left(Q_{\mathrm{c}_1} - Q_{\mathrm{i}_1}\right) + \frac{\frac{R_{22}}{L_2} - \frac{R_{13}}{L_3}}{\frac{1}{L_1} + \frac{1}{L_2} + \frac{1}{L_3}}\left(Q_{\mathrm{c}_2} - Q_{\mathrm{i}_2}\right) \\ & + \frac{\frac{1}{L_1}}{\frac{1}{L_1} + \frac{1}{L_2} + \frac{1}{L_3}} p_{\mathrm{c}_1} + \frac{\frac{1}{L_2}}{\frac{1}{L_1} + \frac{1}{L_2} + \frac{1}{L_3}} p_{\mathrm{c}_2}. \end{aligned} \tag{B-5}$$

The third assumption is that the length and diameter of the pipes are equal, therefore the characteristic terms become $L_1 = L_2 = L_3 = L_{\mathrm{H}}$ and $C_1 = C_2 = C_3 = C_{\mathrm{H}}$. Equations (B-5) and (B-3) can be reduced to

$$p_{\mathrm{i}_3} = \frac{1}{3}\left(p_{\mathrm{c}_1} + p_{\mathrm{c}_2} + p_{\mathrm{c}_3}\right) + \frac{R_{21} - R_{13}}{3}\left(Q_{\mathrm{c}_1} - Q_{\mathrm{i}_1}\right) + \frac{R_{22} - R_{13}}{3}\left(Q_{\mathrm{c}_2} - Q_{\mathrm{i}_2}\right), \tag{B-6}$$

$$\dot{Q}_{\mathrm{i}_3} = \frac{1}{L}\left(p_{\mathrm{c}_1} + p_{\mathrm{c}_2}\right) + \frac{R_{21}}{L}\left(Q_{\mathrm{c}_1} - Q_{\mathrm{i}_1}\right) + \frac{R_{22}}{L}\left(Q_{\mathrm{c}_2} - Q_{\mathrm{i}_2}\right) - \frac{2}{L} p_{\mathrm{i}_3}, \tag{B-7}$$

when substituting (B-6) back in (B-7) the following relations are found

$$\dot{Q}_{\mathrm{i}_3} = \frac{1}{3L}\left(p_{\mathrm{c}_1} + p_{\mathrm{c}_2} - 2p_{\mathrm{c}_3}\right) + \frac{R_{21} + 2R_{13}}{3L}\left(Q_{\mathrm{c}_1} - Q_{\mathrm{i}_1}\right) + \frac{R_{22} + 2R_{13}}{3L}\left(Q_{\mathrm{c}_2} - Q_{\mathrm{i}_2}\right). \tag{B-8}$$

Using the formulations presented in (2-32), (2-34), (2-35), (B-6), and (B-7), the following state-space representation of a two-turbine hydraulic network can be constructed:

$$\begin{bmatrix} \dot{p}_{\mathrm{c}_1} \\ \ddot{p}_{\mathrm{c}_1} \\ \dot{Q}_{\mathrm{c}_1} \\ \dot{p}_{\mathrm{c}_2} \\ \ddot{p}_{\mathrm{c}_2} \\ \dot{Q}_{\mathrm{c}_2} \\ \dot{p}_{\mathrm{c}_3} \\ \ddot{p}_{\mathrm{c}_3} \\ \dot{Q}_{\mathrm{c}_3} \end{bmatrix} = \underbrace{\begin{bmatrix} 0 & 0 & \frac{1}{C} & 0 & 0 & 0 & 0 & 0 & 0 \\ \frac{-2}{3CL} & \frac{-R_{21}}{L} & \frac{R_{21}-R_{13}}{3CL} & \frac{1}{3CL} & 0 & \frac{R_{22}-R_{13}}{3CL} & \frac{1}{3CL} & 0 & 0 \\ \frac{-2}{3L} & 0 & \frac{-2R_{21}-R_{13}}{3L} & \frac{1}{3L} & 0 & \frac{R_{22}-R_{13}}{3L} & \frac{1}{3L} & 0 & 0 \\ 0 & 0 & 0 & 0 & 0 & \frac{1}{C} & 0 & 0 & 0 \\ \frac{1}{3CL} & 0 & \frac{R_{21}-R_{13}}{3CL} & \frac{-2}{3CL} & \frac{-R_{22}}{L} & \frac{R_{22}-R_{13}}{3CL} & \frac{1}{3CL} & 0 & 0 \\ \frac{1}{3L} & 0 & \frac{R_{21}-R_{13}}{3L} & \frac{-2}{3L} & 0 & \frac{-2R_{22}-R_{13}}{3L} & \frac{1}{3L} & 0 & 0 \\ 0 & 0 & 0 & 0 & 0 & 0 & 0 & 0 & \frac{1}{C} \\ \frac{1}{3CL} & 0 & \frac{R_{21}+2R_{13}-3R_{23}}{3CL} & \frac{1}{3CL} & 0 & \frac{R_{22}+2R_{13}-3R_{23}}{3CL} & \frac{-5}{3CL} & \frac{-R_{23}}{L} & 0 \\ \frac{1}{3L} & 0 & \frac{R_{21}+2R_{13}-3R_{23}}{3L} & \frac{1}{3L} & 0 & \frac{R_{22}+2R_{13}-3R_{23}}{3L} & \frac{-5}{3L} & 0 & \frac{-R_{23}}{L} \end{bmatrix}}_{A} \begin{bmatrix} p_{\mathrm{c}_1} \\ \dot{p}_{\mathrm{c}_1} \\ Q_{\mathrm{c}_1} \\ p_{\mathrm{c}_2} \\ \dot{p}_{\mathrm{c}_2} \\ Q_{\mathrm{c}_2} \\ p_{\mathrm{c}_3} \\ \dot{p}_{\mathrm{c}_3} \\ Q_{\mathrm{c}_3} \end{bmatrix} \tag{B-9}$$

$$+ \underbrace{\begin{bmatrix} 0 & 0 & 0 & 0 & 0 \\ 0 & \frac{2R_{21}+R_{13}}{3CL} & \frac{1}{C} & \frac{-R_{22}+R_{13}}{3CL} & 0 \\ 0 & \frac{2R_{21}+R_{13}}{3L} & 1 & \frac{-R_{22}+R_{13}}{3L} & 0 \\ 0 & 0 & 0 & 0 & 0 \\ 0 & \frac{-R_{21}+R_{13}}{3CL} & 0 & \frac{2R_{22}+R_{13}}{3CL} & \frac{1}{C} \\ 0 & \frac{-R_{21}+R_{13}}{3L} & 0 & \frac{2R_{22}+R_{13}}{3L} & 1 \\ 0 & 0 & 0 & 0 & 0 \\ \frac{3}{3CL} & \frac{-R_{21}-2R_{13}+3R_{23}}{3CL} & 0 & \frac{-R_{22}-2R_{13}+3R_{23}}{3CL} & 0 \\ \frac{3}{3L} & \frac{-R_{21}-2R_{13}+3R_{23}}{3L} & 0 & \frac{-R_{22}-2R_{13}+3R_{23}}{3L} & 0 \end{bmatrix}}_{B} \begin{bmatrix} p_{\mathrm{o},3} \\ Q_{\mathrm{i}_1} \\ \dot{Q}_{\mathrm{i}_1} \\ Q_{\mathrm{i}_2} \\ \dot{Q}_{\mathrm{i}_2} \end{bmatrix}, \tag{B-10}$$

$$\begin{bmatrix} p_{\mathrm{i}_1} \\ p_{\mathrm{i}_2} \\ p_{\mathrm{i}_3} \\ Q_{\mathrm{o}_1} \\ Q_{\mathrm{o}_2} \\ Q_{o_3} \end{bmatrix} = \underbrace{\begin{bmatrix} 1 & 0 & 0 & 0 & 0 & 0 & 0 & 0 & 0 \\ 0 & 0 & 0 & 1 & 0 & 0 & 0 & 0 & 0 \\ \frac{1}{3} & 0 & \frac{R_{21}-R_{13}}{3} & \frac{1}{3} & 0 & \frac{R_{22}-R_{13}}{3} & \frac{1}{3} & 0 & 0 \\ 0 & 0 & -1 & 0 & 0 & 0 & 0 & 0 & 0 \\ 0 & 0 & 0 & 0 & 0 & -1 & 0 & 0 & 0 \\ 0 & 0 & -1 & 0 & 0 & -1 & 0 & 0 & -1 \end{bmatrix}}_{C} \begin{bmatrix} p_{\mathrm{c}_1} \\ \dot{p}_{\mathrm{c}_1} \\ Q_{\mathrm{c}_1} \\ p_{\mathrm{c}_2} \\ \dot{p}_{\mathrm{c}_2} \\ Q_{\mathrm{c}_2} \\ p_{\mathrm{c}_3} \\ \dot{p}_{\mathrm{c}_3} \\ Q_{\mathrm{c}_3} \end{bmatrix} \tag{B-11}$$

$$+ \underbrace{\begin{bmatrix} 0 & R_{11} & L & 0 & 0 \\ 0 & 0 & 0 & R_{12} & L \\ 0 & \frac{-R_{21}+R_{13}}{3} & 0 & \frac{-R_{22}+R_{13}}{3} & 0 \\ 0 & 1 & 0 & 0 & 0 \\ 0 & 0 & 0 & 1 & 0 \\ 0 & 1 & 0 & 1 & 0 \end{bmatrix}}_{D} \begin{bmatrix} p_{\mathrm{o},3} \\ Q_{\mathrm{i}_1} \\ \dot{Q}_{\mathrm{i}_1} \\ Q_{\mathrm{i}_2} \\ \dot{Q}_{\mathrm{i}_2} \end{bmatrix}. \tag{B-12}$$

Appendix C

Hydraulic Network Analysis

A frequency domain analysis of both the single-turbine and two-turbine hydraulic network model assuming steady-state flow has been performed to find suitable design parameters. For the two-turbine case, the input flows of the parallel lines are equal and the flow at the inlet of the collective pipeline is the sum of the upstream flows.

The natural frequency ω_n and corresponding damping factor ζ_n of the system can be derived using the following equations [44]:

$$\omega_\mathrm{n} = \sqrt{\frac{1}{C_\mathrm{H} L_\mathrm{H}}}, \tag{C-1}$$

$$\zeta_\mathrm{n} = \frac{R_\mathrm{H}}{2}\sqrt{\frac{C_\mathrm{H}}{L_\mathrm{H}}}. \tag{C-2}$$

The effects of the pipe segment flow, length, and radius are evaluated in the following subsections.

Pipeline flow

Larger pipeline flows lead to higher flow velocities, inducing pressure losses due to increased friction. This is captured in the flow dependent resistance term, given in Section 2-3. The increase in resistance at larger flows is visible in Table C-1, which shows the characteristic values of the resistance (damping), induction (mass inertia), and capacitance (spring stiffness) for different flow inputs. Equations (C-1) and (C-2), show that an increased flow provides additional damping without altering the natural frequencies of the system. This is visible as the reduced amplitudes, but same locations of the resonance peaks in Figure C-1. Finally, it is seen in Figure C-1c and Figure C-1d that a flow

Table C-1: System characteristics for different pipeline flows Q, corresponding to Figure C-1. The table presents the resistive R_{H}, induction R_{H}, and capacitive C_{H} terms.

Q $[m^3/s]$	R_{H} $[\mathrm{kgm^{-4}s^{-1}}]$		L_{H} $[\mathrm{kgm^{-4}}]$		C_{H} $[\mathrm{kg^{-1}m^4s^2}]$	
0.003	2.40e5	1.20e5	5.10e7	2.55e7	8.59e-9	4.30e-9
0.054	3.16e6	1.58e6	5.10e7	2.55e7	8.59e-9	4.30e-9
0.105	6.04e6	3.02e6	5.10e7	2.55e7	8.59e-9	4.30e-9
0.156	8.91e6	4.45e6	5.10e7	2.55e7	8.59e-9	4.30e-9

(left: single-turbine, right: two-turbine)

increase induce a higher DC gain posed by the input flow Q_{i}. The increased DC gain may impose control challenges, since there will be increased pressure losses. Accordingly, an offset between the pressure at the pump p_{i} and spear valve p_{o} side will arise, which makes controlling the pressure at the pump with the spear valve less straightforward.

Pipeline length

A larger pipeline length corresponds to a longer travel route under which it is exposed to friction losses, a larger length to cross-sectional area ratio of the pipeline, and a larger control volume. Accordingly, Table C-2 shows that the values of the resistance, induction, and capacitance terms gain proportionally with an increase of the pipe segment length. Considering (C-1), the natural frequency of the system shifts to lower frequencies. This is clearly seen in Figure C-2 as the shift in resonance peak locations. Furthermore, when investigating (C-2), damping increases when the pipe length is enlarged. This is evidently visible as a decrease in resonance peak amplitude in Figure C-2a and Figure C-2b.

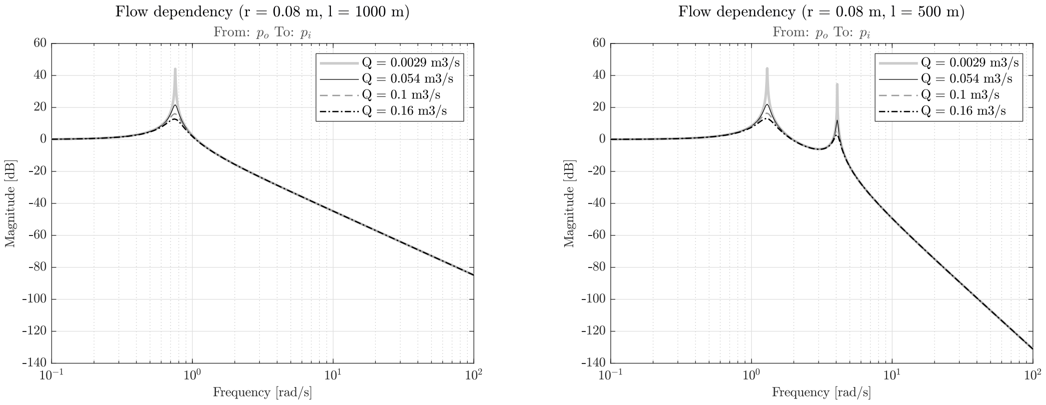

(a) Single-turbine (p_o to p_i)

(b) Two-turbine (p_o to p_i)

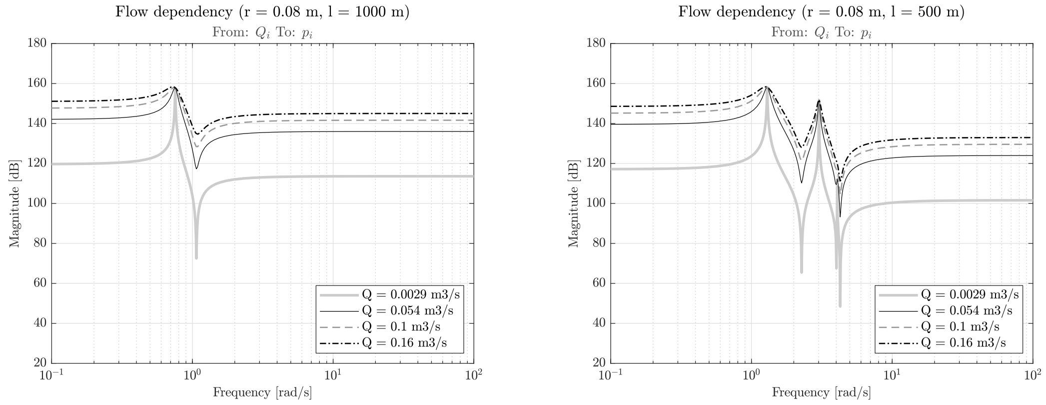

(c) Single-turbine (Q_i to p_i)

(d) Two-turbine (Q_i to p_i)

Figure C-1: The effect of flow on the bode response of a single-turbine (left) and two-turbine (right) hydraulic network for the system inputs: outlet pressure p_o (top) and inlet flow Q_i (bottom), to the system output: inlet pressure p_i. The pipeline flow influences the damping and DC gain of the system.

Another effect that arises when increasing the pipeline length, is an increase of DC gain in the bode which represents the influence of the inlet flow Q_i on the inlet pressure p_i, which can be clearly seen in Figure C-2c and Figure C-2d.

Table C-2: System characteristics for different pipeline Lengths L_{L}, corresponding to the results in Figure C-2. The table presents the resistive R_{H}, induction R_{H}, and capacitive C_{H} terms.

L_{L} [m]	R_{H} [kgm^{-4}s^{-1}]	L_{H} [kgm^{-4}]	C_{H} [kg^{-1}m^{4}s^{2}]
500	1.20e5	2.55e7	4.30e-9
1000	2.40e5	5.10e7	8.59e-9
1500	3.59e5	7.65e7	1.29e-8
2000	4.79e8	1.02e8	1.72e-8

(left: single-turbine, right: two-turbine)

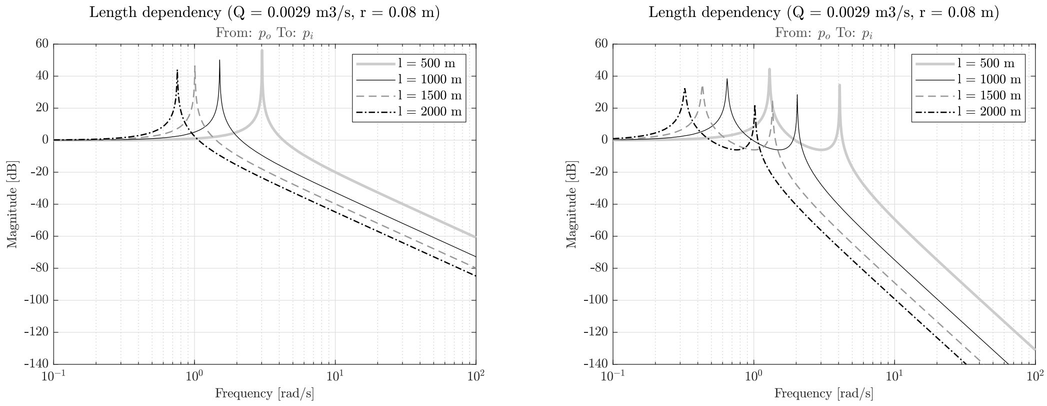

(a) Single-turbine (p_{o} to p_{i})

(b) Two-turbine (p_{o} to p_{i})

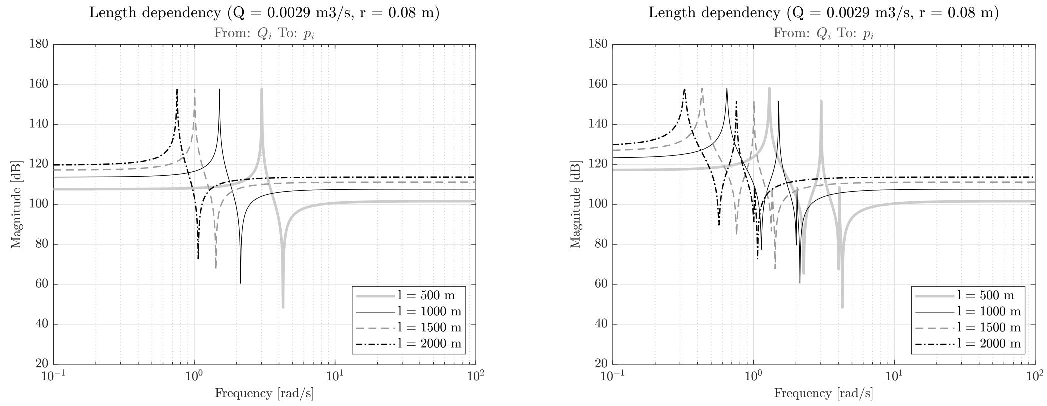

(c) Single-turbine (Q_{i} to p_{i})

(d) Two-turbine (Q_{i} to p_{i})

Figure C-2: Influence of different pipeline lengths on the bode response of a single-turbine (left) and two-turbine (right) hydraulic network for the system inputs: outlet pressure p_{o} (top) and inlet flow Q_{i} (bottom), to the system output: inlet pressure p_{i}. The pipeline influences the damping, natural frequencies, and DC gain of the system.

Pipeline radius

A larger pipeline radius corresponds to a lower pipe surface to fluid volume ratio, which reduces surface friction, a lower length to cross-sectional area ratio, and a larger control volume. Therefore, widening the pipeline results in decreasing resistance and induction terms, while the capacitive term increases, shown in Table C-3.

From the values in the table a relation of a change in radius and the change in hydraulic system terms L_H and C_H can be found:

$$nR_\mathrm{L} \longrightarrow \frac{1}{4}^{(n-2)} L_\mathrm{H}, \tag{C-3}$$

$$nR_\mathrm{L} \longrightarrow 4^{(n-2)} C_\mathrm{H}, \tag{C-4}$$

where n represents the factor of change in radius. Looking at the obtained relations and the equation in (C-1), it can be concluded that the natural frequencies of the system do not change for alterations of the pipeline radius, since the increase and decrease of L_H and C_H are complementary. This is visible in Figure C-3 as the resonance peaks do not change in frequency location.

When investigating the amplitude of the resonance peaks in Figure C-3, it is seen that an increase of the pipeline radius results in deteriorated damping. Finally, Figure C-3c and Figure C-3d show that the by enlarging the radius of the pipeline, the DC gain of the Q_i to p_i response is decreased.

Pipeline characteristics

R_L [m]	R_H [kgm^{-4}s^{-1}]	L_H [kgm^{-4}]	C_H [kg^{-1}m^{4}s^2]
0.025	8.03e7	5.23e8	8.39e-10
0.050	2.40e6	1.31e8	3.36e-9
0.075	3.28e5	5.81e7	7.55e-9
0.10	8.15e4	3.27e7	1.34e-8

(left: single-turbine, right: two-turbine)

Table C-3: System characteristics for different pipeline radii R_L, corresponding to the results of Figure C-3. The upper table presents the resistive R_H, induction R_H, and capacitive C_H terms. The lower table describes the following properties of a single-turbine (left values) and two-turbine (right values) hydraulic system model: phase margin PM, gain margin GM, and bandwidth ω_b.

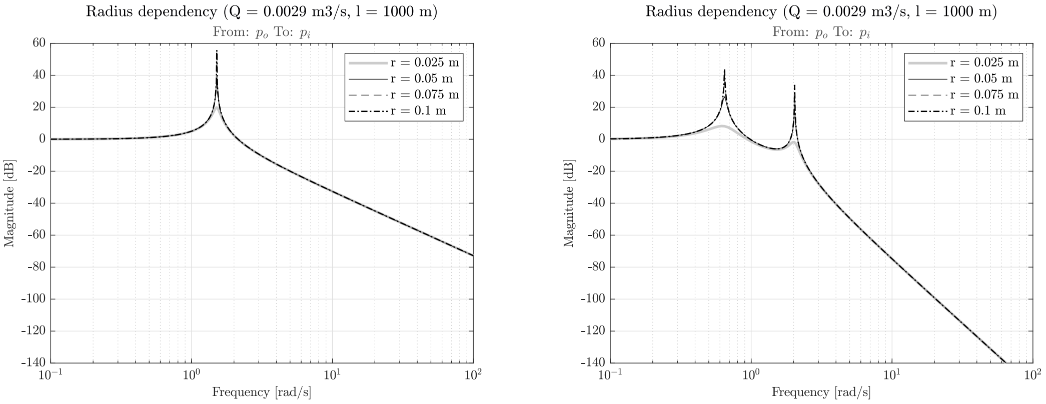

(a) Single-turbine (p_o to p_i)

(b) Two-turbine (p_o to p_i)

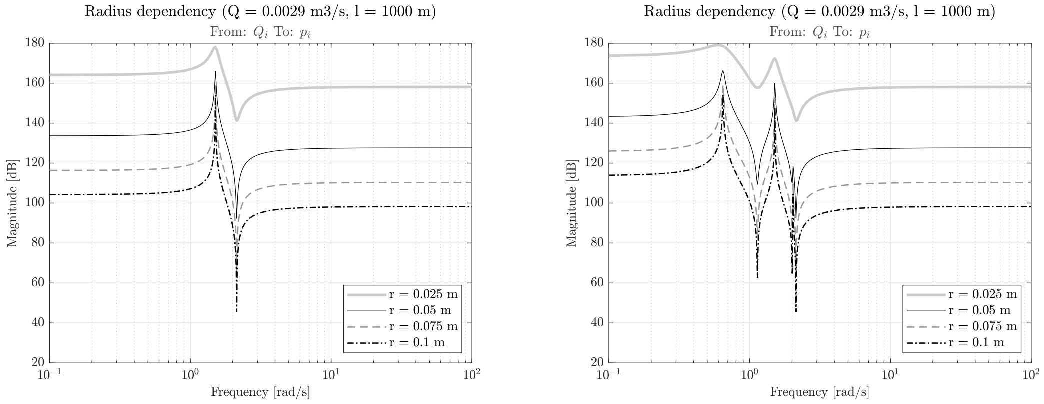

(c) Single-turbine (Q_i to p_i)

(d) Two-turbine (Q_i to p_i)

Figure C-3: Influence of different pipeline radii on the bode response of a single-turbine (left) and two-turbine (right) hydraulic network for the system inputs: outlet pressure p_o (top) and inlet flow Q_i (bottom), to the system output: inlet pressure p_i. The pipeline influences the damping and DC gain of the system. The natural frequencies remain unchanged.

Selecting network parameters

As seen in the previous two subsections, the characteristics of the network model can be tuned using the pipeline branch length L_L and the pipeline radius R_L. When choosing the values of L_L and R_L, one should also consider their effect on the stability of the controlled system, the bandwidth (system delay), and the increase in DC gain posed by the input flow Q_i. Time domain tuning is performed to find desired pipeline length and radius values for a stable and efficient controlled system.

The increase of the pipeline length adds damping and stability to the system, but causes larger pressure losses due to increased DC gain, moreover a larger system delay arises. These negative effects can be partially mitigated by enlarging the pipeline diameter. However, this decreases damping.

The tuned system parameters are given in Table C-4. The single-turbine configuration consists of a single pipeline segment, and the two-turbine of two parallel and one collective pipeline segment. It is assumed that a pipeline segment is built up by two branches with equal lengths L_L. Therefore, the total pipeline length, in which fluid flows from pump to spear valve, of the single and two-turbine configuration cases become $2L_\mathrm{L}$ and $4L_\mathrm{L}$, respectively. This means that the total pipeline length for both cases becomes $L_\mathrm{tot} = 2000$ meters.

Configuration	L_L [m]	R_L [m]
Single-turbine	1000	0.08
Two-turbine	500	0.08

Table C-4: Chosen network parameters for the pipeline segment branch length L_L and the pipeline diameter R_L.

Cut-in flow

As discussed in the previous sections, the flow has an effect on the damping and stability of the system. It is found that when the flow surpasses a certain cut-in flow lower bound, the controlled system becomes unstable. From the bode plot in Figure C-4 it can be seen that the phase margin of the hydraulic network model itself diminishes for smaller flows. Therefore, when adding the controller to the loop, the system could become unstable.

To find the value of this flow for the closed loop controller system, a declining ramp wind speed input is fed to the controlled system, shown in Figure C-5a. Note that the wind speed for turbine 1 is used for the single turbine case.

The resulting flows are given in Figure C-5. It is found that the cut-in pump flow for the single-turbine and two-turbine case are roughly 0.02 m^3/s and 0.0157 m^3/s, respectively.

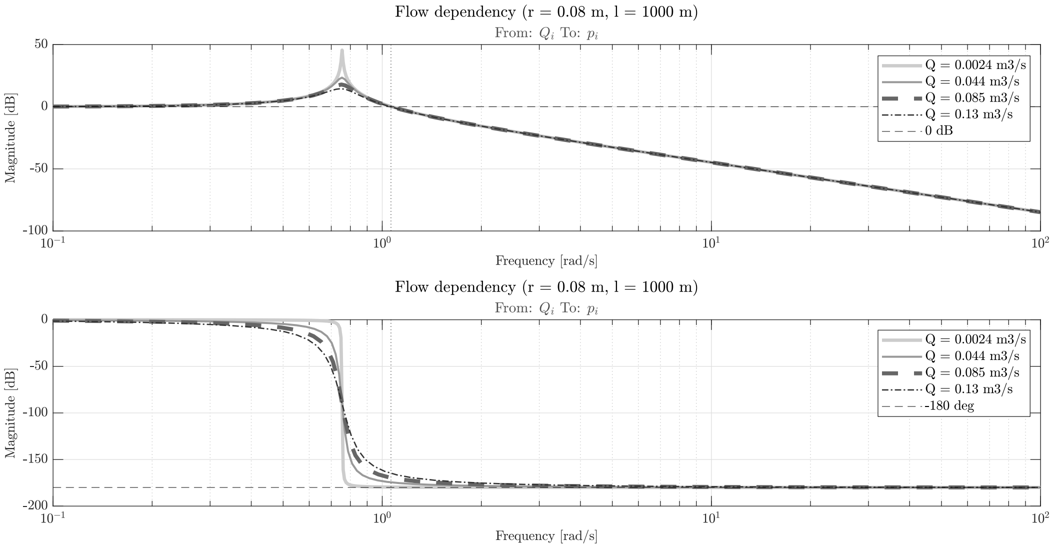

Figure C-4: Bode plot of the single turbine case showing the flow dependency. Note that the phase margin diminishes for smaller flows.

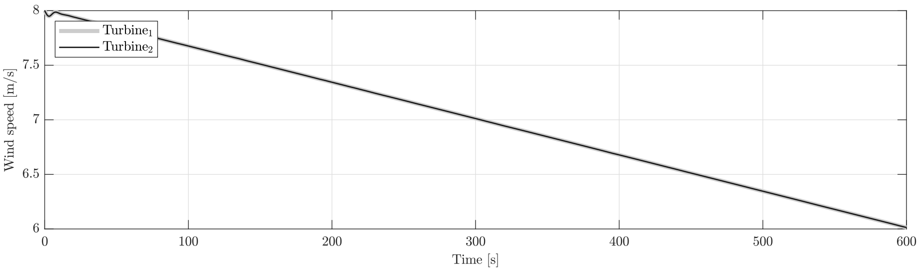

(a) Hub height decreasing ramp wind speed signals for two wind turbines.

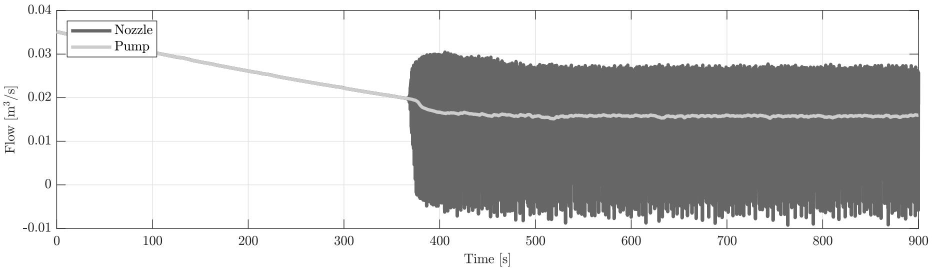

(b) Single-turbine flow.

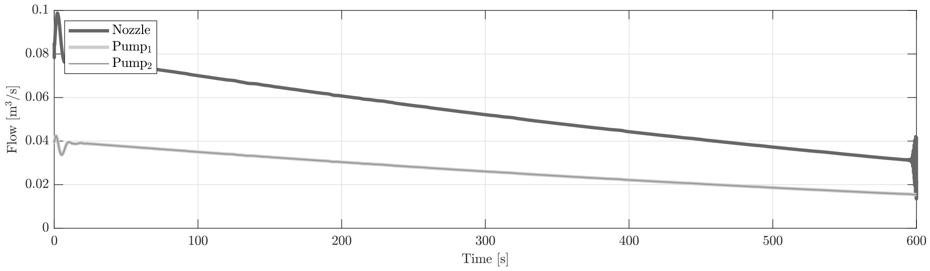

(c) Multi-turbine flow.

Figure C-5: Flow response of the controlled single-turbine and two-turbine system dependent on the ramp wind speed. The cut-in pump flow conditions can be found at the point where the nozzle flow becomes unstable.

Appendix D

Additional simulation results

This appendix encompasses additional simulation results not shown in Chapter 6 due to conciseness.

D-1 Wind case 1: Staircase throughout operating regime

In real-world scenarios, it is very unlikely that two turbines experience the exact same wind speed. Therefore, a situation where the second turbine experiences a different wind speed signal, given in Figure 6-2, is investigated: the wind speed signal of the second wind turbine is maintained at 7 m/s while the wind speed of the first turbine increases following the staircase signal used in the single-turbine case. These wind profiles are chosen to investigate the effect of diverging wind speeds throughout the wind farm, the resulting responses are presented in Figure D-1.

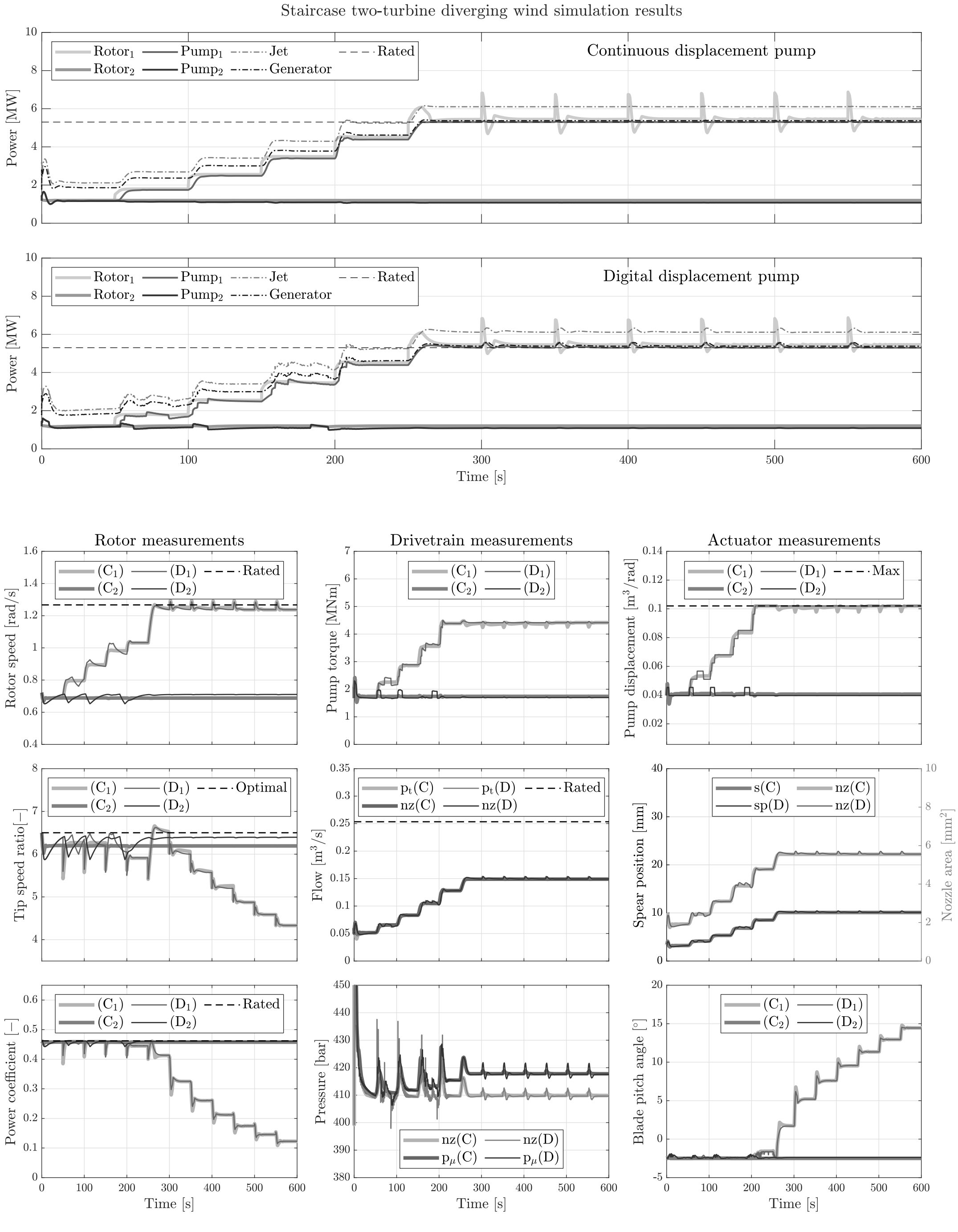

Figure D-1: Staircase two-turbine results. The upper plots show the power responses of the (C) and (D) case. Note that the depicted pump power is the mechanical pump power. The plant measurements are presented in the lower plots.

D-2 Wind case 4: Above-rated turbulent wind profile

The final wind case for which the convex economic model predictive control (CEMPC) framework performance is analyzed is for the above-rated wind speed signals, shown in Figure D-2.

Single-turbine control

Figure D-3 shows the single-turbine above-rated results, which are summarized in Table D-1. The power graphs show that the controllers are capable of maintaining the pump power around the rated value. Due to overspeeding and model-mismatches between the true system model and convex internal control model, the rated power is occasionally surpassed, also seen by the E_{O} and P_{O} values in Table D-1. The rotor speed is mainly regulated using the blade pitch angles, but small pump displacement activity is also visible.

The overall controlled system behavior resembles that of the above-rated regions of the rated wind profile case. When comparing the (C) and (D) case, it can be seen that the controller performs slightly worse in maintaining the rated power objective, seen by the higher rated pump power exceeded energy and power overshoot values E_{O} and P_{O}, respectively. Possible explanations are given in Section 6-4 and Section 6-5.

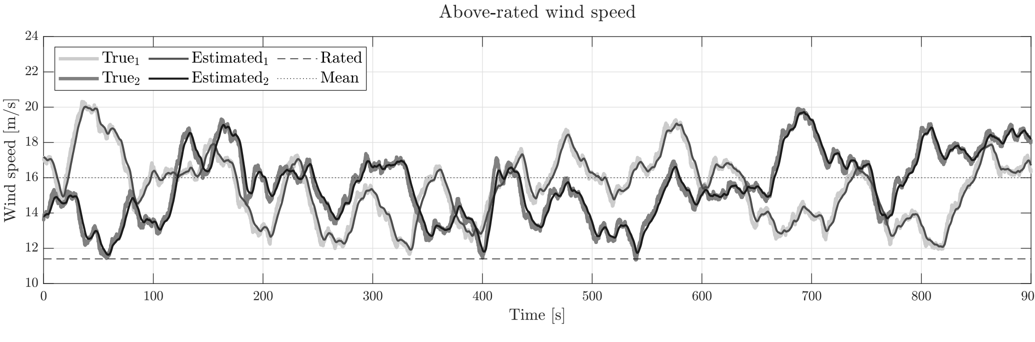

Figure D-2: Hub height above-rated wind speed signals with a 16 m/s mean. The true, immersion and invariance (I&I) estimated, rated, and mean wind speeds are depicted for two wind turbines.

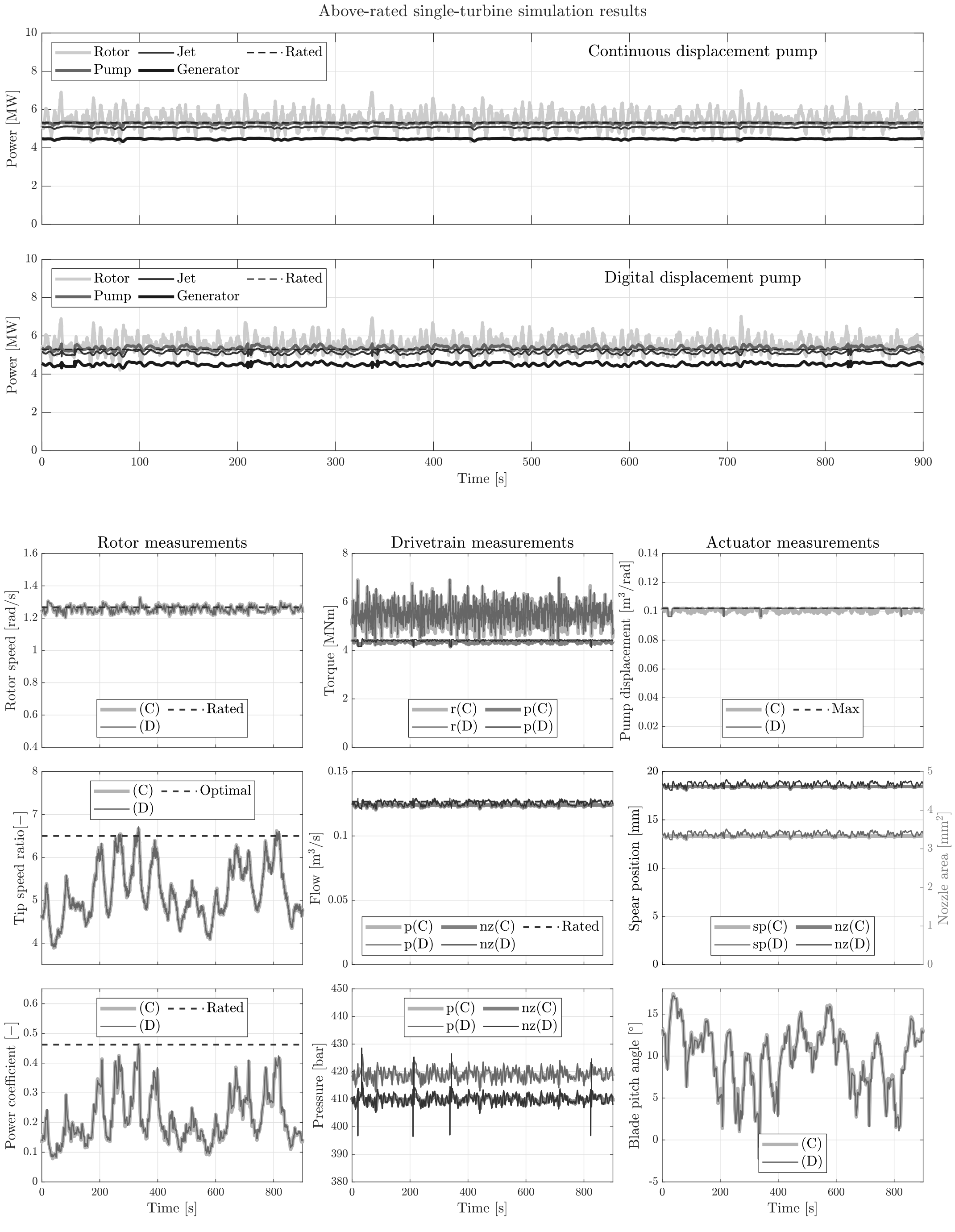

Figure D-3: Above-rated single-turbine results. The upper plots show the power responses of the (C) and (D) case. Note that the depicted pump power is the mechanical pump power. The plant measurements are presented in the lower plots.

Table D-1: Dynamic single-turbine hydraulic-drivetrain wind farm (HWF) performance of the continuously variable displacement pump (CDP) and digital displacement pump (DDP) case at above-rated turbulent wind speeds. The mean μ and standard deviations σ and σ/μ of various parameters are presented. Total produced energies are given by E, the portion that is obtained by above-rated powers by E_O, and maximum overshoots by P_O, η_max describes the efficiency with respect to the maximum attainable power maximum pump and generator efficiencies. The efficiency compared to National Renewable Energy Laboratory (NREL) 5-MW reference turbines is denoted by η_NREL. Note that the mechanical pump power is presented in this table.

	(C)			(D)		
Turbine 1	μ	σ	σ/μ	μ	σ	σ/μ
Rotor power [MW]	5.5	0.40	7.4%	5.5	0.38	6.9%
Pump power [MW]	5.2	0.033	0.63%	5.3	0.093	1.8%
Jet power [MW]	5.1	0.027	0.53%	5.1	0.085	1.7%
Generator power [MW]	4.5	0.024	0.54%	4.5	0.076	1.7%
Power coefficient [-]	0.21	0.083	39%	0.22	0.083	39%
Pump efficiency [-]	0.95	0.07	7.3%	0.95	0.064	6.7%
Pipeline efficiency [-]	0.98	0.0033	0.34%	0.98	0.0079	0.81%
Pelton efficiency [-]	0.88	0.00011	0.012%	0.88	0.00019	0.021%
Pump pressure [bar]	419	1.1	0.25%	419	2.0	0.49%
Nozzle pressure [bar]	410	0.94	0.23%	410	1.7	0.41%
	E	E_O	P_O	E	E_O	P_O
Pump Energy [MWh]	1.3	0.14%	1.2%	1.3	1.5%	5.4%
	E	η_max	η_NREL	E	η_max	η_NREL
Electrical energy [MWh]	1.1	91%	89%	1.1	92%	90%

Two-turbine control

The two-turbine above-rated results are presented in Figure D-4 and summarized in Table D-2. When comparing the two-turbine results with the single-turbine controller results, similar differences have been found as described in the previous wind cases. A difference in controller behavior, however, is that the two-turbine controller makes more use of the pump displacements to maintain the pump power beneath the rated value. Even the (D) case shows rapid digital pump displacement switching. It is probable that this is necessary due to increased above-rated wind speed deviation intensity.

Table D-2: Dynamic two-turbine HWF performance of the CDP and DDP case at above-rated turbulent wind speeds. The mean μ and standard deviations σ and σ/μ of various parameters are presented. Total produced energies are given by E, the portion that is obtained by above-rated powers by E_O, and maximum overshoots by P_O, η_max describes the efficiency with respect to the maximum attainable power maximum pump and generator efficiencies. The efficiency compared to NREL 5-MW reference turbines is denoted by η_NREL. Note that the mechanical pump power is presented in this table.

	(C)			(D)		
Turbine 1	μ	σ	σ/μ	μ	σ	σ/μ
Rotor power [MW]	5.5	0.46	8.4%	5.5	0.47	8.6%
Pump power [MW]	5.2	0.032	0.61%	5.2	0.11	2.1%
Power coefficient [-]	0.21	0.084	39%	0.21	0.085	40%
Pump efficiency [-]	0.96	0.079	8.3%	0.96	0.077	8.1%
Pump pressure [bar]	430	0.89	0.21%	430	2.3	0.54%
	E	E_O	P_O	E	E_O	P_O
Pump energy [MWh]	1.3	0.14%	1.2%	1.3	0.96%	6.5%
Turbine 2	μ	σ	σ/μ	μ	σ	σ/μ
Rotor power [MW]	5.5	0.49	8.9%	5.5	0.52	9.5%
Pump power [MW]	5.2	0.033	0.64%	5.2	0.12	2.2%
Power coefficient [-]	0.21	0.086	41%	0.21	0.087	41%
Pump efficiency [-]	0.96	0.085	8.9%	0.96	0.083	8.7%
Pump pressure [bar]	430	0.90	0.21%	430	2.3	0.54%
	E	E_O	P_O	E	E_O	P_O
Pump energy [MWh]	1.3	0.14%	1.1%	1.3	0.96%	6.5%
Collective	μ	σ	σ/μ	μ	σ	σ/μ
Jet power [MW]	9.9	0.039	0.39%	10	0.15	1.5%
Generator power [MW]	8.7	0.035	0.40%	8.8	0.14	1.6%
Pipeline efficiency [-]	0.96	0.0022	0.23%	0.96	0.0092	0.96%
Pelton efficiency [-]	0.88	8.4e-05	0.0095%	0.88	0.00022	0.026%
Nozzle pressure [bar]	410	0.75	0.18%	410	2.0	0.5%
	E	η_max	η_NREL	E	η_max	η_NREL
Electrical energy [MWh]	2.2	89%	87%	2.2	89%	88%

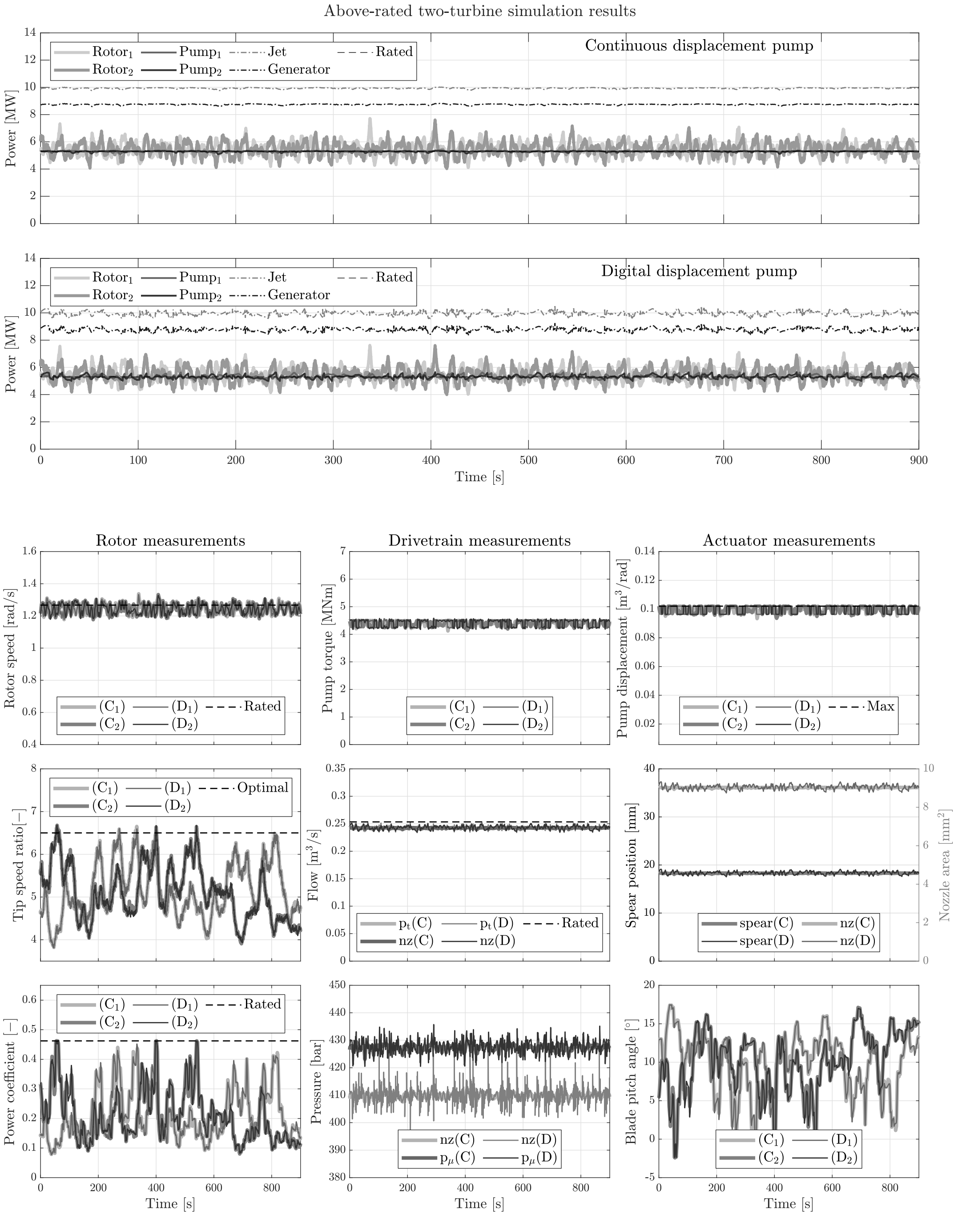

Figure D-4: Above-rated two-turbine results. The upper plots show the power responses of the (C) and (D) case. Note that the depicted pump power is the mechanical pump power. The plant measurements are presented in the lower plots.

Appendix E

Feedback-feedforward compensation spear valve controller

As the synthesized convex economic model predictive control (CEMPC) framework is not able to adequately control the nozzle pressure, an additional feedback loop can be included to trim the pressure to its nominal value. The CEMPC controller is used to calculate an initial guess of the desired spear valve area, based on the optimized control variables and plant measurements. This value is used as a feedforward signal. The feedback loop, containing a simple proportional gain $K_\mathrm{P} = -5e{-}10$, is used for trimming the pressure to the required value. This concept is known as feedback with feedforward compensation (FB-FFC) and is used in non-linear control of mechanical actuators similar to the presented application [9]. A schematic overview of the implemented system is given in Figure E-1.

The results of the original CEMPC framework and FB-FFC-aided controller framework, subjected to the rated wind speed signals used in Section 6-5, are shown in Figure E-2 and in Table E-1. It is seen that the hybrid controller is much better at handling fast variations in pressure, leading to improved nominal nozzle pressure control, showing more stable nozzle and pump pressure responses. In terms of power production and efficiencies, there are no significant changes as seen in Table E-1. However, it can be seen that standard deviations of the FB-FFC-aided CEMPC case are reduced, mainly in the pressure deviations.

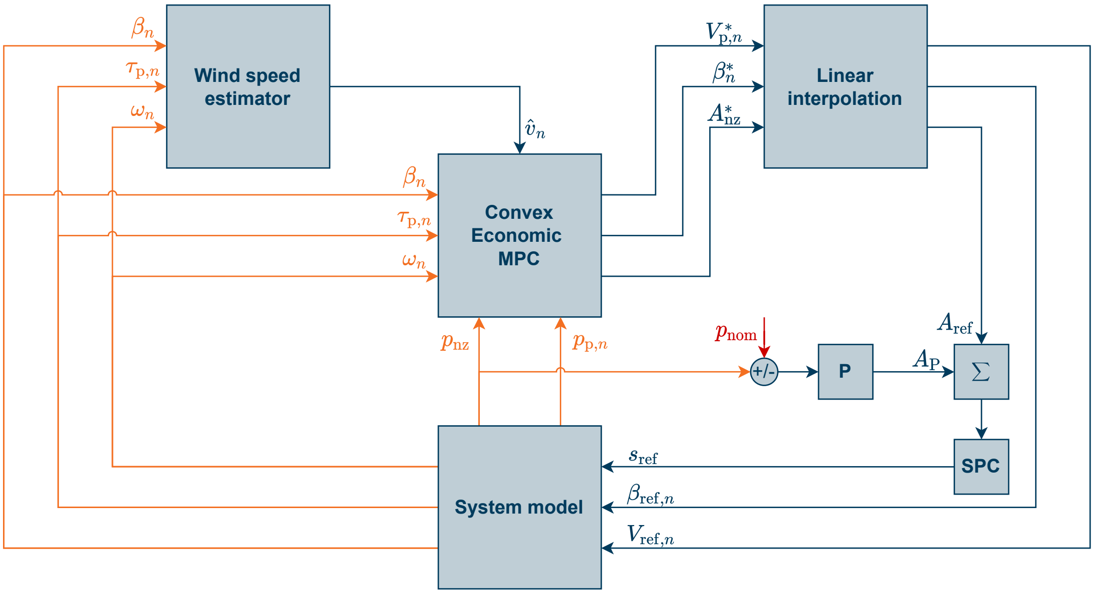

Figure E-1: A control diagram that shows the dependencies between different control components and the investigated HWF. A rotor-effective wind speed estimates $\hat{v}_n$ of the wind speeds v_n acting on each wind turbine n is provided to the implemented CEMPC block by an immersion and invariance (I&I) wind speed estimator. Other inputs of the controller comprise measurements of the blade pitch angles β_n, pump torques $\tau_{\mathrm{p},n}$, rotor speeds ω_n, pump pressures $p_{\mathrm{p},n}$, and nozzle pressure p_{nz}. The optimized controller outputs consist of the solution trajectories of the pump displacements $V_{\mathrm{p},n}$, blade pitch angles β_n, and spear valve area A_{ref}. The solutions of the first time step in the predicted horizon are selected and linearly interpolated to avoid large input transients. The optimized nozzle area A_{ref} is summed with the feedback signal A_{P}, created by the proportional gain P, and fed into the spear position compensator. The resulting spear position s_{ref} and the optimized blade pitch angles $\beta_{\mathrm{ref,n}}$ and pump displacement values $V_{\mathrm{ref,n}}$ are used as inputs of the system model of the hydraulic-drivetrain wind farm (HWF).

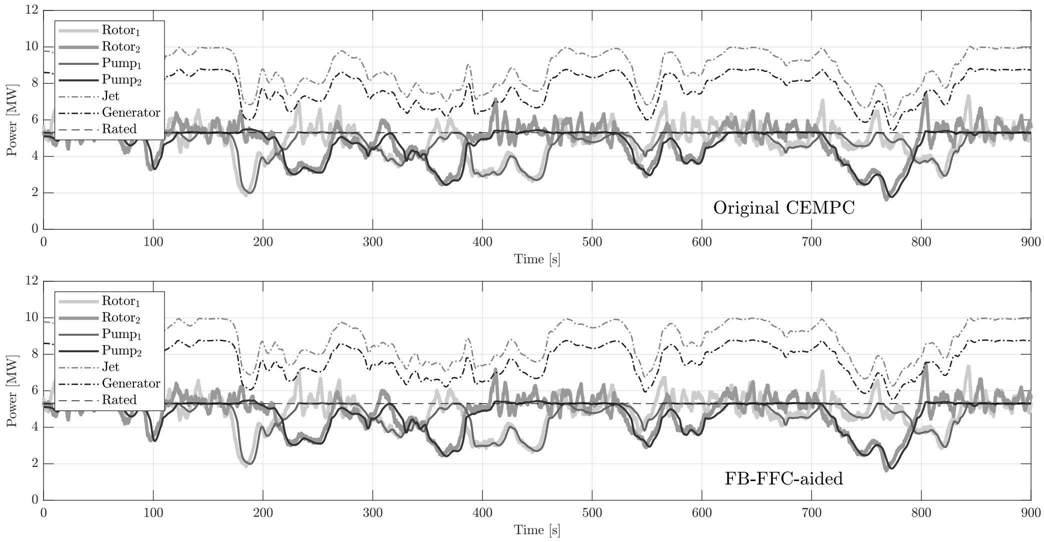

(a) Power response.

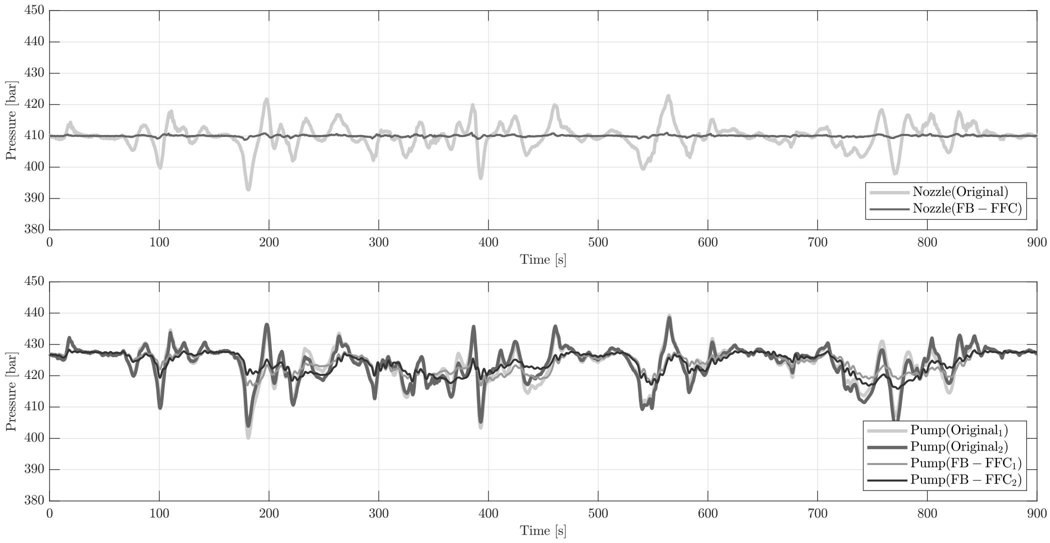

(b) Pressure response.

Figure E-2: Rated two-turbine results using the proposed feedback with feedforward compensation method. The upper plots show the power responses of the (C) and (D) case. Note that the depicted pump power is the mechanical pump power. The plant measurements are presented in the lower plots.

Table E-1: Dynamic two-turbine HWF performance of the original and FB-FFC case at rated turbulent wind speeds. The mean μ and standard deviations σ and σ/μ of various parameters are presented. Total produced energies are given by E, the portion that is obtained by above-rated powers by PE, and maximum overshoots by PO, $\eta_{\max}$ describes the efficiency with respect to the maximum attainable power maximum pump and generator efficiencies. The efficiency compared to National Renewable Energy Laboratory (NREL) 5-MW reference turbines is denoted by η_{NREL}. Note that the mechanical pump power is presented in this table.

	(C)			(D)		
Turbine 1	μ	σ	σ/μ	μ	σ	σ/μ
Rotor power [MW]	4.9	0.91	19%	4.9	0.93	19%
Pump power [MW]	4.6	0.77	17%	4.6	0.80	17%
Power coefficient [-]	0.40	0.073	18%	0.40	0.072	18%
Pump efficiency [-]	0.95	0.093	9.7%	0.95	0.093	9.7%
Pump pressure [bar]	424	5.5	1.3%	424	3.0	0.71%
	E	PE	PO	E	PE	PO
Pump energy [MWh]	1.2	0.044%	0.69%	1.2	0.042%	0.69%
Turbine 2	μ	σ	σ/μ	μ	σ	σ/μ
Rotor power [MW]	4.8	1.0	21%	4.8	1.0	21%
Pump power [MW]	4.5	0.88	19%	4.5	0.88	19%
Power coefficient [-]	0.41	0.068	17%	0.41	0.068	17%
Pump efficiency [-]	0.95	0.088	9.2%	0.95	0.088	9.3%
Pump pressure [bar]	424	5.6	1.3%	424	3.2	0.75%
	E	PE	PO	E	PE	PO
Pump energy [MWh]	1.1	0.055%	0.87%	1.1	0.050%	0.79%
Collective	μ	σ	σ/μ	μ	σ	σ/μ
Jet power [MW]	8.8	1.0	12%	8.8	1.0	11%
Generator power [MW]	7.8	0.90	12%	7.8	0.89	11%
Pipeline efficiency [-]	0.97	0.0089	0.93%	0.97	0.0068	0.7%
Pelton efficiency [-]	0.88	0.00046	0.052%	0.88	2.9e-5	0.0033%
Nozzle pressure [bar]	410	4.0	0.97%	410	0.26	0.063%
	E	$\eta_{\max}$	η_{NREL}	E	$\eta_{\max}$	η_{NREL}
Electrical energy [MWh]	1.9	90%	87%	1.9	90%	87%

Bibliography

[1] T. R. Ayodele and J. L. Munda. Potential and economic viability of green hydrogen production by water electrolysis using wind energy resources in South Africa. *International Journal of Hydrogen Energy*, 44(3):17669–17687, 2019.

[2] M. Becker, B. Ritter, B. Doekemeijer, D. van der Hoek, U. Konigorski, D. Allaerts, and J.W. van Wingerden. The revised FLORIDyn model: Implementation of heterogeneous flow and the Gaussian wake. *Wind Energy Science Discussions*, pages 1–25, 2022.

[3] A. Betz. *Wind-energie und ihre ausnutzung durch windmühlen*, volume 2. Vandenhoeck & Ruprecht, 1926.

[4] F. D. Bianchi, H. De Battista, and R.J. Mantz. *Wind turbine control systems: principles, modelling and gain scheduling design*, volume 19. Springer, 2007.

[5] S. Boersma, B. M. Doekemeijer, P. M.O. Gebraad, P. A. Fleming, J. Annoni, A. K. Scholbrock, J. A. Frederik, and J. W. Van Wingerden. A tutorial on control-oriented modeling and control of wind farms. *2017 American Control Conference (ACC)*, pages 1–18, 2017.

[6] S. Boersma, B. M. Doekemeijer, S. Siniscalchi-Minna, and J. W. van Wingerden. A constrained wind farm controller providing secondary frequency regulation: An LES study. *Renewable Energy*, 134:639–652, 2018.

[7] BP. Statistical Review of World Energy. Technical report, BP, 2020.

[8] D. Buhagiar, T. Sant, and M. Bugeja. A comparison of two pressure control concepts for hydraulic offshore wind turbines. *Journal of Dynamic Systems, Measurement and Control, Transactions of the ASME*, 138(8):1–11, 2016.

[9] D. Buhagiar, T. Sant, and M. K. Bugeja. Control of an open-loop hydraulic offshore wind turbine using a variable-area orifice. *International Conference on Offshore Mechanics and Arctic Engineering*, 56574:V009T09A043, 2015.

[10] T. Burton, N. Jenkins, and E. Sharpe, D.and Bossanyi. *Wind energy handbook.* John Wiley & Sons, 2011.

[11] CBS. Energieverbruik particuliere woningen, woningtype en regio's. Technical report, CBS, 2020.

[12] W. Chen, X. Wang, F. Zhang, H. Liu, and Y. Lin. Review of the application of hydraulic technology in wind turbine. *Wind Energy*, 23(7):1495–1522, 2020.

[13] P.S.G. Cisneros, S. Voss, and H. Werner. Efficient nonlinear model predictive control via quasi-lpv representation. In *2016 IEEE 55th Conference on Decision and Control (CDC)*, pages 3216–3221. IEEE, 2016.

[14] Á.M. Costa, J.A. Orosa, D. Vergara, and P. Fernández-Arias. New tendencies in wind energy operation and maintenance. *Applied Sciences*, 11(4):1386, 2021.

[15] B. De Schutter and W.P.M.H. Heemels. Lecture notes on modeling and control of hybrid systems. *TU Delft Catalogus*, 2015.

[16] M. Deldar, A. Izadian, and S. Anwar. A decentralized multivariable controller for hydrostatic wind turbine drivetrain. *Asian Journal of Control*, 22(3):1038–1051, 2020.

[17] N.F.B. Diepeveen. On the application of fluid power transmission in offshore wind turbines. 2013.

[18] R. Dinkla. Towards convex economic model predictive individual pitch control for wind turbine load mitigation. 2021.

[19] S. L. Dixon and C. A. Hall. *Fluid mechanics and thermodynamics of turbomachinery.* Butterworth-Heinemann, 2013.

[20] EERE DOE. Advanced wind turbine drivetrain concepts: Workshop report, june 29-30, 2010. 2010. National Renewable Energy Lab.(NREL), Golden, CO (United States).

[21] B. M. Doekemeijer, S. Kern, S. Maturu, S. Kanev, B. Salbert, J. Schreiber, F. Campagnolo, C. L. Bottasso, S. Schuler, F. Wilts, T. Neumann, G. Potenza, F. Calabretta, and F. Fioretti. Field experiment for open-loop yaw-based wake steering at a commercial onshore wind farm in Italy. *Wind Energy Science*, 6(1):159–176, 2021.

[22] DOWA. Mean wind speed per wind farm zone and Cabauw (100m). Technical report, DOWA.

[23] D. P. e Silva, J. F. Salles, J. L. F.and Fardin, and M. M. R. Pereira. Management of an island and grid-connected microgrid using hybrid economic model predictive control with weather data. *Applied Energy*, 278:115581, 2020.

[24] M.A. Evans, M. Cannon, and B. Kouvaritakis. Robust MPC tower damping for variable speed wind turbines. *IEEE Transactions on Control Systems Technology*, 23(1):290–296, 2015.

[25] C. Fetting. The European Green Deal. *ESDN Report*, 2020. ESDN Office, Vienna.

[26] N. Fichaux, J. Beurskens, P. H. Jensen, and J. Wilkes. Design limits and solutions for very large wind turbines: A 20 MW turbine is feasible. *UpWind Report*, 2011.

[27] J. A. Frederik, B. M. Doekemeijer, S. P. Mulders, and J. W. van Wingerden. The helix approach: using dynamic individual pitch control to enhance wake mixing in wind farms. *Wind Energy*, 23(8):1739–1751, 2020.

[28] S. Gros. An economic NMPC formulation for wind turbine control. In *52nd IEEE Conference on Decision and Control*, pages 1001–1006. IEEE, 2013.

[29] S. E. Haaland. Simple and explicit formulas for the friction factor in turbulent pipe flow. 1983.

[30] E. Hernandez-Estrada, O. Lastres-Danguillecourt, J. B. Robles-Ocampo, A. Lopez-Lopez, P. Y. Sevilla-Camacho, B.Y. Perez-Sariñana, and J. R. Dorrego-Portela. Considerations for the structural analysis and design of wind turbine towers: A review. *Renewable and Sustainable Energy Reviews*, 137:110447, 2021.

[31] S. Hovgaard, T. G.and Boyd and J. B. Jørgensen. Model predictive control for wind power gradients. *Wind Energy*, 18(6):991–1006, 2015.

[32] T.G. Hovgaard, L.F.S. Larsen, J.B. Jørgensen, and S. Boyd. MPC for wind power gradients - Utilizing forecasts, rotor inertia, and central energy storage. In *2013 European Control Conference (ECC)*, pages 4071–4076. IEEE, 2013.

[33] IRENA Renewable Cost Database. *Renewable Power Generation Costs in 2020*. International Renewable Energy Agency, 2020. Abu Dhabi.

[34] H. Ishaq, I. Dincer, and G.F. Naterer. Performance investigation of an integrated wind energy system for co-generation of power and hydrogen. *International Journal of Hydrogen Energy*, 43(19):9153–9164, 2018.

[35] A. Jarquín Laguna. Centralized electricity generation in offshore wind farms using hydraulic networks. 2017.

[36] J. Jonkman, S. Butterfield, W. Musial, and G. Scott. Definition of a 5-MW reference wind turbine for offshore system development. National Renewable Energy Lab.(NREL), Golden, CO (United States), 2009.

[37] N. D. Kelley and B.J. Jonkman. Overview of the TurbSim stochastic inflow turbulence simulator. pages 1–13. National Renewable Energy Lab.(NREL), Golden, CO (United States), 2005.

[38] W. H. Lio, J. A. Rossiter, and B. L. Jones. A review on applications of model predictive control to wind turbines. In *2014 Ukacc international conference on control (control)*, pages 673–678. IEEE, 2014.

[39] Y. Liu, A.K. Pamososuryo, R. Ferrari, and J.W. van Wingerden. The immersion and invariance wind speed estimator revisited and new results. *IEEE Control Systems Letters*, pages 361–366, 2021.

[40] L. Magni and R. Scattolini. An overview of nonlinear model predictive control. *Automotive model predictive control*, pages 107–117, 2010.

[41] M.S. Mahmoud and M.O. Oyedeji. Adaptive and predictive control strategies for wind turbine systems: A survey. *IEEE/CAA Journal of Automatica Sinica*, 6(2):364–378, 2019.

[42] H.E. Merritt. Hydraulic control systems. *J. Wiley*, 1967.

[43] S.P. Mulders. Wind turbine control: Advances for load mitigations and hydraulic drivetrains. 2020.

[44] S.P. Mulders, N.F.B. Diepeveen, and J.W. van Wingerden. Control design, implementation, and evaluation for an in-field 500 kw wind turbine with a fixed-displacement hydraulic drivetrain. *Wind Energy Science*, 3(2):615–638, 2018.

[45] S.P. Mulders, N.F.B. Diepeveen, and J.W. Van Wingerden. Extremum seeking control for optimization of a feed-forward pelton turbine speed controller in a fixed-displacement hydraulic wind turbine concept. In *Journal of Physics: Conference Series*, volume 1222, page 012015. IOP Publishing, 2019.

[46] V. Okulov, J. N. Sørensen, and G.A.M. van Kuik. Development of the optimum rotor theories: On the 100th anniversary of professor joukowsky's vortex theory of screw propeller. 2013.

[47] R. Ortega, F. Mancilla-David, and F. Jaramillo. A globally convergent wind speed estimator for wind turbine systems. *International Journal of Adaptive Control and Signal Processing*, 27(5):413–425, 2013.

[48] L.Y. Pao and K.E. Johnson. A tutorial on the dynamics and control of wind turbines and wind farms. In *2009 American Control Conference*, pages 2076–2089. IEEE, 2009.

[49] Petroleum, British. Energy Outlook 2020 edition explores the forces shaping the global energy transition out to 2050 and the surrounding that transition. *British Petroleum: London, UK*, 2020.

[50] C. Qin, E. Innes-Wimsatt, and E. Loth. Hydraulic-electric hybrid wind turbines: Tower mass saving and energy storage capacity. *Renewable Energy*, 99:69–79, 2016.

[51] A. Ragheb and M. Ragheb. Wind turbine gearbox technologies. In *2010 1st international nuclear & renewable energy conference (INREC)*, pages 1–8. IEEE, 2010.

[52] J.B. Rawlings, D. Angeli, and C.N. Bates. Fundamentals of economic model predictive control. *Proceedings of the IEEE Conference on Decision and Control*, pages 3851–3861, 2012.

[53] M.J. Risbeck. *Mixed-integer model predictive control with applications to building energy systems*. The University of Wisconsin-Madison, 2018.

[54] D. Schlipf, Pa. Grau, S. Raach, R. Duraiski, J. Trierweiler, and P.W. Cheng. Comparison of linear and nonlinear model predictive control of wind turbines using LIDAR. In *2014 American Control Conference*, pages 3742–3747. IEEE, 2014.

[55] K. Schmitz and H. Murrenhoff. *Grundlagen der Fluidtechnik: Teil 1: Hydraulik*. Shaker, 2018.

[56] A. Scholbrock, P. Fleming, D. Schlipf, A. Wright, K. Johnson, and N. Wang. Lidar-enhanced wind turbine control: Past, present, and future. In *2016 American Control Conference (ACC)*, pages 1399–1406. IEEE, 2016.

[57] M.L. Shaltout, M.M. Alhneaish, and S.M. Metwalli. An economic model predictive control approach for wind power smoothing and tower load mitigation. *Journal of Dynamic Systems, Measurement, and Control*, 142(6):061005, 2020.

[58] M.L. Shaltout, J.F. Hall, and D. Chen. Optimal control of a wind turbine with a variable ratio gearbox for maximum energy capture and prolonged gear life. *Journal of solar energy engineering*, 136(3), 2014.

[59] M.L. Shaltout, Z. Ma, and D. Chen. An economic model predictive control approach using convex optimization for wind turbines. In *2016 American Control Conference (ACC)*, pages 3176–3181. IEEE, 2016.

[60] M.L. Shaltout, Z. Ma, and D. Chen. An adaptive economic model predictive control approach for wind turbines. *Journal of Dynamic Systems, Measurement, and Control*, 140(5), 2018.

[61] M.L. Shaltout, N. Zhao, J.F. Hall, and D. Chen. Wind turbine gearbox control for maximum energy capture and prolonged gear life. In *Dynamic Systems and Control Conference*, volume 45318, pages 33–39. American Society of Mechanical Engineers, 2012.

[62] J.G. Silva, B. Doekemeijer, R. Ferrari, and J.W. van Wingerden. Active power control of waked wind farms : compensation of turbine saturation and thrust force balance. In *2021 European Control Conference (ECC)*, pages 1223–1228. IEEE, 2021.

[63] P. Silva, A. Giuffrida, N. Fergnani, E. Macchi, M. Cantù, R. Suffredini, M. Schiavetti, and G. Gigliucci. Performance prediction of a multi-MW wind turbine adopting an advanced hydrostatic transmission. *Energy*, 64:450–461, 2014.

[64] R. Smits. Analysis of a wind driven reverse osmosis desalination system: experimental study using a pressure exchanger energy recovery device, 2019.

[65] E. Trostmann. *Water hydraulics control technology.* Routledge, 2019.

[66] M. Tsili and S. Papathanassiou. A review of grid code technical requirements for wind farms. *IET Renewable power generation*, 3(3):308–332, 2009.

[67] UNFCC. Paris agreement to the United Nations framework convention on climate change. pages 16–1104, 2015.

[68] M. Vaezi, M. Deldar, and A. Izadian. Hydraulic wind power plants: a nonlinear model of low wind speed operation. *IEEE Transactions on Control Systems Technology*, 24(5):1696–1704, 2016.

[69] M. Vaezi, A. Izadian, and M. Deldar. Adaptive control of a hydraulic wind power system using multiple models. In *Industrial Electronics Society, IECON 2014-40th Annual Conference of the IEEE*, pages 1964–1970, 2014.

[70] S. Van Didden. On the control of a seawater-hydraulic wind farm with the Delft Offshore Turbine. 2019.

[71] M.T. van Dijk, J.W. van Wingerden, T. Ashuri, and Y. Li. Wind farm multi-objective wake redirection for optimizing power production and loads. *Energy*, 121:561–569, 2017.

[72] D. van Hanswijk. Learning-based model predictive control for a wind-powered fresh water production plant with integrated electricity production. 2021.

[73] J.W. van Wingerden, P.A. Fleming, T. Göcmen, I. Eguinoa, B.M. Doekemeijer, K. Dykes, M. Lawson, E. Simley, J. King, D. Astrain, M. Iribas, C.L. Bottasso, J. Meyers, S. Raach, K. Kölle, and G. Giebel. Expert elicitation on wind farm control. In *Journal of Physics: Conference Series*, volume 1618, page 022025. IOP Publishing, 2020.

[74] L. Wang. Continuous time model predictive control design using orthonormal functions. *International Journal of Control*, 74(16):1588–1600, 2001.

[75] F.M. White. *Viscous Fluid Flow.* Mc Graw-Hill Science, 2th edition, 1991.

[76] F.M. White. *Fluid mechanics.* Mc Graw-Hill International, 6th edition, 2008.

[77] I.L. Wijnant, B. van Ulft, B. van Stratum, J. Barkmeijer, J. Onvlee, C. de Valk, S. Knoop, S. Kok, G.J. Marseille, H.K. Baltink, and A. Stepek. The Dutch Offshore Wind Atlas (DOWA): description of the dataset. *The DOWA project*, 2019.

[78] Wind Europe. World's first offshore wind farm without subsidies to be built in the Netherlands, 2018.

[79] H. Zhang. *Torque measurement on wind turbines and its application in the determination of drivetrain efficiency*. PhD thesis, Hannover: Institutionelles Repositorium der Leibniz Universität Hannover, 2021.

[80] Z. Zhang. Flow interactions in pelton turbines and the hydraulic efficiency of the turbine system. *Proceedings of the Institution of Mechanical Engineers, Part A: Journal of Power and Energy*, 221(3):343–355, 2007.

Glossary

List of Acronyms

ADM	actuator disk model
APC	active power control
CDP	continuously variable displacement pump
CEMPC	convex economic model predictive control
CMPC	convex model predictive control
DDP	digital displacement pump
DOT	Delft Offshore Turbine
DOWA	Dutch Offshore Wind Atlas
EMPC	economic model predictive control
FB-FFC	feedback with feedforward compensation
HWF	hydraulic-drivetrain wind farm
HWT	hydraulic-drivetrain wind turbine
IEC	International Electrotechnical Comission
I&I	immersion and invariance
IPC	individual pitch control
LCOE	levelized cost of energy
LIDAR	light detection and ranging
LPV	linear parameter-varying
MICEMPC	mixed-integer convex economic model predictive control
MIMO	multi-input, multi-output
MPC	model predictive control

MPPT	maximum power point tracking
NREL	National Renewable Energy Laboratory
NTM	Normal Turbulence Model
OTEC	ocean thermal energy conversion
PCD	pitch circle diameter
PI	proportional-integral
PID	proportional-integral-derivative
QP	quadratic programming
RO	reversed osmosis
SOCP	second-order cone programming
TSR	tip-speed ratio
WC	wake control